Chapter 6

The ATLAS Experiment at the Large Hadron Collider LHC

(L. Andricek, A. Barajas-Velez, A. Bangert, T. Barillari, M. Beimforde, N.Ch. Benekos, S. Bethke, B. Bittner, J. Bronner, D. Capriotti, G. Cortiana, D. Dannheim, A. D'Orazio, V. Danielyan, G. Dedes, J. Dubbert, Th. Ehrich, A. Fischer, M. Fras, C. Delle Fratte, N. Ghodbane, P. Giovannini, T. Göttfert, M. Groh, W. Haberer, J. Habring, P. Haefner, R. Härtel, A. Hambarzumjan, Th. Haubold, S. Horvat, J. Huber, A. Jantsch, St. Kaiser, M. Kilgenstein, A. Kiryunin, S. Kluth, O. Kortner, S. Kotov, H. Kroha, S. Leber, F. Legger, M. Lippert, J. v. Loeben, A. Macchiolo, S. Menke, S. Mohrdieck-Möck, P. Mooshofer, H.-G. Moser, R. Nisius, H. Oberlack, S. Pataraia, G. Pospelov, I. Potrap, E. Rauter, D. Rebuzzi, O. Reimann, R. Richter, R.H. Richter, A. Rudert, D. Salihagic, P. Schacht, J. Schieck, J. Schmaler, S. Schmidl, H. von der Schmitt, Ph. Schwegler,P. Seidler, R. Sedlmeyer, M. Stadler, S. Stern, I. Thiel, G. Tratzl, Ch. Valderanis, M. Vanadia, P. Vanoni, B. Weber, P. Weigell, H. Wetteskind, A. Wimmer, G. Winklmüller, J. Yuan, X. Zhuang, V. Zhuravlov, J. Zimmer)

The LHC experiments started to take data for high-energy proton-proton collisions in March 2010. The accelerator provides substantial luminosity at 7 TeV proton-proton centre-of-mass energy since, and event data corresponding to 0.3 pb^{-1} have been recorded by ATLAS so far. The luminosity of LHC will continue to improve rapidly in the 2nd half of the 2010 running period, with the aim to collect 1 fb^{-1} by the end of 2011, when a shutdown is planned to go towards the design c.m.s. energy of 14 TeV.

Since the last report to the Fachbeirat [1], the ATLAS group at MPI has made extensive use of cosmics and single-beam data to have detector, software and computing facilities well-commissioned before collisions data arrived. Thanks to these efforts, performance in tracking and calorimetry was close to the design values very early on. For instance, the mass peaks of known particles accessible with initial luminosity are as expected. See section 6.1 for the final phases of detector installation, and for commissioning.

Physics analyses with the luminosity collected by Mid 2010 have resulted in a first set of ATLAS physics papers. Analyses of processes which require higher luminosity, as expected before end of 2010 and beyond, are well prepared. Fig. 6.1 gives an overview of signal and background cross sections at LHC. See section 6.2 for those parts of physics analyses in which MPI is firmly involved.

The LHC future planning foresees a substantial increase of luminosity beyond the design of the present machine, to further extend its physics reach. MPI participates in detector and electronics development with the aim of exploiting higher event rates with ATLAS. See section 6.3 for the detector upgrade activities at MPI.

The detector is described in detail in the ATLAS Detector paper [2]. In the remainder of this introduction we briefly recall the ATLAS components with MPI involvement.

The Inner Detector

Tracking detectors at the LHC have to face three major challenges: high occupancy, severe radiation damage and a short bunch crossing interval. A typical hard interaction like $t\bar{t}$ production creates several hundred charged particles within a rapidity range of $|\eta| \leqslant 2.5$. In ten years of operation a flux of up to $5 \cdot 10^{14}$ n_{eq}/cm^2 (1 MeV neutron equivalent) particles cause substantial radiation damage to the SemiConductor Tracker (SCT). Furthermore the short bunch crossing interval of 25 ns demands fast sensors with fast readout elec-

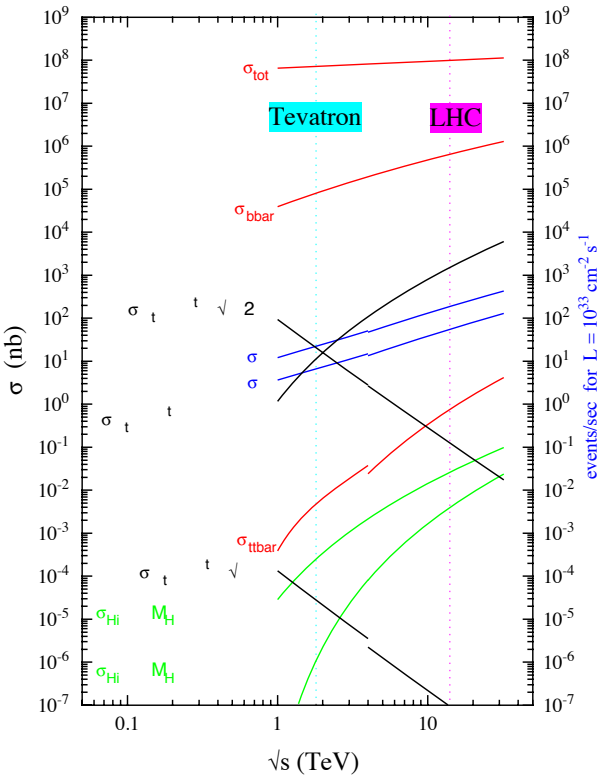

Figure 6.1: Particle production cross-sections in proton–proton collisions as a function of the center-of-mass energy $\sqrt{s}$ and the corresponding number of events produced per second at a luminosity of $\mathcal{L} = 10^{34}\,\mathrm{cm}^{-2}\mathrm{s}^{-1}$ planned for the LHC. The red dotted line marks the collision energy of the LHC. The increase of cross-section is several orders of magnitude compared to the Tevatron at Fermilab.

tronics. Driven by the required physics performance, a survival capability of at least ten years of operation, and costs, a layout for the silicon part of the ATLAS Inner Detector (ID) was identified in the Technical Design Report [3]. A sketch of the ID is shown in Fig. 6.2.

The complete ID is operated in a 2 T axial field. Detailed descriptions and specifications of the ID, its components and the expected performance can be found in [4, 5]. It is designed to provide a resolution in transverse momentum, in the plane perpendicular to the beam axis, of $\sigma_{p_\mathrm{T}}/p_\mathrm{T} = 0.0005 p_\mathrm{T}/\mathrm{GeV} \oplus 0.01$ and a transverse impact parameter resolution of 10 μm for high momentum particles in the central detector region [4].

Occupancy and radiation damage depend strongly on the radius, r. To allow for an optimized technical solution for each radial region, the ID is segmented into three parts, each using a different detector technology:

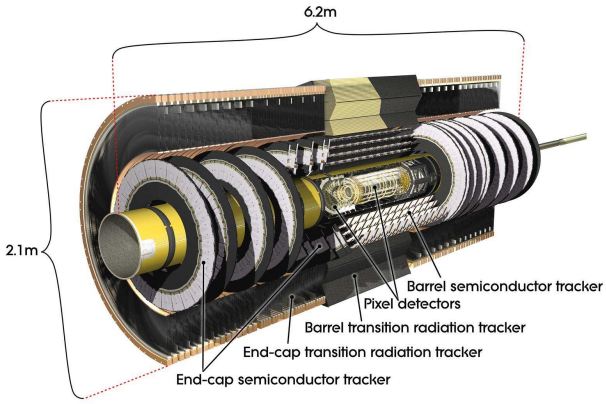

Figure 6.2: Sketch of the ATLAS Inner Detector.

- In the innermost region, $5\,\mathrm{cm} \leqslant r \leqslant 12\,\mathrm{cm}$ a high granularity silicon pixel detector with about 80 M readout channels is used. It offers an excellent space point resolution and low occupancy. The high resolution of this detector is essential for secondary vertex reconstruction, needed e.g. for τ-lepton and b-quark identification.

- In the intermediate region, $30\,\mathrm{cm} \leqslant r \leqslant 51\,\mathrm{cm}$, a silicon micro-strip detector, the SCT, is used. The strips are oriented to measure with high precision the track coordinates transverse to the beam. A small stereo angle between two faces of a detector module allows measuring the orthogonal coordinate, albeit with less precision. The detector measures up to four space points per track. For the SCT the total area of silicon is about 61 m^2.

- Finally, for $56\,\mathrm{cm} \leqslant r \leqslant 107\,\mathrm{cm}$, the transition radiation tracker (TRT) uses straw tubes. The large number of straws allows continuous tracking with on average 36 hits per track, which, despite the moderate space resolution of single hits, results in a high precision measurement at large radii. In addition, the ability to detect transition radiation improves the electron/pion separation. The challenge for this detector is to cope with the high occupancy.

The actual performance of the ID after the final installation including the cosmic ray data analysis from the year 2008 is discussed in [6]. At the LHC, the ID already served to measure the multiplicities and spectra of charged particles in minimum bias interactions at a proton-proton center of mass energy of 900 GeV [7], presenting the first ATLAS LHC physics result.

The Hadronic End-cap Calorimeter

The ATLAS MPI calorimeter group has contributed to the construction, assembly, installation and commissioning of the hadronic end-cap calorimeter (HEC) system [27, 45], to the cold electronics of the HEC employing the novel concept of 'active pads' [140], to the read-out system of the calorimeter, and to the trigger summation for the HEC. The group has also taken over the responsibility for the hadronic calibration of the ATLAS calorimeter [37] and is strongly involved in the preparation of $t\bar{t}$ [41] and jet analyses [38, 39]. The large $t\bar{t}$ cross section provides even in the LHC start-up phase a reasonable statistic of $t\bar{t}$ events. In the very first stage they will yield a powerful in-situ test of the hadronic calibration in ATLAS.

The Muon Spectrometer

The muon spectrometer [48, 49] of the ATLAS experiment is equipped with three layers of muon detectors in a toroidal magnetic field of $3-6$ Tm bending power generated by a superconducting air-core magnet system. The spectrometer is designed to provide muon momentum resolution of better than 10% for transverse momenta up to 1 TeV/c over a pseudo-rapidity range of $|\eta| \leqslant 2.7$. This requires a very accurate track sagitta measurement with three layers of muon detectors which have to be aligned relative to each other with an accuracy of up to $30\,\mu$m in the bending direction in the magnetic field. Drift chambers with very high spatial resolution of $40\,\mu$m, the Monitored Drift Tube (MDT) chambers, have been developed to cover the active area of the spectrometer of $5500\,\mathrm{m}^2$ with only 5% gaps mainly in the region of the detector feet.

The cylindrical central part of the spectrometer (barrel) contains eight race-track shaped magnet coils of 25 m length and 5 m radial width. The layout of the muon chambers follows the eightfold symmetry of the magnet around the proton beam axis in eight small and eight large azimuthal sectors (see Figure 6.3). The barrel part of the spectrometer is complemented by two endcaps each consisting of eight superconducting coils housed in a common cryostat fitting into the inner bore of the barrel toroid magnet and three wheel-shaped layers of muon detectors.

The MDT chambers built in Munich consist of two triple layers of 30 mm diameter aluminium drift tubes of 3.8 m length equipped with a central gold-plated tungsten-rhenium sense wire which are separated by an aluminium space frame. The drift tubes are operated with Ar:CO_2 (93:7) gas mixture at a pressure of 3 bar and a gas amplification of 20,000 (corresponding to a operating voltage between tube wall and wire of 3080 V) and provide a position resolution of about $80\,\mu$m . The sense wires are positioned within a chamber with an accuracy of better than $20\,\mu$m in order to achieve the required spatial resolution of the chambers [50].

In the years 2001 to 2006, 88 MDT chambers were constructed at the MPP [51] containing about 36000 drift tubes. They cover about 15% of the active area of the spectrometer.

ATLAS Computing

The contruction and operation of the computing system for the ATLAS experiment is a major undertaking carried out by the ATLAS collaboration with support from the Worldwide LHC Computing Grid (WLCG) collaboration. The MPP contributes its share to this task with a large Linux cluster located at the Rechenzentrum Garching (RZG) of the MPG. This cluster serves as a part of the Munich ATLAS Tier-2 centre, hosts the Munich calibration and alignment centre for the ATLAS Muon system (MCAC) and provides our institute's users with large computing and storage ressources. In addition the MPP ATLAS group has several members working on central computing tasks for ATLAS.

6.1 Detector Commissioning and Computing

6.1.1 The Semiconductor Tracker SCT

Because of the MPP experience with silicon microstrip sensors and the unique possibilities offered by the associated semiconductor laboratory (HLL = HalbLeiterLabor), MPP decided to participate in the design and construction of the SCT.

Mechanically the SCT consists of three main units, namely the barrel and two identical endcaps. The barrel covers the region of central rapidity, $|\eta| \leqslant 1$, and the detector modules, i.e. the smallest mechanically sensitive units of the SCT, are arranged on four cylinders around the beam axis. The endcaps extend the acceptance up to $|\eta| \leqslant 2.5$. Here the modules are mounted on nine disks per endcap, and are oriented perpendicular to the beam axis.

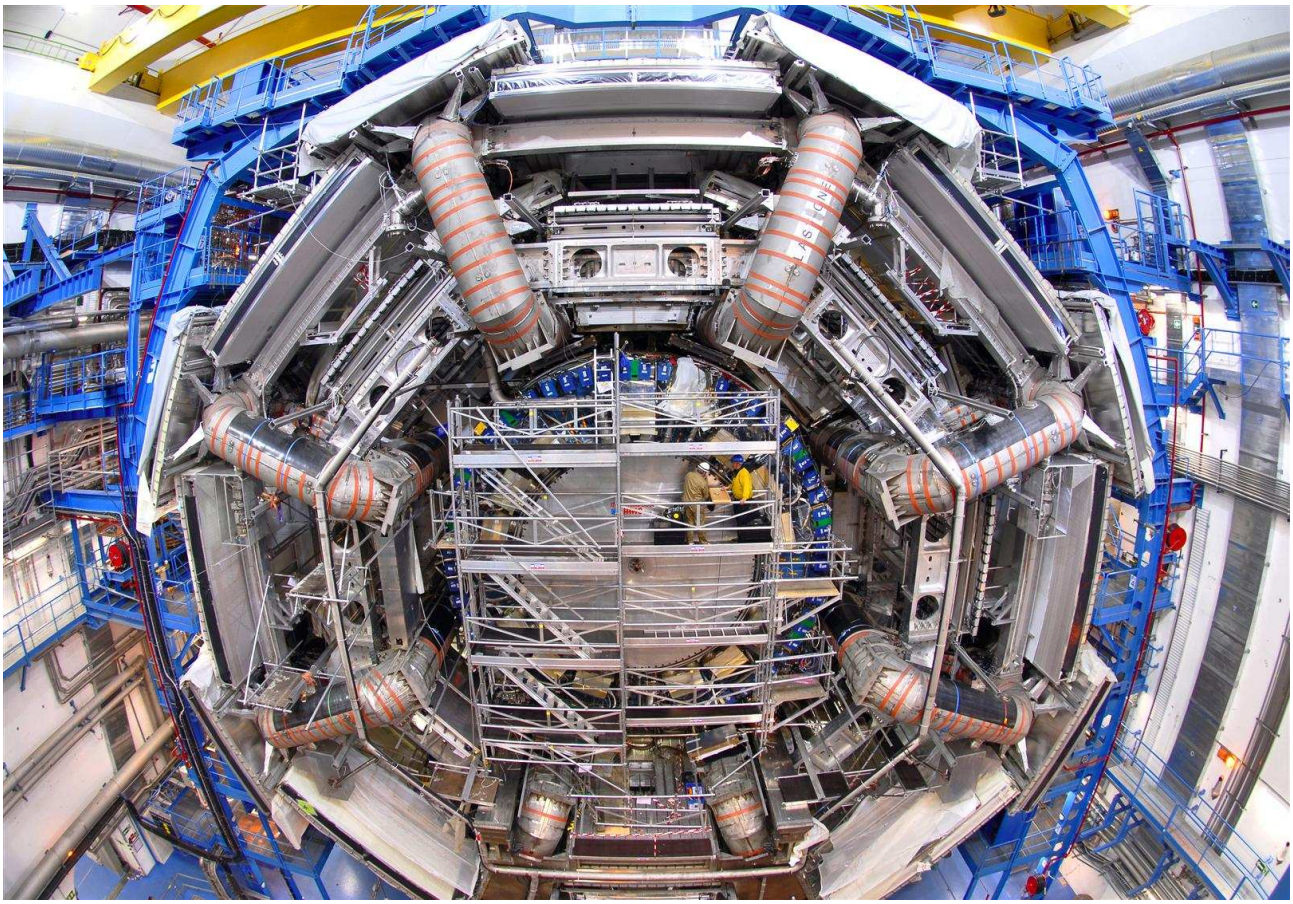

Figure 6.3: The barrel part of the ATLAS muon spectrometer viewed from the LHC tunnel after completion of the muon chamber installation in November 2006. The MDT chambers built in Munich are mounted on rails on the outside of the eight superconducting magnet coils.

The barrel modules are made from four rectangular sensors glued back to back in pairs. The sensor dimensions are about 6.4 cm $\times$ 6.4 cm and the strip pitch of the 768 strips per sensor is 80 μm. Electrically, the two sensors of either pair are chained in series. One pair has the strip orientation parallel to the beam, while the second pair is rotated by 40 mrad in order to yield stereo information. The binary readout electronics is located on a bridge on the top and backside. In the binary mode the only information retained per channel is whether the observed signal was above or below a discriminating threshold. To equalize the efficiency of all channels for detecting a passing particle, the discriminating threshold can be set individually for each channel by means of calibration capacitors.

Due to the radial arrangement the endcap modules use wedge shaped sensors, with the strip pitch varying in the range (64–90) μm. Again the strips of two sensors are connected. One pair has the strips oriented radially, the second pair is rotated by 40 mrad. A double sided hybrid with the electronics is attached to the end of the module. On a fully populated disk, three different types of endcap modules, inner, middle and outer modules, are arranged in three rings.

A major challenge for the ATLAS SCT is the large radiation level which leads to severe radiation damage of the sensors and the readout electronics. The system requires a very high geometrical stability, due to the cold operation and the dissipation of the heat generated by the electronics and the sensor leakage currents.

MPP Engagements in the ID

In the years 1997–2006 the MPP engagement mainly concentrated on 1) the development of a cost-effective design for radiation-tolerant silicon strip sensors, 2) the design work for the endcap modules concentrating on the mechanical and thermal performance, 3) the construction of 424 SCT endcap modules of the middle type, Fig. 6.4, which amount to about 30% of all endcap modules, 4) the integration, as well as performance measurements with cosmic ray muons, of the

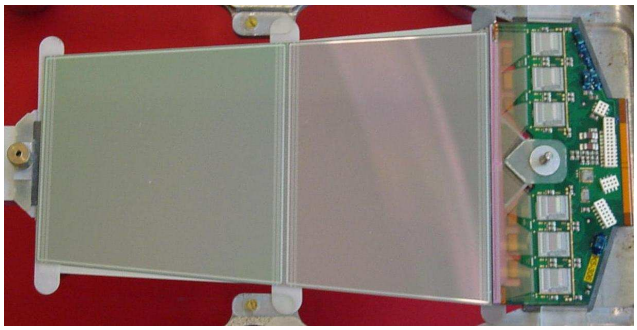

Figure 6.4: View of a middle module constructed by MPP technicians.

combined SCT and TRT detectors at the surface before their installation into the ATLAS cavern, and 5) the alignment of the silicon part of the ID with particle tracks. Detailed reports of the work performed

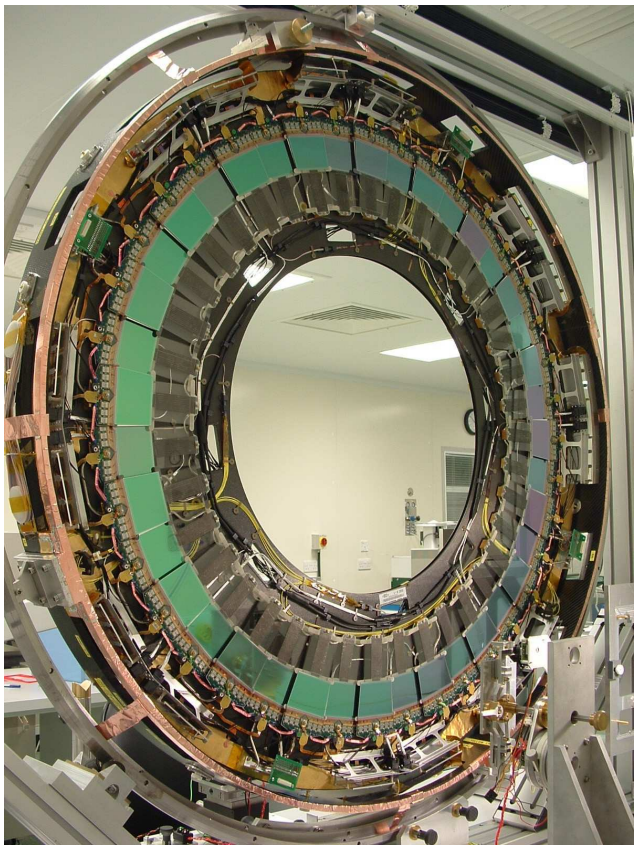

Figure 6.5: First disc equipped with MPP short middle modules.

by the MPP group in the years 1997–2006 can be found in [8, 9]. The properties of the sensors are described in [10], details of the endcap modules and their production process are given in [11]. The first 40 short middle modules [1], produced by MPP, and mounted onto one endcap disc at Liverpool, are shown in Fig. 6.5.

In the years 2007–2010 for the present ATLAS detector the MPP group mainly worked on the SCT commissioning with emphasis on detector monitoring, and the alignment of the silicon part of the ID with particle tracks.

SCT Commissioning

The MPP is contributing to the SCT detector commissioning in the area of online monitoring.

The SCT read-out-system (ROS) is structured in various layers. The ROS monitoring is used to continuously control the detector operation, and thereby also gives valuable information on the LHC beam condition that ATLAS is facing. It comprises error searches at chip-, link-, or read-out-driver level, but also information on the actual illumination of the SCT by means of strip occupancies. The ROS monitoring is mostly independent of the ATLAS trigger system, and can give even faster feedback on much more data, than what is eventually written to tape. The MPP group provides a ROS monitoring expert, whose task is to constantly maintain and extend the ROS monitoring software and its interface to the online monitoring of the ATLAS SCT as a whole. The fast feedback achieved is a valuable input to the detector operation, and has already led to a detailed understanding of some LHC conditions that otherwise would have been difficult to get.

Detector Alignment with Particle Tracks

Since 2004 the MPP group develops software for the alignment of the SCT and pixel detector parts of the ATLAS ID based on particle tracks. To achieve the best possible reconstruction of tracks the exact location of all read-out channels needs to be known. In a first step this is achieved by a geometrical survey of the detector, however, for the ultimate precision the use of particle tracks is mandatory.

A crude estimate of the alignment precision aimed at can be obtained from the requirement that the detector misalignment should lead to a degradation of any

[1] The only difference between middle- and short middle modules is that the latter only carry one sensor per module side, i.e. the second sensor is replaced by a glass plate that is insensitive to passing particles, but retains the mechanical stability of the module. Short middle modules are used at the largest rapidities.

track parameter of at most 20% [3](p. 215). Using this requirement, the misalignment for SCT modules in the direction perpendicular to the strip orientation should not exceed 12 μm. Final physics aims of ATLAS are even more demanding. For improving on the determination of the mass of the W-Boson, i.e. for an accuracy of better than 25 MeV, an alignment accuracy of about 1 μm transverse to the beam direction is needed [12].

As an example, for the SCT optical surveys are performed for the location of the silicon sensors within the modules (see above), and for the mounting points of the modules on the discs (see the fixations at both short ends of the modules visible in Fig. 6.5) and barrel cylinders. The accuracy obtained with the external methods is better than 5 μm for the positions of the sensors within a module. For the module locations one expects larger uncertainties. For the SCT endcap modules the expected precision is about 50 (100) μm transverse (parallel) to the beam direction, which is not precise enough to achieve the physics goals of ATLAS.

From the above it is clear that in any case the ultimate precision has to be obtained using the trajectories of charged particles observed in real data. Using the external measurements as starting points, the knowledge of the module locations is improved by the alignment procedure based on particle tracks. The MPP strategy uses an iterative procedure to constrain the six degrees of freedom for individual modules by means of a χ^2 minimization of the sum of unbiased track residuals (see below) with respect to the alignment parameters per module. This method is called the local χ^2 algorithm. Figure 6.6 shows the local coordinate system of an SCT module. The six degrees of freedom are the three coordinates along three axes running perpendicular to the strip, along the strip and perpendicular to the module plane (x, y, z), and the three angles of rotation around these axes, namely α, β and γ. For a given single strip that gave a signal above threshold and is associated to a fitted track, the unbiased residual is defined as the smallest distance in space between the actual location of the strip and the fitted trajectory obtained when excluding that hit from the track fit. By means of iterations, this method incorporates the correlation of the locations of the modules traversed by a particle.

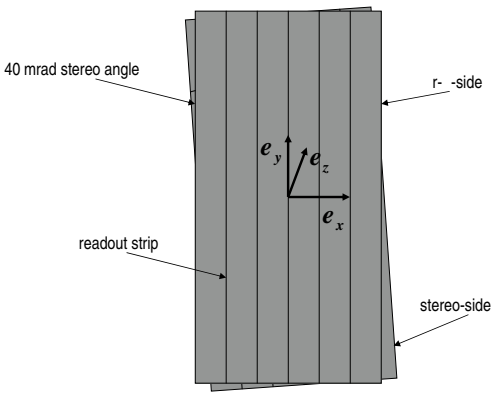

Figure 6.6: Local coordinate system of an SCT module.

The algorithm has initially been implemented into the ATLAS reconstruction software for the SCT detector [13]. It was extended to also incorporate the pixel detector [14] by treating the two precise pixel measurements along the two dimensions of the pixel as two independent measurements in analogy to the two hits recorded on the two sensors of an SCT module. Thereby the basic mathematical framework could be kept the same, facilitating the simultaneous alignment of pixel and SCT detectors.

In the conventional alignment procedures the detector geometry is only updated after a large number of particle tracks has been analyzed, and the χ^2 has been minimized with respect to the alignment parameters. As an alternative a KALMAN filter approach has been implemented and studied [15]. Here the knowledge gained by analyzing the tracks from one event is immediately fed back resulting in a geometry update after each event. The basic functionality of the KALMAN approach has been achieved. However, no striking advantage in convergence speed has been observed. In addition, in contrast to e.g. the local χ^2 algorithm, the KALMAN filter algorithm cannot be parallelized. Therefore, this possible advantage could always be compensated by parallel computing, and consequently this approach is no longer followed in ATLAS.

The local χ^2 algorithm has been used in very different environments like Monte Carlo simulated proton-proton interaction events [16], data from an ID combined test beam (CTB) run [17, 18], simulated interactions of protons with the rest gas in the beam pipe, data recorded from cosmic ray muons taken at the surface [19] as well as after completion of the ATLAS detector at its final position [17, 20], and finally with proton-proton collision data from the LHC.

In these studies it became evident that for each of the data sets, due to their specific limitations, additional features had to be implemented into the algorithm to either make it properly converge, or to improve on its performance. The separation of the alignment into three subsequent levels, L1 to L3, (L1 $\equiv$

global structures, i.e. barrel and endcaps, L2 ≡ superstructures, i.e. barrel layers and endcap discs, L3 ≡ individual modules) has been performed and an enrichment of overlap hits (pairs of neighboring modules on superstructures slightly overlap, see Fig. 6.5) was implemented into the algorithm for better convergence [17].

For the CTB setup the improvement of the momentum resolution is seen in Fig. 6.7 [18], where the 1/momentum resolution before and after performing the alignment is shown for pions with 100 GeV momentum. The initially wide distribution is greatly improved, and after the alignment the narrow distribution peaks at the correct value. In Fig. 6.8 [18] the performance of the MPP algorithm is compared to other algorithms used in ATLAS, and also to the expectation of the ATLAS Monte Carlo simulation based on the perfect knowledge of the geometry. Here, the figure of merit is the momentum resolution as a function of the known momentum. The algorithms perform similar, with the exception of the robust algorithm that, due to its simplistic but robust implementation, is slightly worse. The other algorithms also closely match the expected resolution.

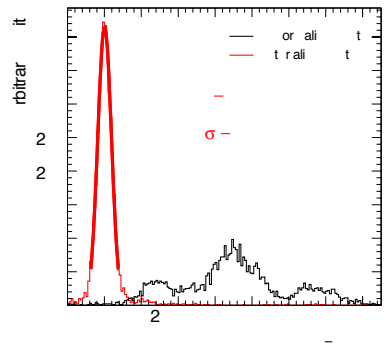

Figure 6.7: Improvement of the momentum resolution by the CTB alignment

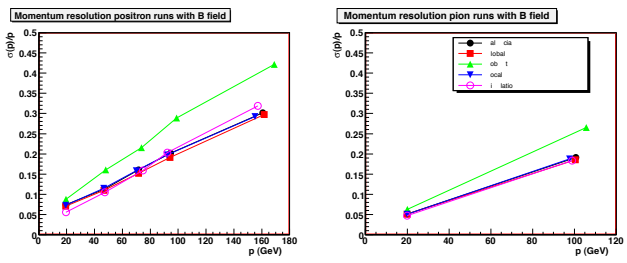

Figure 6.8: Momentum resolution for different momenta, and for positrons (left) and pions (right), for the CTB setup when using different alignment algorithms.

For the cosmic ray muon analysis the limited illumination of the detector in the ATLAS cavern poses a challenge. Due to the geometry, cosmic rays pass barrel modules mostly perpendicular to the sensors, but endcap modules almost parallel. This renders some degrees of freedom only loosely constrained, most notably for the SCT endcaps. To accommodate this, further improved mixed levels of alignment were constructed, i.e. the level L32 (barrel L3 SCT alignment, but endcaps only L2 SCT alignment) has been implemented, supplemented by additional soft constraints to limit the parameter movements of badly constrained degrees of freedom by means of pseudo hits with appropriate uncertainties [20].

For the cosmic ray alignment Fig. 6.9 shows the flow of the six alignment parameters of the pixel layers (blue) and discs (green, red) with consecutive iterations, using five iterations at L1 followed by thirty iterations at L2. A perfect convergence would man-

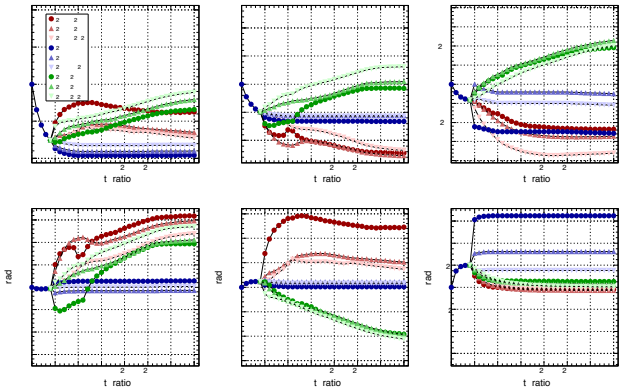

Figure 6.9: Flow of alignment parameters of the pixel layers and discs during alignment iterations for cosmic ray data.

ifest itself in horizontal lines, which is clearly better fulfilled for the barrel layers than for the discs that, due to the inclination angle of the cosmic ray muons, are less well constrained. Nevertheless, as displayed in Fig. 6.10, the residual distributions for pixel and SCT modules in barrel and endcaps are greatly improved after L2 (blue) and the final (red) alignment. Again, when comparing to the expectation for perfect knowledge of the geometry (yellow), all distributions move the right way, with the SCT barrel modules (lower left) getting the closest. The alignment based on cosmic ray data will constitute the basis for the alignment to follow with tracks coming from the interaction vertex in proton-proton collisions at the LHC.

The influence on the alignment caused by constrain-

ing the tracks to a common vertex, as well as the impact of systematic detector mis-alignments on the performance of the ATLAS b-tagging algorithms, have also been studied [16].

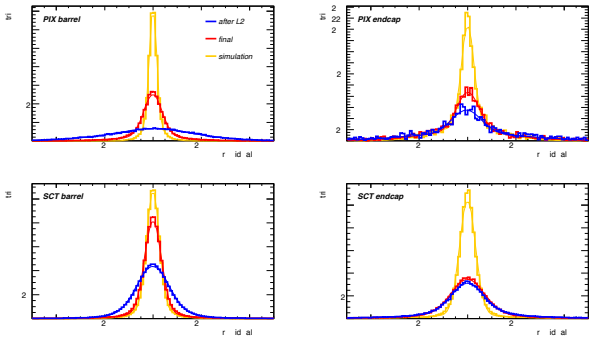

Figure 6.10: Improvements in the residual distributions for the alignment using cosmic ray data.

Finally, the recovery of so called weak deformation modes of the detector, i.e. systematic deformations that either leave track parameters virtually unchanged, or lead to changed, but consistent parameters, was thoroughly studied. The deformations were implemented into the simulation [20], and their impact on the track parameters, as well as on the measured invariant mass of the Z-Boson reconstructed from $Z \rightarrow \mu\mu$ events, was investigated [21].

The progress of the ATLAS ID alignment has been constantly reported outside of ATLAS [22, 23, 24] by members of the MPP group. At present the alignment based on proton-proton collision data from the LHC is underway. It turned out that the SCT endcap alignment obtained from the cosmic ray analysis is easily improved by inclusion of this data. However, the SCT barrel alignment is already so precise that significant improvements need further adaptations of the software like inclusion of constraints provided by invariant masses from known resonances.

6.1.2 The Hadronic End-cap Calorimeter HEC

There are two end-caps in the ATLAS calorimeter system. The HEC, which covers the rapidity range $1.5 < |\eta| < 3.2$, consists of two independent mechanical units ('wheels') per end-cap: the front and the rear wheel. Each wheel has a diameter of ≈ 4 m. The absorber structure of the two wheels consists of parallel copper plates of 25 mm (50 mm) for the front (rear) wheels. There is a gap of 8.5 mm of LAr between adjacent absorber plates. Three electrodes divide this gap into four separate LAr drift zones of 1.8 mm width each. Each calorimeter wheel is divided into 32 individual modules. A front (rear) module collects the signal in 24 (16) LAr gaps. The signals of two adjacent gaps are collected and transmitted to an amplifier channel in the 'active pad' (cold) electronics. Finally the signals corresponding to a tower pointing to the interaction point are summed. There are four such longitudinal segmentations for each end-cap tower. The signal processing of the HEC employs the notion of 'active pads' which keeps the detector capacities at the input of the amplifiers small and thereby achieves a fast rise time of the signal [140]. Short coaxial cables are used to send the signals from the pads to preamplifier and summing boards (PSB) located at the perimeter of the wheels inside the liquid argon. These PSB's carry highly integrated amplifier and summing chips in Gallium-Arsenide (GaAs) technology.

Commissioning of the HEC

Cosmic Muons. First tests reconstructing the real particle response in ATLAS have been done using muons from cosmic rays in the years 2007 and 2008 [45, 47]. For the HEC the incoming cosmic ray flux is mostly parallel to the orientation of the absorber plates and the LAr gaps. Nevertheless, using inclined tracks and reconstructing the effective track length in individual read-out cells, a cross check of the calibration can be done. Alternatively the energy in the calorimeter cells alone can be used to select data samples independent of the muon tracks. This approach has been adopted for the pulses in figure 6.11. Only small deviations ($3 - 5\%$) of the prediction from the data in the peak region and the end of the negative undershoot are observed.

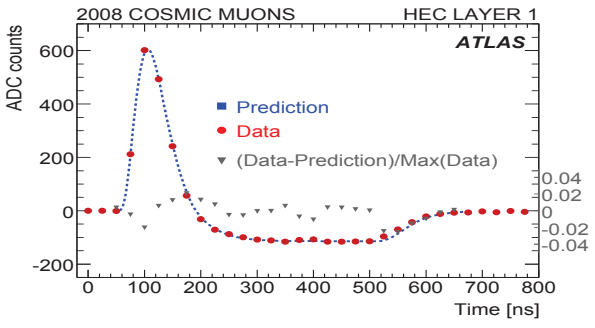

Figure 6.11: Typical pulse shapes, recorded during the cosmic ray campaign, for the first layer of the HEC. The relative difference between data and prediction is indicated by triangles on the right scale.

Random triggers in the cosmic data are taken to measure the electronics noise, and the stability of pedestal with time. Figure 6.12 shows the measured noise on cell level for each layer of the LAr calorimeter as a function of $|\eta|$. Good agreement with predicted values from simulations [44] is observed and the uniformity in ϕ and the symmetry in η is within a few percent. The stability of the pedestals in the HEC was monitored over 6 months and showed variations of 2 MeV only – well below the numerical precision of the energy computation which is 8 MeV.

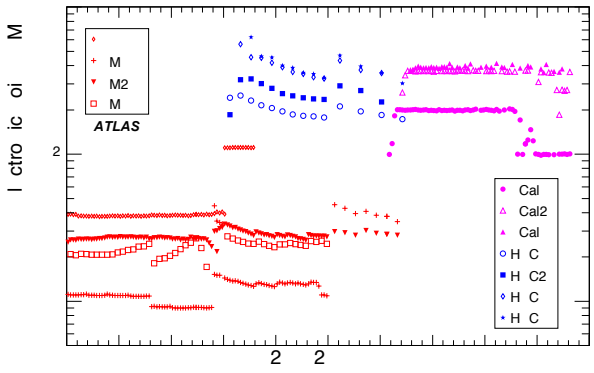

Figure 6.12: Electronic noise (σ_{noise}) in randomly triggered events at the EM scale in individual cells for each layer of the LAr calorimeter as a function of $|\eta|$. Results are averaged over ϕ.

The transverse missing energy in random triggers is sensitive to correlated noise in the calorimeter and has been used together with noise suppression methods to search for unaccounted effects in the noise description. Figure 6.13 shows $E_{\mathrm{T}}^{\mathrm{miss}}$ computed for all cells above 2σ noise and for cells inside topological clusters [36] (see also section 6.1.2) which are seeded by cells above 4σ. Both are consistent with the Gaussian model of electronics noise although the agreement in the stricter suppressing case using topological clusters is a bit worse due to the enhanced sensitivity to details in the noise description. The absence of large tails shows that the electronics noise is well under control and not perturbed by large correlated effects.

Beam Splash Events. The turn on of the LHC in 2008 and again in 2009 provided with so-called beam-splash-events another set of commissioning data. In beam splash events circulating single beams at 450 GeV are dumped on collimators some 140 m upstream of the detector and cause a large particle spray

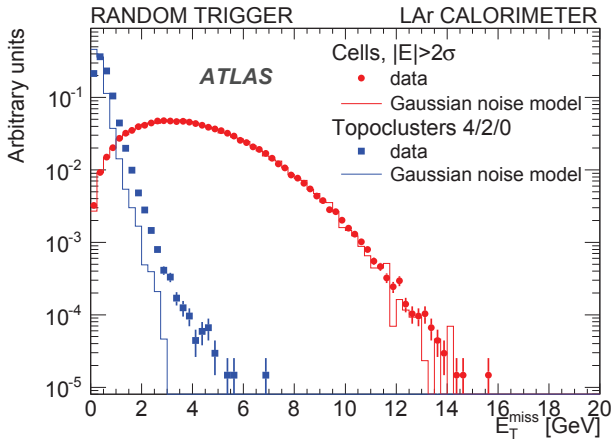

Figure 6.13: $E_{\mathrm{T}}^{\mathrm{miss}}$ distribution with LAr calorimeter cells for 135,000 randomly triggered events in June 2009. The dots (squares) show the cell-based (cluster-based) methods in the data, and the histograms show the equivalent distributions for the Gaussian noise model.

to pass the detector from one end-cap to the other leaving huge amounts of energy (typical are 1000 TeV and more) in the calorimeters. The comparison for each endcap of the average cell energy as function of η and ϕ for the 85 beam splash events observed in 2008 allowed to identify all channels with reduced high voltage, where the decrease in signal is larger than 20% [47]. Figure 6.14 shows the average cell energies on both sides for a given bin in $|\eta|$ as a function of ϕ. The missing quadrant on the C-side (missing dots at high ϕ indices) was caused by a malfunctioning power supply which is meanwhile operational again. Currently

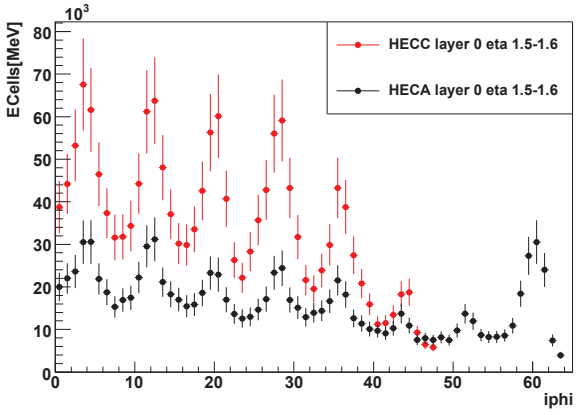

Figure 6.14: The average cell energy vs. the phi index on side A (C) the HEC in black (red) for 85 beam splash events from 2008. The periodic structure is due to the material in the endcap toroid magnets.

about 1% of all channels in the LAr calorimeters are not operational and a few percent require a correction for reduced high voltage.

The relative timing for the readout of the calorimeter systems was also tuned with the splash events. Since at these large energies the time resolution is well below 1 ns the expected time differences due to time-of-flight and the trigger could be confirmed within ± 2 ns [45].

Collisions. Finally late in 2009 the first collisions at center-of-mass energies of $\sqrt{s} = 900$ GeV have been recorded with the ATLAS detector. Comparisons to simulations of QCD processes (minimum bias events) allowed a first validation of the clustering and calibration scheme described in more detail in section 6.1.2.

Examples for these early validations with physics events are show in figures 6.15 and 6.16.

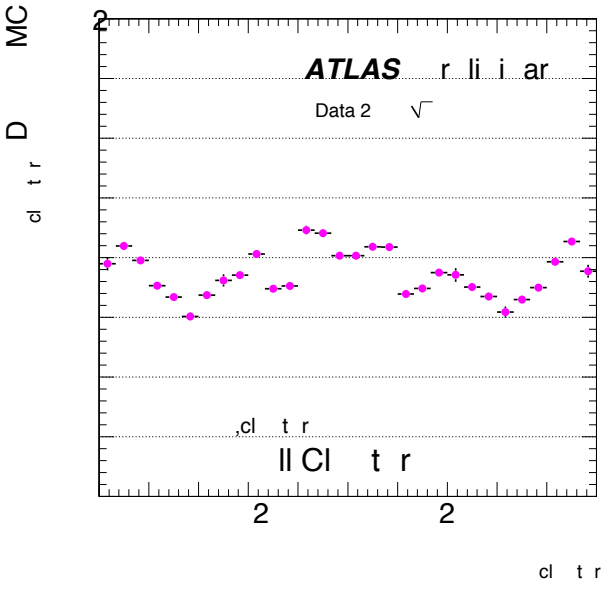

Figure 6.15: Ratio of average uncalibrated cluster energies to expectations from simulations for collisions at $\sqrt{s} = 900$ GeV.

Both figures demonstrate that the systematic error for the clustering and the calibration are well under control and currently are on the level of $< 5\%$.

Local Hadron Calibration

The local hadronic calibration [37], which is developed in large parts in our group has been further refined in the reporting period and validation efforts

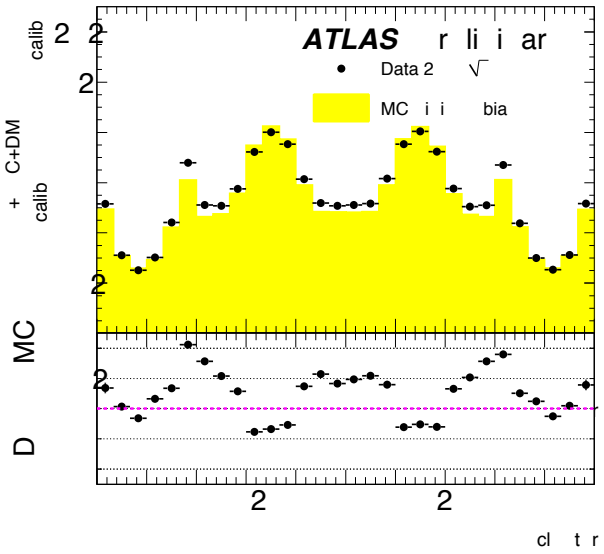

Figure 6.16: Average calibrated cluster energies normalized to uncalibrated energies (upper plot) and the ratio data to simulation (lower plot) for collisions at $\sqrt{s} = 900$ GeV. The simulation is shown in yellow in the upper plot.

started with collisions data (see section 6.1.2) and with simulated $t\bar{t}$-events [41, 47].

The aim of the method is to provide the energy on the hadron level for each individual cluster in the calorimeter which in turn serve as input to the reconstruction of higher level objects like jets [38, 39] and missing transverse energy [40]. The most important steps in this procedure are:

1. **Topological Clustering.** Clusters [36] are reconstructed in the calorimeters around seed cells with very significant energy ($|E| > 4\sigma_{\text{noise}}$). Neighboring cells in the same and in neighboring layers are added to the cluster regardless of their energy ($|E| > 0\sigma_{\text{noise}}$) and expand the cluster further by their respective neighbors in case they have significant energies ($|E| > 2\sigma_{\text{noise}}$). Clusters are merged in this step if they share a cell with significant energy. The so-found clusters are split and regrouped again around local energy maxima ($E > 500$ MeV). In this step merging of clusters is not allowed and border cells are shared among the clusters. The resulting clusters have a close correspondence to individual particles hitting the detector and thus motivate the local hadron calibration approach.

2. **Classification.** Each cluster is compared by means of cluster shape variables like depth and energy density with a-priori probabilities for such shapes derived from simulations of charged and neutral pions. If the resulting probability of the cluster to stem from a charged pion is above 50% the cluster is classified as hadronic, those with values below as electromagnetic. The probability p_{had} to be hadronic is stored as well for each cluster.

3. **Cell Weighting.** Invisible hadronic energy deposits are recovered in this step by applying cell weights w_{cell} derived from charged pion simulations to the cells in all clusters. The weights are functions of cell position, cell energy density and cluster energy as inspired by the H1 weighting scheme [34, 35]. Since electromagnetic showers do not lead to invisible energies (i.e. their weight ought to be 1) the final weight per cell is given by $p_{\text{had}} \times w_{\text{cell}} + (1 - p_{\text{had}}) \times 1$.

4. **Out-Of-Cluster Corrections.** Both, electromagnetic and hadronic showers lose energies on the edge of the shower due to the applied noise cuts. Averaged corrections depending on η, shower depth and energy are derived for both and applied with the same probabilities as in the weighting step.

5. **Dead-Material Corrections.** Energy deposits in non-instrumented material upstream of, in between, and beyond the calorimeter is recovered in this step. The correlation of the losses with energy deposits in calorimeter layers close to the dead-material (like the pre-sampler for any material upstream) is used here and parameterized corrections are applied again with the probability weighted sum of hadronic and electromagnetic corrections.

6. **Jet-Level Corrections.** Finally some corrections need to be applied to the jets made out of the calibrated clusters mainly due to particles not leaving any signal in the calorimeter and thus not accounted for in the correction steps above. The main reasons for missing signals are the noise threshold for seeding clusters, the magnetic field bending charged particles with low p_{T} outside the jet acceptance and absorbed particles in the dead material upstream of the calorimeters.

Figure 6.17 shows the comparison of the average cluster energies normalized to the uncalibrated energy as a function of η after the individual cluster calibration steps outlined above in the first collisions data. For this inclusive plot low energetic clusters dominate and the largest corrections are applied in the out-of-cluster and dead-material correction steps. As already shown in figure 6.16 the agreement with simulations is better than 4% for all η regions.

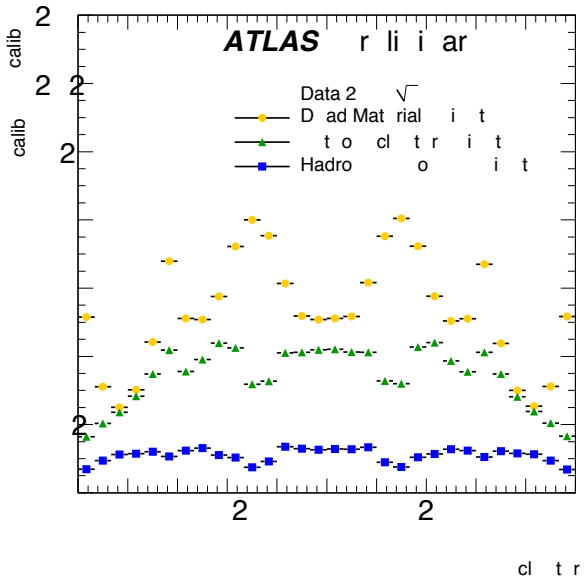

Figure 6.17: Average cluster energies normalized to the uncalibrated energy after various calibration steps for collisions at $\sqrt{s} = 900\,\text{GeV}$.

Current developments focus on the jet-level corrections, where the energy distribution of the constituent clusters in a jet is used to estimate the lost energy fraction, and the validation of the local hadron calibration with isolated hadrons in collision data at $\sqrt{s} = 7\,\text{TeV}$ and inclusive cluster samples like shown in section 6.1.2.

Another focus concerns the work on refined simulations for jets in ATLAS with the ability to tag each energy deposit with the originating hadron produced by the generator. This technique allows to use the jet simulations directly instead of single particle simulations to derive the local hadron calibration constants. First simulations with this new labeling scheme are already available and refined calibration constants are expected within the next few months.

Combined Beam Test

In 2004 the last of a series of beam tests [28, 30, 31, 29, 32] with participation of the HEC in which about 25% of the modules have been exposed to beams of electrons, pions and muons with energies up to 200 GeV, was conducted at CERN, covering the transition region $2.5 < |\eta| < 4.0$ [33]. This is a particularly complex region of overlap of the three end-cap calorimeters. The EMEC, HEC and FCal (forward calorimeter) modules are positioned as in ATLAS, including all details of cryostat walls and supports (dead material). One quarter of the front and rear HEC wheels have been assembled, but with small modules which cover in size only the forward η region. Similarly, one EMEC inner wheel module (1/8 of the EMEC wheel) and 1/4 of the FCal1 and FCal2 have been assembled. Fig. 6.18 shows a schematic of the set-up of the different calorimeter modules. The beam enters through the cryostat window from the right at a nominal position of $y = 0$ cm. Shown are the inner EMEC (front), the HEC front wheel and rear wheel modules as well as the FCal1 and FCal2 modules (below the HEC modules). In addition a cold tail catcher (CTC) is placed right behind the last FCal module in order to measure any leakage beyond the FCal2 module. In a similar way the energy leakage for the rear wheel HEC modules is measured in a warm tail catcher (WTC) placed outside the cryostat.

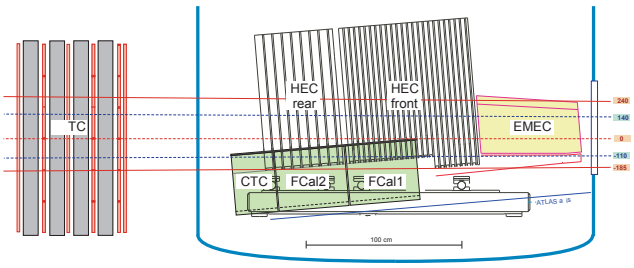

Figure 6.18: Schematic view of the calorimeter set-up of the 2004 combined beam test. Shown are the inner EMEC (front), the HEC, the FCal1 and FCal2 modules (below the HEC modules). In addition, the cold tail catcher (CTC, behind FCAL2) and the warm tail catcher (WTC, outside of cryostat) are shown as well.

The validity of the local hadron calibration approach was tested in a diploma thesis [46] utilizing as a first step the calibration constants derived for ATLAS. The results for linearity and resolution for charged pions in the EMEC/HEC region before and after calibration are depicted in figure 6.19 in comparison to the expectations for two different hadronic physics lists [43].

The linearity is found to be restored within 1% beyond 60 GeV and within 3 % below that energy. The resolution is improved by the calibration although the constants are not optimized for the test beam setup. The currently ongoing analysis of the test beam data therefore focuses on the performance with dedicated constants.

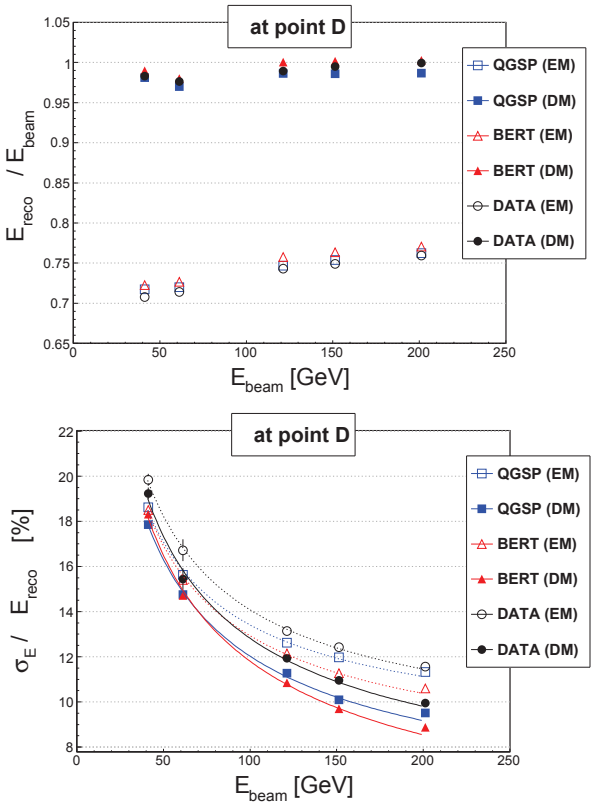

Figure 6.19: Linearity (upper plot) and resolution (lower plot) for charged pions in the EMEC/HEC region of the 2004 combined test beam. Open symbols are for uncalibrated, filled symbols for local hadron calibrated clusters. The data is compared to Geant4 simulations with QGSP and QGSP-BERTINI physics lists, respectively.

6.1.3 The Monitored Drift Tube Chambers MDT

The 88 Monitored Drift Tube chambers built at the Max-Planck-Institut für Physik were installed in the ATLAS experiment from February to June 2006, after being integrated with their respective trigger chambers and tested at CERN in 2005 [52, 53, 54, 55]. The chambers were the first to be mounted on the rail sys-

tem in the barrel part of the spectrometer and were positioned with an accuracy of about 1 mm [54], well within the specifications. The barrel part and the middle wheels of endcaps of the muon spectrometer were installed in 2006, the missing inner and outer endcap wheels followed in 2008, completing the muon spectrometer. 10 of 62 additional chambers improving the acceptance in the barrel-endcap transition region have been installed in 2009, the rest will follow in 2012.

The Max-Planck-Institut für Physik has taken a leading role in the commissioning of the ATLAS muon spectrometer and, via a representative in the ATLAS Muon Steering Group, is responsible for the overall coordination of the operation and maintenance of all MDT chambers since beginning of 2008. In addition, our MDT group provides on-call gas system and detector experts, as well as the data quality expert, who is responsible for the final sign-off of the MDT data. The MPP team is also involved in providing training and documentation for the shifters operating the detector in the ATLAS control room.

The commissioning of the MDT chambers should have followed their installation closely, but it was delayed due to the late installation of the final services in the experiment—the routing of the low and high voltage cables, readout fibers, and gas pipes and valves—and the availability of the commercially manufactured power supply boards. Thus, the commissioning phase of the muon spectrometer spanned from the end of 2006—with only 13 MDT chambers operational on temporary services—to September 2008, when the first beam was circulated in the Large Hadron Collider (LHC), and 98.8% of the 350000 channels of the 1088 MDT chambers of the muon spectrometer were operational.

A notable exception to the general commissioning strategy were the MPP MDT chambers: immediately after their installation and in regular intervals afterwards their gas tightness, HV stability and the stability of the chamber geometry has been tested [54]. As a result, these chambers exhibited less problems than other types when finally put into operation. The chambers were connected to the ATLAS gas system in 2007 and to the power supplies and read-out chain in 2008 by a team of 3 technicians and 4 physicists from MPP. Due to their exposed position at the outside of the ATLAS detector and the hostile environment with cooling and cryogenic stations and electronics racks on the surrounding structures nearby, the MPP chambers showed an increased noise pickup compared to the inner chambers. The situation was remedied by designing additional low-pass filters for the high voltage lines which were mounted on all MPP chambers in 2008 [56]. These filters are now also used on other chambers in the muon spectrometer which suffer from high noise rates.

The commissioning of the ATLAS muon spectrometer encompasses the connection of services to the chambers and the electronic racks in the experimental cavern. The MPP team supported this global work with 1–2 technicians and 2–4 physicists during 2007 and 2008. About 50% of all barrel MDT chambers were connected by the team and subsequently integrated in the read-out and debugged. Faulty front-end electronics cards were exchanged and high voltage failures due to a few broken anode wires in the drift tubes or dirt in the Faraday cages—caused by the ongoing installation of other subdetectors—were fixed. The channel mapping of the optical fibers for the read-out and the high and low voltage cabling of the whole spectrometer was verified and corrected. After the chambers had been integrated in the read-out of the experiment, data taken with cosmic ray muons is used to verify their proper operation and test their performance [57, 58]. Figure 6.20 shows an overview of the number of MDT chambers read-out as a function of time, denoted by periods of either combined muon system cosmic data taking (P-weeks) or combined cosmic data taking of all ATLAS subdetectors (milestones, M-weeks). An event display of one of the first recorded cosmic muons traversing the entire muon spectrometer during the P4 period is shown in Figure 6.21.

A major part of the commissioning phase consisted of taking into operation the recirculating MDT gas system—-the largest gas system of any LHC experiment. This effort was coordinated and to a large part executed by the MPP team. The system consists of 15 distribution racks serving 226 individual gas manifolds, each connected to 4 to 32 MDT chambers. The total gas volume of 2.2×10^6 bar L is exchanged once every 24 hours, and about 10% of the gas is replaced. In addition to the 2.8 million O-ring seals of the on-chamber gas distributions, the systems has about 4500 manual valves and 18000 connections. Stringent requirements exist for the allowed leak rate which should not exceed $2 \cdot 10^{-7}$ bar L/s per drift tube to avoid back diffusion of air into the system which would change the space to drift relation and degrade the drift tube efficiency. The vast majority

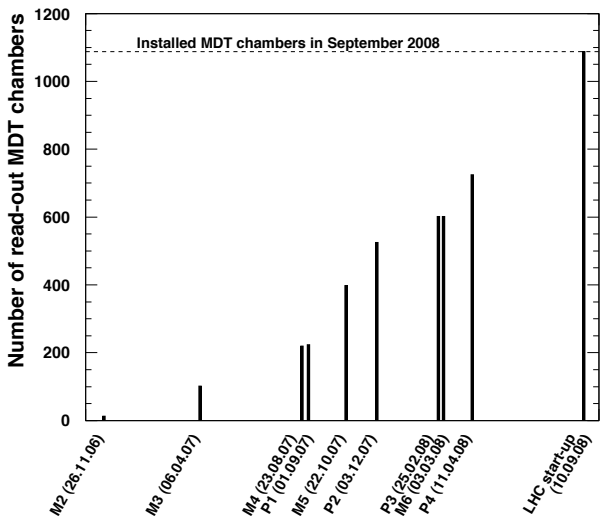

Figure 6.20: Number of MDT chambers read-out as a function of time from Nov. 2006 to the LHC start-up in Sep. 2008. P*i* denotes the *i*th combined muon data taking, M*i* denotes the *i*th milestone of combined data taking of the ATLAS detector components.

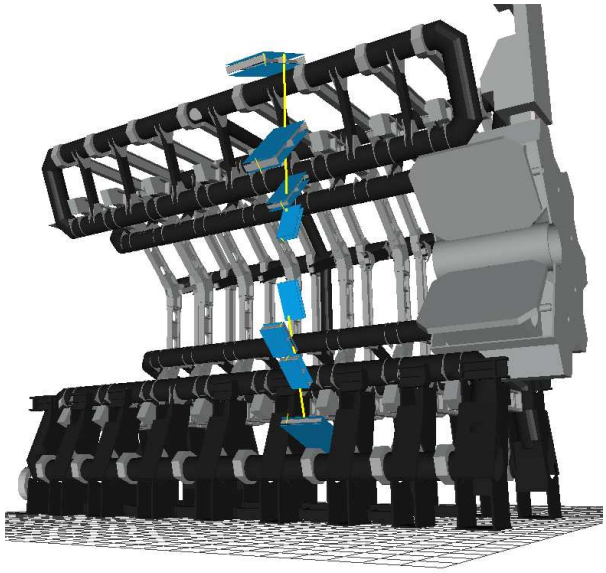

Figure 6.21: A cosmic muon traversing the ATLAS muon spectrometer, recorded during the P4 period in 2008. Only the MDT chambers with hits close to the reconstructed track and part of the toroid magnet system is shown. The topmost MDT chamber was built at MPP.

of all chambers and connections fulfills the tightness requirements after several hundreds of leaks were repaired. At the moment, the total leak rate of the system is about 30% higher than the allowed limit, caused by several larger leaks which will be repaired during the next LHC shutdown when access is possible. No adverse effect of the larger leaks has been observed so far. The purging of all MDT chambers, the leak search and repair, and the adjustment of the distribution system took an estimated manpower of 1.5 man years during 2007 and 2008. Periodic leak tests are still performed to spot new leaks in the system.

As all other subdetectors of the ATLAS experiment, the MDT system has entered routine operation in 2009 and 2010. Annual failure rates of the active and passive front-end electronics on the chambers, the high voltage distribution, and the detector control system are all well below 1%, but the more than 50000 different components nevertheless requires a continuous maintenance of the system to which the Max-Planck-Institut für Physik contributes a major share of manpower and expertise. The MDT system has been operational with 99.7% of all channels taking high quality data for the past two years.

Muon Detector Commissioning with Cosmic Rays

The MPP group is contributing to all aspects of the software development for the analysis of the ATLAS muon detector data, including the calibration of the space drift-time relationship of the MDT chambers [59, 60, 61, 62, 63, 64, 65], the alignment of the muon spectrometer with muon tracks [54, 56, 66, 67, 68, 69, 70], the evaluation and monitoring of the data quality of the muon detector [71, 72], optimisation of the muon reconstruction for the high background rates expected at the LHC [68, 73], and the Monte Carlo simulation programs for the muon spectrometer [74, 75]. The first two projects which are of central importance for the operation and performance of the ATLAS muon spectrometer and in which the MPP group plays a leading role are discussed in more detail in the following.

Drift Tube Calibration. The pressurised drift-tube technology has been chosen for the ATLAS muon tracking chambers because of the high spatial resolution of better than 80 μm which can be achieved for individual drift tubes by measuring the drift time of the ionisation electrons to the sense wires. In order to reach the required spatial resolution of the chambers of 40 μm not only the the sense wires have to be positioned in a chamber with an accuracy of 20 μm but also the space drift-time relationship of the approximately 400,000 drift tubes in ATLAS has to be known with the same precision. The drift properties of the electrons depend on the temperature and pressure of the drift gas as well as on the magnetic field and the rate of

background hits from neutrons and photons which can be very high at the Large Hadron Collider (LHC). For the regular calibration of the space drift-time relationship, correlations between the positions measurements of the drift tubes hit by a traversing muon can be used.

We have developed fast and efficient algorithms for the determination of the space drift-time relationship [59, 53] and of the spatial resolution [60] of the MDT chambers which are now part of the ATLAS data reconstruction software. The algorithms have been extensively tested with simulated data, cosmic ray commissioning data [58, 59], in a muon beam at CERN [61, 62] and under LHC operating conditions, in magnetic fields and at high background rates, using test beam data taken by our group at the Gamma Irradiation Facility at CERN [63]. A model for magnetic field corrections to the space drift-time relationship has been derived from the measurements [64].

The large sample of cosmic ray muons recorded by the ATLAS detector in 2008 and 2009 allowed detailed studies of the robustness of the calibration algorithms. The *r-t* calibration algorithm showed robust operation for all the chambers apart from the chambers with muons at 30° incidence angles where all drift radii are equal. The *r-t* calibration method originally applied to straight track segments in triplelayers of the muon chambers had to be extended to curved track segments in the muon chambers to achieve the same level of robustness for all muon chambers [76]. Figure 6.22 shows the accuracy of the space drift-time relationship provided by the improved calibration algorithm as a function of the number of collected muon track segments in a chamber for simulation and cosmic ray data. The required accuracy of 20 μm is reliably achieved with 3000 muons per chamber for all chambers of the muon spectrometer. The predicted accuracy is confirmed by the studies with muons from cosmic rays.

The dependence of the drift time on the magnetic field strength measured with cosmic rays in the ATLAS detector agrees well with the model based on the test beam measurements (see Figure 6.23).

The MPP group is operating one of the three computing centres dedicated to the calibration and the alignment of the ATLAS muon spectrometer [65] using a special data stream of muon tracks reconstructed by the ATLAS second level trigger algorithms. The commitment of the MPP group to calibrate roughly one third of the MDT chambers and to align the muon detectors with muon trajectories includes the development of fully automated calibration and alignment procedures and monitoring tools [77].

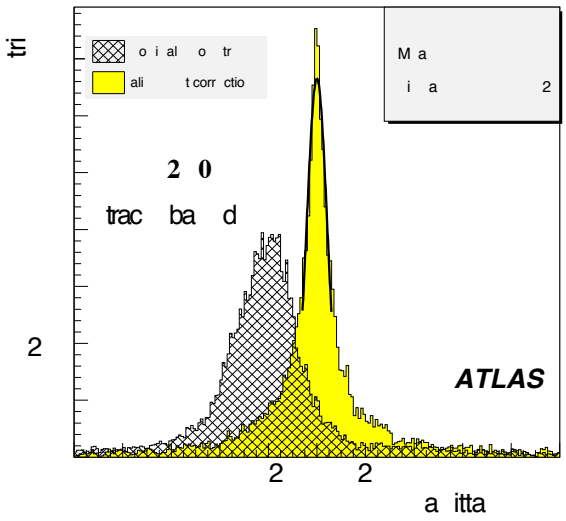

Figure 6.24: Sagitta distributions of straight cosmic ray muon tracks before and after the alignment with tracks. The mean value is on the order of a mm before the alignment procedure consistently with the mechanical installation accuracy. The mean value of the distribution is shifted towards 0 and its width is reduced by the track alignment procedure.

Muon Chamber Alignment with Tracks. To achieve the required momentum resolution of the ATLAS muon spectrometer up to the highest muon energies, the relative positions of the chambers have to be continuously monitored and misalignment corrections have to be applied to the measured track sagitta with an accuracy of 30 μm. The MPP group contributed significantly to the development and test of the high-precision optical alignment monitoring system for the muon spectrometer [48]. The group also developed algorithms for the alignment of the ATLAS muon spectrometer with muon tracks [66, 67, 68, 69, 70].

In the barrel part of the spectrometer, only the large chamber sectors mounted in between the magnet coils can be fully aligned with optical sensor measurements. The small chamber sectors mounted on the coils (see Figure 6.3) have to be aligned with respect to the large sectors with muon tracks passing through the overlap regions between the the small and large sectors. The MPP group is providing these alignment corrections using the muon calibration data at the Munich calibration and alignment computing centre [65, 66].

Straight muon tracks measured while the toroid magnets are turned off are needed for the precise determination the initial chamber positions after installation

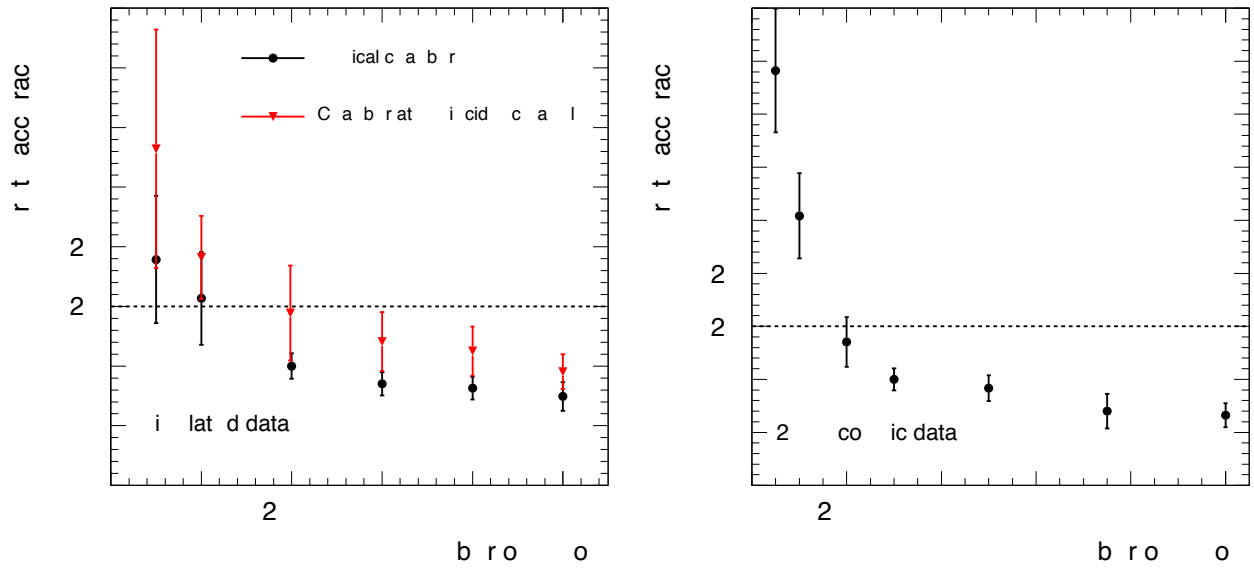

Figure 6.22: Accuracy of the calibration of the space drift-time relationship of the drift tubes of the ATLAS MDT chambers as a function of the number of cosmic muon tracks used per chamber. Left: Simulated data. Right: Cosmic ray data confirming the predicted *r-t* accuracies.

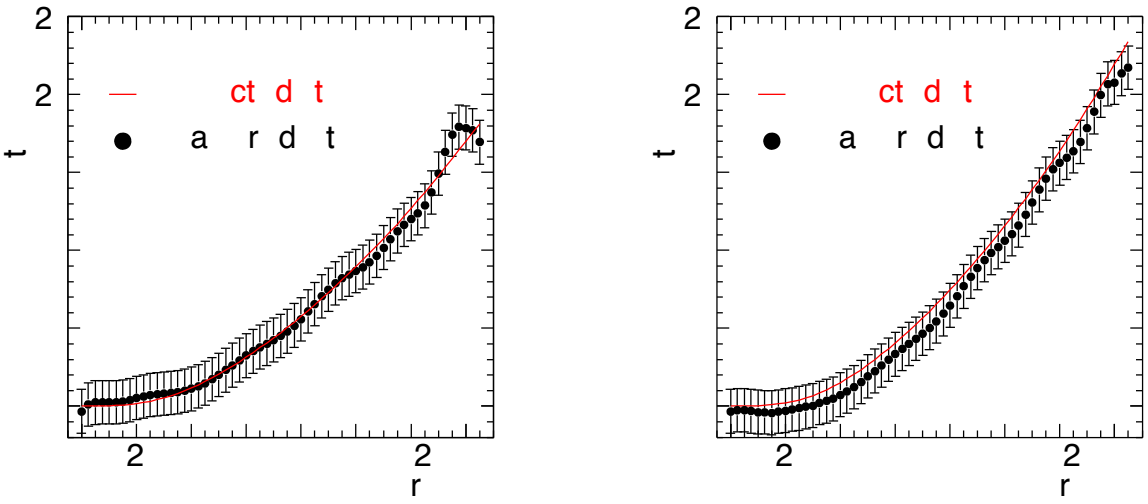

Figure 6.23: Magnetic field corrections to the drift time t in different regions of magnetic-field strength (0.47 T on the left, 0.54 T on the right) in MDT chambers in the middle layer of the large sectors of the barrel muon spectrometer as a function of the drift distance r. The measured difference in the drift times with and without magnetic field B agrees well with the model expectation in red derived from test beam measurements. The error bars of data points correspond to the estimated *r-t* accuracy of 20 μm. The drift time correction increases with the distance to the wire because of the deflection of the drifting electrons in the magnetic field oriented in the direction of the tube axis.

as a starting point for the monitoring of further chamber movements by the optical sensors mounted on the chambers. An efficient algorithm has been developed and successfully applied to cosmic ray commissioning data [67]. Figure 6.24 shows the mean value of the apparent sagitta of straight cosmic muon tracks after the initial alignment with straight cosmic muon tracks. In Figure 6.25 the mean value of the apparent sagitta distributions of the large sectors are shown as a function of the position of the MDT chamber along the z-direction (parallel to the beam pipe). The accuracy of the initial alignment is of the order of 50 μm or better and close to the desired ultimate accuracy of 30 μm. Improvements of the alignment accuracy are

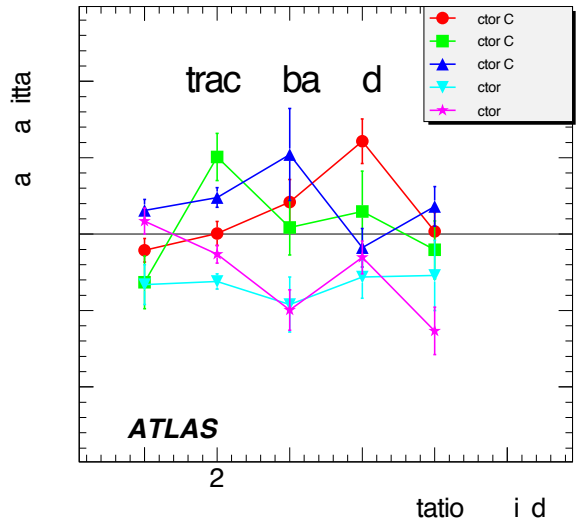

Figure 6.25: Mean value of the apparent track sagitta distributions obtained using a track-based alignment (large sectors). The station index describes the position of the MDT chamber along the z-direction (parallel to the beam pipe). The achieved accuracy of the alignment is independent of the sector and station index.

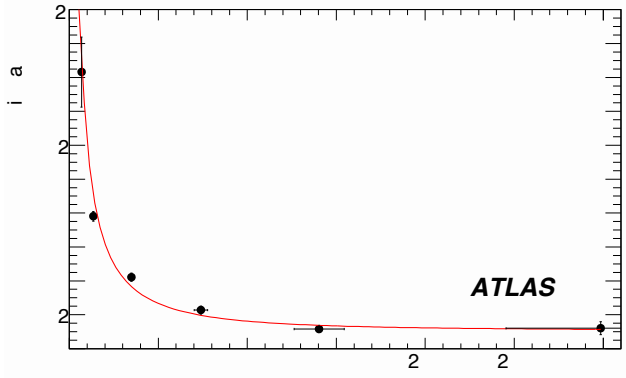

Figure 6.26: Resolution of the sagitta measurement as a function of the muon momentum as measured in ATLAS cosmic ray data. The red line illustrated the fitted resolution which is the quadratic sum of a term proportional to the inverse momentum taking into account multiple scattering and a constant term (of 100 μm) reflecting the limitation of the resolution by the spatial resolution and the alignment of the muon chambers.

expected when chamber deformations will be taken into account in the track reconstruction. The measurement of the sagitta resolution of straight tracks in the muon spectrometer as a function of the muon momentum measured by the inner detector is presented in Figure 6.26. It improves with increasing momentum as multiple scattering decreases with increasing momentum ans reaches a plateau value of about 100 μm at high momenta reflecting the limited spatial resolution and the residual misalignment of the muon chambers. The achieved resolution is about a factor 2 larger than the target value of 50 μm because the chambers are only aligned with 50 μm instead of 30 μm precision.

The method is being extended to the alignment of the muon chambers with curved muon tracks in the magnetic field during normal operation of the experiment in order to verify the optical alignment corrections. This requires an independent measurement of the muon momentum which is insensitive to misalignment of the MDT chambers along the muon track. The MDT chambers with their two triple or quadruple layers of precisely positioned drift tubes measure not only track coordinates with high accuracy but also the local track direction. This feature can be utilised for independent momentum determination from measurement of the track deflection angles between the inner and the outer chamber layer and between the two multilayers of the chambers in the middle layer located inside the magnetic field. Studies with simulated data showed that the required alignment accuracy can be achieved within two days of data taking at the nominal LHC luminosity of 10^{33} cm^{-2}s^{-1} [68, 70].

Muon Identification Performance

The huge sample of cosmic ray muons made it possible to study the performance of the muon identification in great detail up to muon momenta of 300 GeV/c [78, 79]. Figure 6.27 shows the track reconstruction efficiency in the ATLAS muon spectrometer for cosmic ray muons reconstructed in the inner detector. The efficiency is close to 100% in the instrumented regions of the muon spectrometer. The drop of the efficiency at $|\eta| = 0$ is caused by the acceptance gap of the muon spectrometer which is needed for the services of the inner detector and the calorimeters.

The momentum of cosmic ray muons traversing the entire ATLAS detector are measured twice, first in the top part of the muon spectrometer, then in the bottom part of the muon spectrometer. The comparison of the two momentum measurements allowed us to measure the fractional momentum resolution of the muon spectrometer up to muon with $p_T = 300$ GeV/c (see Figure 6.28). The measured momentum resolution is in agreement with the expected momentum resolution for $p_T \lesssim 100$ GeV/c, but is a factor 2-3 worse than expected above 300 GeV/c due to the residual misalignment of the muon spectrometer.

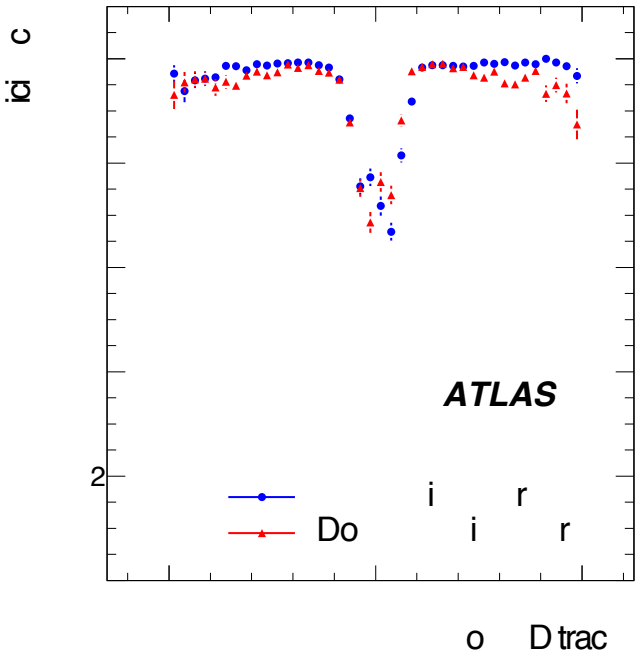

Figure 6.27: Track reconstruction efficiency in the muon spectrometer as a function of the pseudorapidity of the cosmic ray muon reconstructed by the inner detector. The muon momentum in the inner detector was requested to be greater than 5 GeV for the top part and greater than 9 GeV for the bottom part. The loss of efficiency in the region near $|\eta| = 0$ is due to acceptance holes of the muon spectrometer needed for services of the inner detector and the calorimeters.

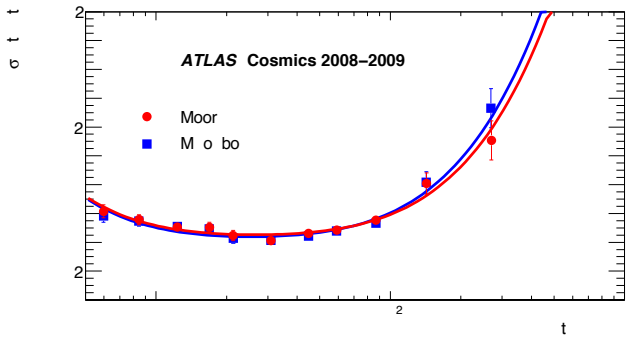

Figure 6.28: Transverse momentum resolution of the muon spectrometer evaluated by comparing the momentum of cosmic ray muons measured in the top part of the spectrometer with the momentum in the bottom part of the spectrometer in the barrel region of the muon spectrometer. The results of two complementary track reconstruction algorithms show similar performance.

The muon reconstruction efficiency and the momentum scale and resolution will be measured for low p_T with $J/\Psi \rightarrow \mu^+\mu^-$ decays and for high p_T with $Z \rightarrow \mu^+\mu^-$ decays in pp collision data at the LHC [80, 81]. First $J/\Psi \rightarrow \mu^+\mu^-$ events have been observed by the ATLAS experiment. The invariant mass distribution of the $J/\Psi \rightarrow \mu^+\mu^-$ events is shown in Figure 6.29

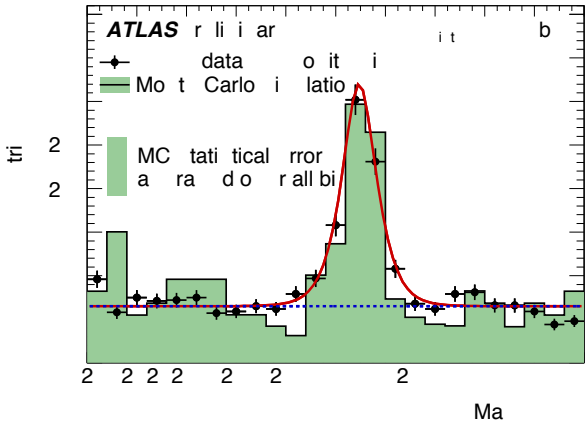

Figure 6.29: Invariant mass distribution of reconstructed $J/\Psi \rightarrow \mu^+\mu^-$ candidates. The points with error bars are data. The solid line is the result of maximum likelihood unbinned fit to all di-muon pairs in the mass window 2-4 GeV and the dashed line is the result for the background of the same fit. MC from both prompt J/Ψ and minimum bias simulation are superimposed.

The position of the Z resonance peak is a measure for the momentum scale, its width a measure for the momentum resolution. The muon reconstruction efficiency will be measured by the so-called "tag-and-probe method". In the tag-and-probe method events with an isolated muon and an inner detector track giving an invariant mass compatible with the Z boson mass are selected. The fact that one of the two tracks is identified as muon ensure that the second track is also a muon and one can count how often the second track is reconstructed as a muon. The method has been studied on Monte-Carlo data and is able to reproduce the muon reconstruction efficiency with a systematic uncertainty of 0.2%.

First $Z \rightarrow \mu^+\mu^-$ candidate events have been observed in the ATLAS detector. One such event is shown in Figure 6.31. In the early phase of the LHC operation the rate of dimuon decays of Z bosons is too low for the tag-and-probe method and alternative methods have to be used to get a handle on the muon spectrometer reconstruction efficiency. The efficiency of the standard muon reconstruction is measured with respect to an alternative muon identification approach. In the alternative approach an inner detector track which deposits only little energy in the calorimeters and which can be matched with a track segment

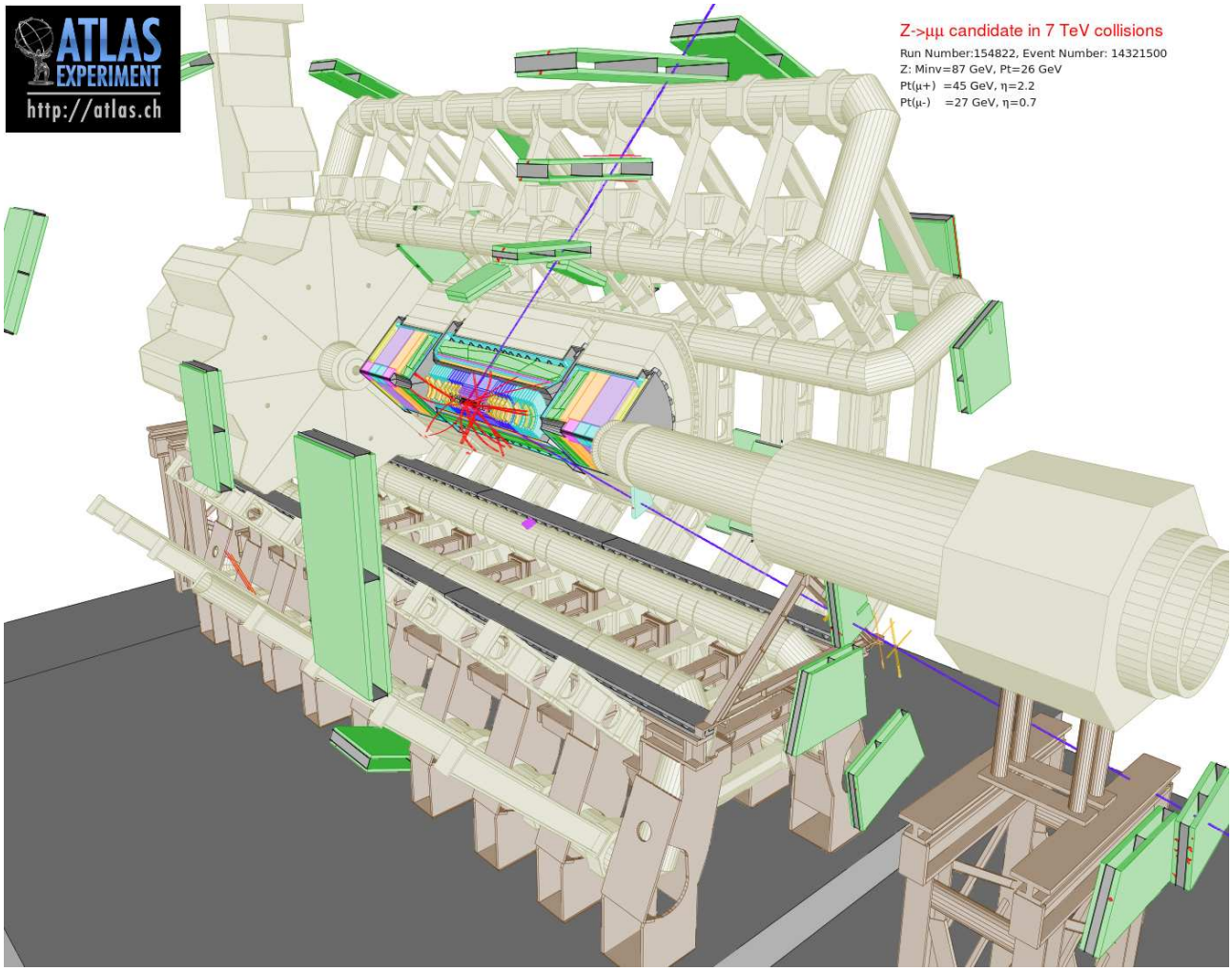

Figure 6.31: Event display of a $Z \rightarrow \mu^+\mu^-$ candidate event recorded at a centre-of-mass energy of $\sqrt{s} = 7$ TeV

in the muon spectrometer is identified as muon. The relative efficiency of the standard muon reconstruction with respect to the alternative selection is shown as a function of the transverse muon momentum in Figure 6.30 [82]. The relative efficiency agrees with the Monte-Carlo prediction within errors. It is lower than the true efficiency as the alternative muon selection has a lower rejection power against muons from pion and kaon decays in flight than the standard reconstruction.

At transverse momenta below 20 GeV/c the momentum resolution in the momentum resolution is significantly larger than in the inner detector and can be measured by comparing the momentum measured in the muon spectrometer with the momentum measured in the inner detector. The resolution measured this way is in agreement with the Monte-Carlo prediction and the measurement with cosmic ray muons within the measurement uncertainties (see Figure 6.32) [83].

The analysis of cosmic ray data and the first results of the analysis of pp collision data confirm the expected performance of the muon spectrometer.

6.1.4 Computing

The rate of triggered and filtered data from the experiment data acquisition system (DAQ) will be about 200 beam-crossing events per second. This rate translates to more than 300 MB/s given an expected event size of ca. 1.6 MB. When the additional data generated by event reconstruction is taken into account, several PB of physics data per year will have to be handled by the ATLAS computing system [84, 85, 86].

ATLAS Computing Model

The ATLAS computing model [84] is based on the established procedure of performing several successive steps of data reduction. The data coming from the DAQ is termed RAW data and will be passed through

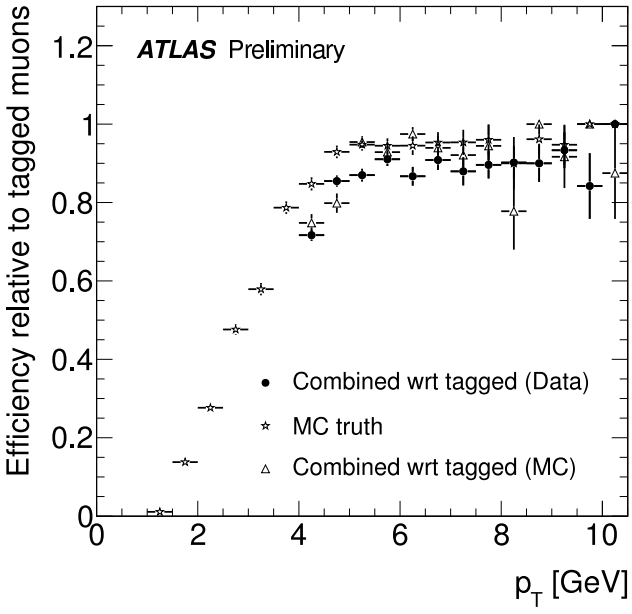

Figure 6.30: Comparison of the relative efficiency of the standard muon reconstruction algorithm with respect to reference muons as defined in the text with the Monte-Carlo prediction for $p_T > 4$ GeV/c. The star-shaped symbols labelled as MC truth show the standard muon reconstruction efficiency for muons identified as true muons in the simulation.

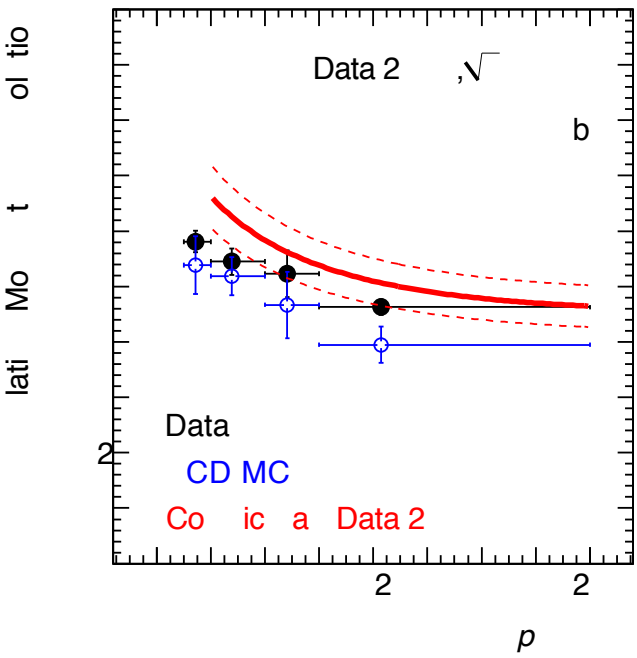

Figure 6.32: Comparison of the momentum resolution in the barrel part of the muon spectrometer measured with muons from pp collisions in comparison with the expected resolution from Monte-Carlo data and the analysis of cosmic ray data. The measured resolution agrees with the prediction within the measurement uncertainties.

the event reconstruction immediatly after recording (prompt reconstruction). The next step of data reduction leads to event summary data (ESD, about 500 kB/event) consisting of reconstructed particle tracks and calorimeter clusters and the corresponding hits after noise supression. The last step of central data reduction results in the analysis object data (AOD, about 100-200 kB/event) where essentially only the reconstructed particle momenta and identity information is kept. The working groups in ATLAS can define their own derived physics data (DPD), which are typically 10 kB/event.

The ATLAS computing system [85] is organized in a hierarchical manner with three levels (or tiers) of distributed and interconnected computing centers mapped approximately to the different levels of reduced data. The single Tier-0 center at CERN serves the four LHC experiments and provides mass storage of raw data and processing capacity for the prompt reconstruction. The reduced data (ESD and AOD) are distributed to the Tier-1 centers along with the RAW data.

ATLAS has ten Tier-1 centers; one of them is operated by the FZ Karlsruhe (GridKa). The responsibility of the Tier-1 centers is to store between them a copy of the RAW data, provide processing capacity for deriving ESD/AOD data from RAW data (reprocessing) and to make ESD and AOD data sets available for organized physics analyses.

Each of the Tier-2 centers in turn are connected to one of the Tier-1 centers. There are about 30 Tier-2 centers serving ATLAS and their responsibility is to provide processing capacity to run the ATLAS simulation and to run scheduled and unscheduled physics analyses by working groups or individual users with AOD data. In addition the derivation of calibration constants may be performed at Tier-2 centers. The Tier-2 centers will each hold approximately 1/3 of the total AOD data such that the usually three Tier-2 centers connected to a regional Tier-1 center together hold the entire AOD data set.

The Tier-3 centers correspond to local computing facilities operated at institutes and dedicated to the local ATLAS groups.

Worldwide LHC Computing Grid

The WLCG collaboration lead by CERN with all major institutes participating in the LHC as partners provides the computing resources needed for timely and successful analysis of the LHC experiments data [87].

One of the most important goals of the WLCG is to deliver the neccessary software to manage the distributed data storage and computing tasks as well as to give transparent access to the data to all collaborators of an LHC experiment.

The Institute is an official member of the WLCG collaboration. It is the responsibility of the ATLAS group at MPP to contribute a large fraction of the resources needed to build and operate a Tier-2 center in Munich for use by the ATLAS collaboration.

Munich Tier-2/3 Computing Center

The two ATLAS groups in Munich at the MPP and the LMU (LS D. Schaile) have agreed to build and operate a Tier-2 center for ATLAS of the average size as specified in [84]. The center is hosted by the RZG and the Leibniz Rechenzentrum (LRZ) in Garching. The four parties MPI, LMU, RZG, and LRZ have signed a memorandum of understanding (MOU) outlining the details of the project.

The contributions of MPP/RZG and LMU/LRZ are expected to be about equal in size. It is foreseen to add 100% of the CPU resources and 50% of the storage ressources needed for the Tier-2 center in order to support local computing requirements for the Munich calibration and alignemnt centre and at the Tier-3 level. The hardware is one homogeneous setup and the sharing of resources between Tier-2, MCAC and Tier-3 can be adjusted during operation according to the needs of the experiment or the local working groups.

The hardware is located on the sites of the two computing centers RZG and LRZ in Garching. Such a federation of computing centers is explicitly foreseen in the WLCG to operate a common Tier-2 service.

The total resource requirements for the Munich Tier-2/3 computing centre for 2010 are estimated as 11.8 kHS06[1] for data processing and 650 TB for data storage on disk. This corresponds to approximately 1700 CPU cores and about 33 fileservers with 20 TB RAID storage each. A wide area network (WAN) connection with a sustained bandwidth of 30 MB/s is supplied by RZG for import and export of data.

MPI Computing Facility at RZG

The computing facility serves the whole institute and the main users are currently the ATLAS and MAGIC groups.

[1] 7 HS06 correspond roughly to one core of a AMD or Intel multicore CPU from 2009

The system consists now of 8 IBM BladeCenter H equipped each with 14 single-board computers. Common services such as power supply and LAN are provided by the BladeCenter. The single-board computers have two CPUs (Intel Xeon 3.2 GHz or Xeon 54xx quad-core), 2 GB RAM/core and a bandwidth of 1 Gb/s to the LAN. Data are stored on integrated fileservers, which connect 12, 16 or 28 large SATA harddisks (currently 300, 500 or 750 GB) each to RAID arrays via dedicated PCI expansion cards. The total useable disk space is more than 300 TB.

The RZG maintains the operating system (OS), currently Suse Linux Enterprise Server (SLES) 10, batch queue system (Sun grid engine SGE), and other system services. The mass data storage system dCache developed by DESY and FNAL has also been installed and is used by ATLAS. The MPP user groups, e.g. ATLAS, have to install and maintain their own experiment software on this platform.

The RZG operates several servers running the LCG software needed to connect the MPP computing facility to the WLCG. One person from MPP seconded to RZG runs together with staff from RZG the WLCG services, responds to problem reports, installs upgrades, and interacts with our users. Some of the WLCG services run as virtual machines [88], since this makes it more convenient to use the required Scientific Linux OS instead of SLES10 as is standard at RZG.

6.2 ATLAS Physics Analysis

Since long the MPP ATLAS group continuously works on the preparation of physics analysis of hadron collision data at the LHC. The results obtained in the years 1997-2007, including preparatory work based on Tevatron data, are described in the previous reports [89, 90, 91], and references therein.

The present physics studies for the ATLAS experiment cover a broad physics range. Already at this early stage of data taking, a number of Standard Model (SM) processes occur in abundance. These processes allow for detailed studies of the detector performance, as well as for the precision measurement of QCD and electroweak observables. In this respect the top-quark physics is of particular interest. A good understanding of SM processes is essential also for new discoveries. The ATLAS discovery potential is explored in searches for the Higgs boson both in the Standard Model and in supersymmetric extensions, as well as

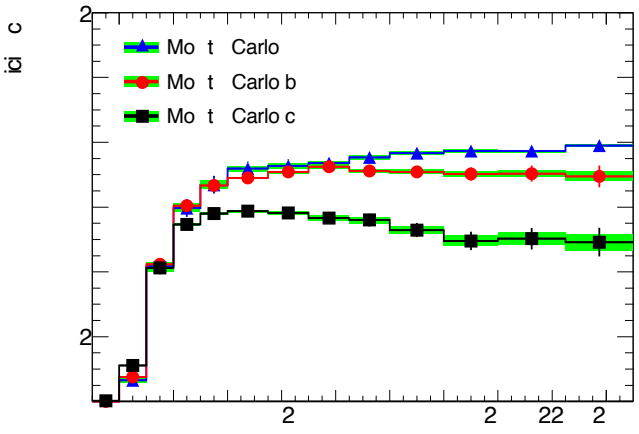

Figure 6.33: Monte-Carlo prediction of electron reconstruction efficiency for electrons from heavy quark and Z boson decays after the optimization of the electron identification cuts.

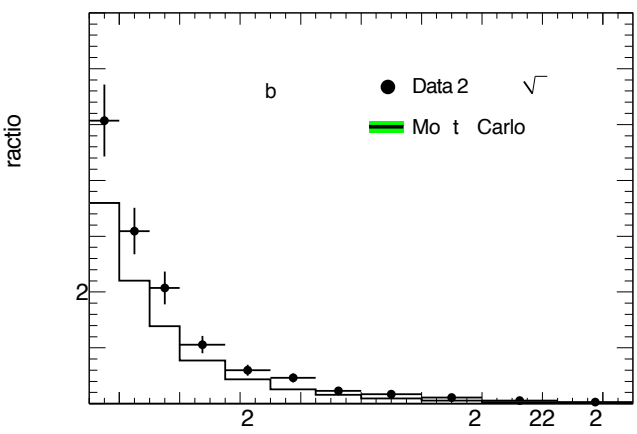

Figure 6.34: Comparison of the measured distribution of the transverse energies of prompt electrons from c and b decays with the Pythia 6.4 minimum bias Monte-Carlo predictions. [94]

in a generic search for supersymmetric particles. The ongoing investigations are described in more detail below.

6.2.1 Measurement of Standard Model Processes

Measurement of Inclusive Lepton Cross Sections

At the LHC pp collision events with highly energy electrons and muons in the final provide clean signatures for many physics processes of interest. A good understanding of the inclusive electron and muon cross section is therefore of great importance. The MPI group contributes to the measurement of the inclusive electron and muon cross section [92, 93, 94].

At the LHC electrons are produced predominantly in decays of heavy quarks for transverse momenta below about 30 GeV and in decays of W and Z boson at higher transverse momenta. The MPI group significantly contributed to the optimization of the electron selection criteria to arrive at an electron selection efficiency which is flat in the transverse electron momentum (see Figure 6.33). The first measured inclusive electrons spectrum at a centre-of-mass energy of 7 TeV at the LHC shown in Figure 6.34 agrees with the prediction of the Pythia minimum bias Monte-Carlo prediction within about 20%. The MPI group contributes to the analysis of this discrepancy with increasing statistics of the inclusive electron sample.

The MPI group is also involved in the measurement of the inclusive muon cross section contributing with its experience in muon performance stud-

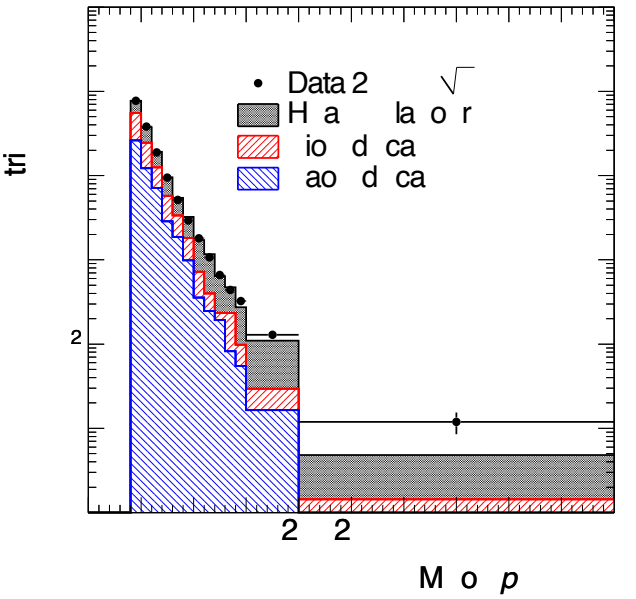

Figure 6.35: Comparison of the measured inclusive muon transverse momentum spectrum with the Pythia 6.4 minimum bias Monte-Carlo prediction. The Monte-Carlo data is decomposed into the three sources of muons, namely in-flight decays of charged pions and kaons and the decays of heavy-flavour hadrons. [93]

ies. The measured inclusive muon p_T spectrum is presented in Figure 6.35 where it is compared with the Pythia 6.4 minimum bias Monte-Carlo prediction. The measured spectrum is well reproduced by the Monte-Carlo simulation. The main sources of the muon at transverse momenta below 20 GeV are in-flight decays of charged pions and kaons and the decays of heavy-flavour hadrons according to the Monte-Carlo

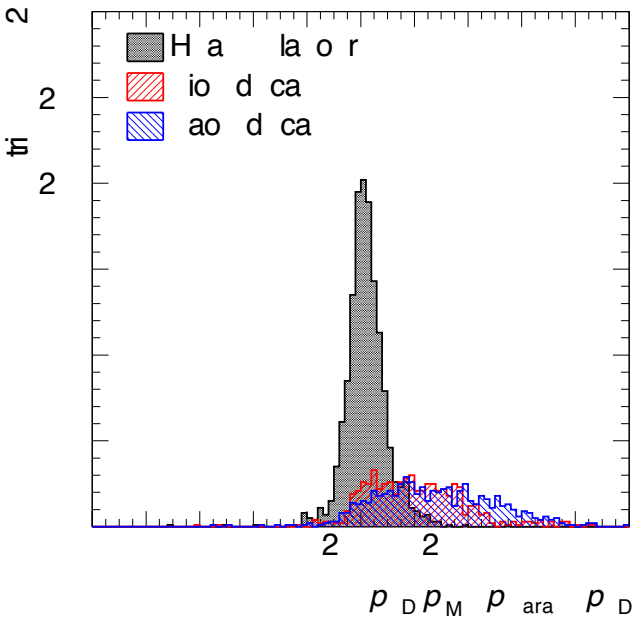

Figure 6.36: Distribution of the difference of the muon momentum measurements in the inner detector and the muon spectrometer normalized to the inner detector momentum measurements in simulated data. Decays of pions and kaons in flight lead to a large tail to positive values as the inner detector measures the pion and kaon momentum while the muon spectrometer measures the momentum of the decay muon. [93]

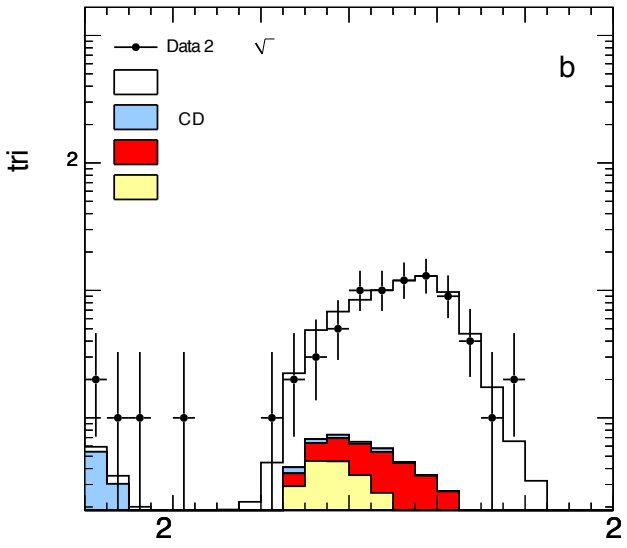

Figure 6.37: Transverse mass distribution of $W \rightarrow \mu\nu_\mu$ candidates found in the first 16 nb^{-1} of pp collision data collected by ATLAS.[95]

simulation. Decays of W and Z bosons become important for $p_T > 20$ GeV. The contribution of pion and kaon decays in-flight to the inclusive muon spectrometer will be estimated from data by comparing the momentum measured in the inner detector with the momentum measured in the muon spectrometer. For late pion and kaon decays in the inner detector lead to a large momentum inbalance between the inner detector and muon spectrometer as illustrated in Figure 6.36.

Study of Processes with Electroweak Gauge Bosons

Standard Model processes are studied with the motivation of estimating the backgrounds to the production of Higgs bosons and supersymmetric particles from the data and to improve the Monte Carlo simulations. The processes under investigation are QCD high p_T and multi-jet production, forward jet production, b jet production, inclusive W, Z and $t\bar{t}$ production as well as $Z \rightarrow \tau^+\tau^-$ decays. $Z \rightarrow e^+e^-$ and $\mu^+\mu^-$ decays are being studied for the purpose of detector calibration and data quality monitoring. The analysis methods developed will be applied to first measurements of multi-jet, $b\bar{b}$ and inclusive W and Z production cross-sections with the early data.

Figure 6.37 shows the transverse mass distribution of the $W \rightarrow \mu\nu_\mu$ candidates in the first 16.6q nb^{-1} of pp collision data collected by ATLAS. The measured distribution is consistent with the Monte-Carlo prediction and has a negligible background contamination. In the same set of pp collision data ATLAS has observed 8 Z boson candidates as can be seen as an excess of entries at the Z mass in the dimuon mass spectrum of Figure 6.38 [95].

A first measurement of the W production cross section could also performed. The measured W production cross section agrees well with the NNLO calculations as shown in Figure 6.39.

%— — — — — — — — — — — — — — — — — — —

6.2.2 Top-Quark Physics

Overview

The top-quark is by far the heaviest known elementary building block of matter. The precise knowledge of the quantum numbers of the top-quark helps to further constrain the parameters of the Standard Model, and is a mandatory prerequisite for any study of new physics that will almost inevitably suffer from top-quark reactions as background processes. In addition, the top-quark should have the strongest couplings to any mechanism that generates mass, which makes it a

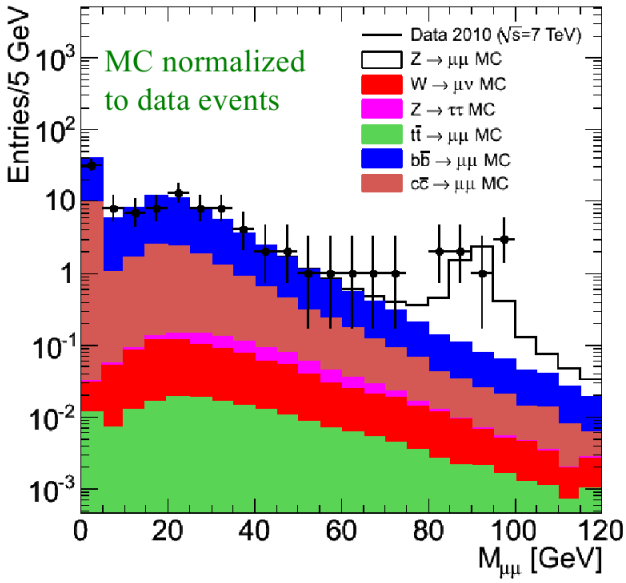

Figure 6.38: Invariant dimuon invariant mass distribution for isolated muonss in the first 16 nb^{-1} of pp collision data collected by ATLAS. An excess of 8 Z events is visible in the distribution consistent with the Monte-Carlo prediction.

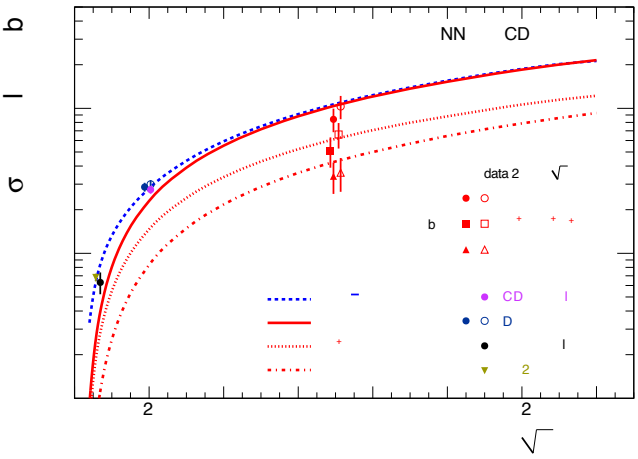

Figure 6.39: Comparison of the measured W cross section with the NLLO prediction. [95]

very interesting object for an unbiased search for this mechanism.

The present main interest of the top-quark physics analysis work of the MPP group is the investigation of the $t\bar{t}$ production process, and particularly the determination of the mass of the top-quark (m_{top}) and the production cross-section ($\sigma_{t\bar{t}}$) in the reaction $t\,\bar{t} \rightarrow b\,\bar{b}\,W^+\,W^-$.

The analyses use two decay channels of the W-boson pair, the lepton + jets channel, where the W-boson pair decays into $\ell\nu\,qq'$ with $\ell = e,\,\mu$ (branching ratio, $\mathcal{BR} = 30\%$) and the all-jets channel, where both W-bosons decay into a qq' pair ($\mathcal{BR} = 44\%$). In both channels m_{top} is obtained from hadronically decaying W-bosons and the corresponding b-jet.

The main background reactions to $t\,\bar{t}$ production, as determined from Monte Carlo simulations, are the W + n-jets production, QCD multijet production, single top-quark production, and that fraction of the $t\bar{t}$ production where the W-boson pair decays via the other decay channels. The QCD multijet production process is special due to the huge cross-section before any cut, such that event samples fully covering the signal phase space cannot be simulated with sufficient statistics, especially for the lepton + jets channel, where the selected lepton mostly results from a wrongly reconstructed jet. Eventually this background contribution has to be obtained from data. So far, initial studies of this background based on Monte Carlo samples have been performed and methods to evaluate it from the data, like the matrix-method, have been implemented. The matrix-method was successfully applied to estimate the background fraction from Monte Carlo samples with a deliberately unknown composition of signal and background events [96]. In the MPP investigations, for the first time the k_t-jet algorithm has been used in top physics analyses at ATLAS [17, 97] Because of a better stability against divergences, this algorithm is theoretically preferred over the traditionally applied cone-jet algorithm. By now also the experimental advantages became apparent, such that since recently a variant of it, namely the anti-k_t jet algorithm is the ATLAS standard.

At present the analyses are optimized on Monte Carlo samples and are ready to be applied to the data to be taken still this year. The analyses are mostly performed assuming the initially envisaged proton-proton center of mass energy of $\sqrt{s} = 10\,\text{TeV}$ and for integrated luminosities $\mathcal{L}_{\text{int}}$ of several 100 pb^{-1}. An overview of the recent activities is given below, the initial investigations were reported in [90, 91].

Lepton + Jets Channel

The lepton + jets channel is the best compromise of branching fraction and signal-to-background ratio (S/B), defined as the ratio of $t\,\bar{t}$ signal events to physics background events. Therefore most of the effort is invested in this channel. At MPP a number of analyses have been performed to arrive at the most sensitive observable and analysis strategy for obtaining m_{top} from the invariant mass of the three jets assigned to the decay products of the hadronically decaying top-quark.

Different event- and jet selection algorithms, observables, jet calibration schemes (see Sec. 6.1.2), and fitting methods have been exploited for this.

In the lepton + jets channel the charged lepton with a high transverse momentum[1] (p_T) from the decay of one W-boson is utilized to trigger and identify the event, and to efficiently suppress background without genuine charged leptons, i.e. from the QCD multijet production. In general, the event selection for the lepton + jets channel requires an isolated electron or muon within the good acceptance of the detectors, which has a transverse momentum of more that 20 GeV and lies within the rapidity range of $|\eta| < 2.5$. Since the initial state is balanced in p_T, to account for the neutrino a missing transverse energy of more than 20 GeV is required. In addition, at least four jets are required within the same range of rapidity, and having transverse momenta of more than 40 GeV for the three highest p_T jets, and more than 20 GeV for the fourth jet. All jets should be well separated from the identified lepton. Given the different emphasis of the analyses, these requirements are slightly modified or additional requirements like the presence of identified b-jets, or restrictions to the reconstructed invariant mass of the W-boson are imposed. With these selections, for each lepton sample an average signal efficiency of about 10% is reached, and the S/B is about 1.5.

The standard assignment of jets to the top-quark and the W-Boson are as follows. For each event, from all jets with $p_T > 20$ GeV the three jet combination which maximizes the transverse momentum is chosen to form the hadronically decaying top-quark. This algorithm is named the p_T-max method. Out of this, the two jet pair with the smallest ΔR is taken to represent the W-boson. A typical top-quark mass spectrum observed with these requirements [20], and only using signal events and W + n-jets events, is shown in Fig. 6.40. In this example, the spectrum is fitted with a Gaussian function to parameterize the correct combinations leading to the top-quark mass and width, and a sum of Chebyshev polynomials used to describe the events stemming from the sum of the physics background events and wrong jet combinations in selected

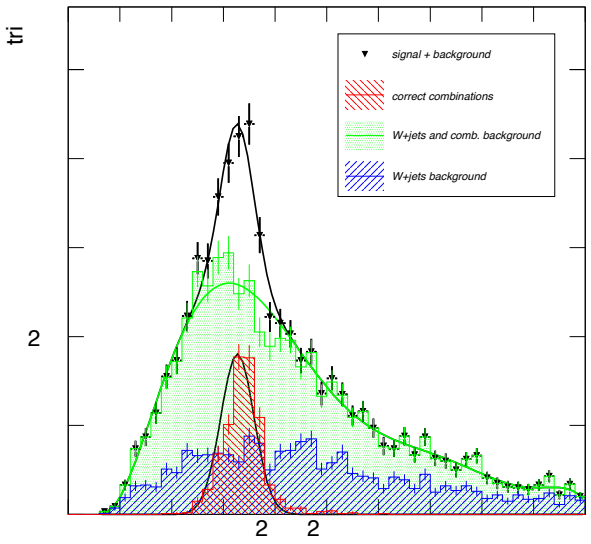

Figure 6.40: The reconstructed top-quark mass together with a fit.

signal events. The Gaussian part of the fit is also shown separately and compared to the red histogram made from the correct jet triplet. In this case correct jet triplets are defined as those combinations of jets where the reconstructed four-vector of the jet triplet coincides with that of the top-quark to within $\Delta R = 0.1$.

From this figure it is clear that firstly the correct jet triplets constitute only a small part of the events in the peak region around the generated top-quark mass of 172.5 GeV, secondly that the shape of the combinatorial background can well influence the fitted peak value, and thirdly that the shown W + n-jets contribution is still sizeable and not entirely flat.

These issues are addressed, e.g. by using other algorithms to select the jet triplet, or by exploiting additional variables or a constrained fit that both help to separate signal from background. Additional algorithms studied include the so-called ΔR method that exploits the angular correlations between the two b-jets that should have a large ΔR, and the two light-jets that should have a small ΔR. This algorithm works without explicitly using b-jet identification, instead from a p_T ordered jet list the first two jets are assumed to be the b-jets and the next two jets to stem from the W-Boson decay. On these jets the angular requirements are applied. Whether the decrease in statistical precision compared to the p_T-max method is compensated by superior features like an improved resolution, or a smaller bias in the reconstructed mass, is under investigation.

[1] In the ATLAS right-handed coordinate system the x-axis points towards the center of the LHC ring, the y-axis points upwards and the z-axis points in the direction of the counter-clockwise running proton beam. The polar angle θ and the azimuthal angle ϕ are defined with respect to the z-axis and x-axis, respectively. The pseudo-rapidity is defined as $\eta = -\ln(\tan(\theta/2))$ and the radial distance in (η, ϕ) space is $\Delta R = \sqrt{\Delta\eta^2 + \Delta\phi^2}$.

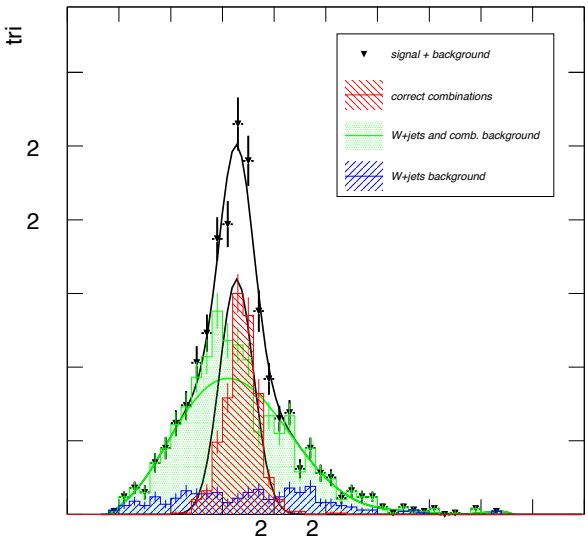

Figure 6.41: Same as Fig. 6.40 but with an additional likelihood selection.

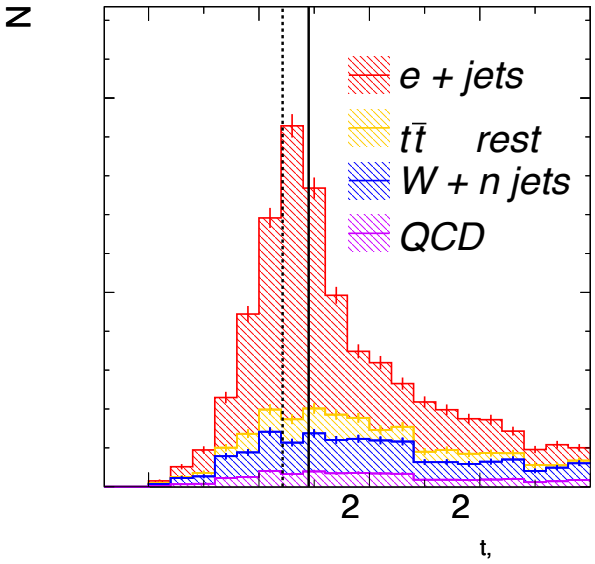

Figure 6.42: The top-quark mass distribution when applying a constrained fit selection.

Due to the presence of the decay of the top-quarks that correlate the W-Bosons and their corresponding b-quarks, the signal events should exhibit a different correlation of the observed jet structure than the background processes without top-quarks. The separation of the jets can be monitored when running the k_t-jet algorithm by studying the $d_{\text{merge}}(M \rightarrow M-1)$ values at which an M-jet configuration is reduced to an $(M-1)$-jet configuration. In a multivariate analysis it was found that the d_{merge} values in signal and background events are not sufficiently different to be used as discriminating variables [20]. In contrast, a likelihood function build from seven event variables, like e.g. the invariant mass of the charged lepton and its assigned b-jet, or the ΔR between the W-Boson and the b-jet from the hadronically decaying top-quark candidate, is clearly able to significantly improve the S/B, while retaining most of the events where the correct jet triplet was selected. This is demonstrated in Fig. 6.41.

A kinematic fit exploiting as constraints the known W-Boson mass both for the leptonic and the hadronic W-Boson decays, and in addition the equality of the two corresponding reconstructed top-quark masses mainly serves three purposes. Firstly, it increases the efficiency for selecting the correct jet triplet by making more detailed use of the entire event. Secondly, it provides a quality measure, namely the probability $P(\chi^2)$ of the fit, to better suppress background events. Finally, it improves on the resolution of the top-quark mass provided the uncertainties of the measured quantities and their correlations are properly understood, something that is only expected after a larger data set has been analyzed. Compared to the p_{T}-max method the efficiency for selecting the correct jet triplet is increased by about 15% absolute, and about 25% of the background events can be removed [98] by requiring $P(\chi^2) > 0.15$. An example of such a selection for events with four reconstructed jets and requiring $P(\chi^2) > 0.15$ is shown in Fig. 6.42. The better suppression of the W + n-jets events compared to Fig. 6.40 is apparent. It has been verified that this improvement, is very stable against variations of the assumed object resolutions. Since at the moment only initial approximations are made for the resolution of the objects, the possible improvement in the mass resolution is not yet exploited.

The largest systematic uncertainty in any determination of m_{top} stems from the imperfect knowledge of the jet energy scale (JES), which depends on kinematic properties like p_{T} and η of the jets, and is different for light-jets and b-jets. Therefore, one of the most important features of any m_{top} estimator is the stability against the variation of the JES. To minimize the JES uncertainty on the measured m_{top} two paths are followed: one is a calibration by means of the known W-boson mass ($M_{\text{W}}^{\text{PDG}}$) to obtain the JES for light-jets, the other is exploring the stabilized top-quark mass ($m_{\text{top}}^{\text{stab}}$, see below) to be as independent as possible of the actual JES value, without actually determining it.

In the lepton + jets channel an iterative in-situ cali-

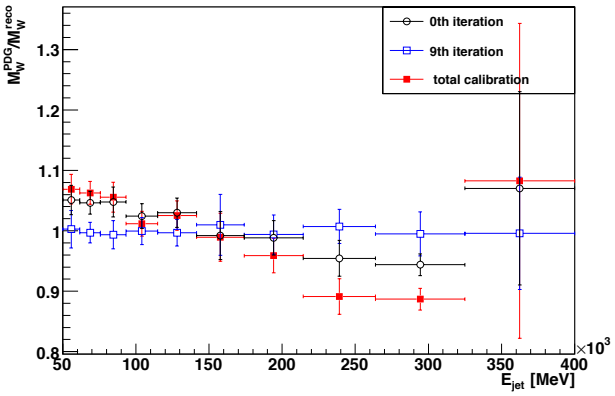

Figure 6.43: In-situ calibration of the W-Boson mass as function of the light-jet energy.

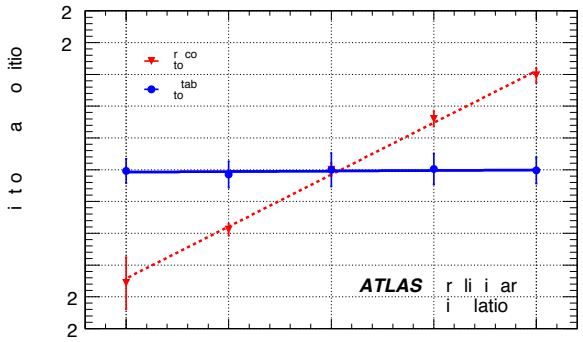

Figure 6.44: Stability of $m_{\text{top}}^{\text{reco}}$ and $m_{\text{top}}^{\text{stab}}$ against JES changes.

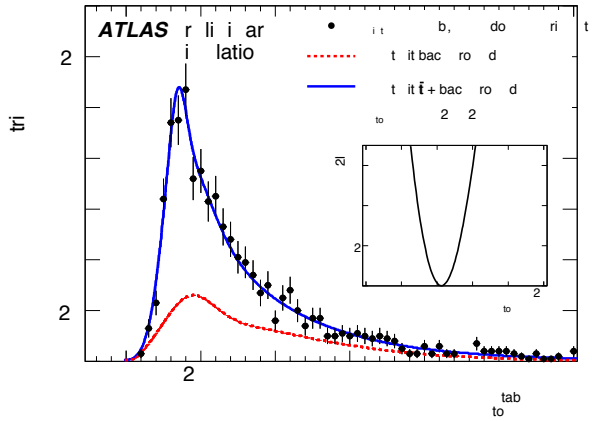

Figure 6.45: Pseudo-experiment mimicking early ATLAS data in the muon channel.

bration of the JES for the selected events has been performed [99]. Jets are treated in the massless limit with unchanged reconstructed angles, such that any change in the invariant two-jet mass ($M_{\text{W}}^{\text{reco}}$) can be expressed in energy dependent JES factors. The jet calibration then makes use of the fact that $M_{\text{W}}^{\text{reco}}$ calculated from the jets assigned to the W-boson decay has to match $M_{\text{W}}^{\text{PDG}}$. The energy bins are chosen logarithmically from 50 GeV to 400 GeV and the resulting calibration factors, which are consecutively applied per iteration, are shown in Fig. 6.43 for the initial situation, the 9$^{\text{th}}$ iteration and the final result. The flatness of the calibration factors of the 9$^{\text{th}}$ iteration with values close to unity clearly shows that the fit has converged. Comparing the initial and final situation reveals that the iterations slightly change the simple picture one would have obtained by once adjusting the peak of the initial distribution to $M_{\text{W}}^{\text{PDG}}$. When applying this global scaling method the uncertainty on m_{top} from the JES uncertainty is considerably reduced [99].

The variable $m_{\text{top}}^{\text{stab}}$ is calculated as the ratio of the reconstructed masses of the top-quark and the W-Boson candidates from the selected jet triplet. For convenience this ratio is multiplied by $M_{\text{W}}^{\text{PDG}}$. The main consequence of using $m_{\text{top}}^{\text{stab}}$ is a strong event-by-event cancellation of the JES dependence of the three-jet and two-jet masses in the mass ratio, while retaining the sensitivity to m_{top}. The quantitative gain in stability when using $m_{\text{top}}^{\text{stab}}$ instead of the jet triplet invariant mass $m_{\text{top}}^{\text{reco}}$ is apparent from Fig. 6.44 taken from [100] Using this variable a template analysis has been developed [96, 101, 100]. In this analysis Probability Density Functions (PDFs) are constructed from templates of the signal events at various assumed m_{top} values and from a template of the combined physics background events. The signal PDF linearly depends on m_{top}, whereas the background PDF does not. Using pseudo-experiments for a given luminosity the sensitivity of the method, together with the systematic uncertainties from various sources, has been estimated. An example of a pseudo experiment is shown in Fig. 6.45 for the muon channel and for $\sqrt{s} = 10\,\text{TeV}$ and $\mathcal{L}_{\text{int}} = 100\,\text{pb}^{-1}$. For this situation the statistical uncertainty for the combined electron and muon channel is about 2 GeV. The total systematic uncertainty is estimated to be about 3.8 GeV for each channel, still dominated by the systematic uncertainty from the JES for light jets and b-jets [100].

The determination of the combinatorial- and physics background from data rather than from Monte Carlo samples likely results in a reduced systematic uncertainty. For this purpose a data driven method was developed that explores the $m_{\text{top}}^{\text{reco}}$ and $R_{\text{top}} = m_{\text{top}}^{\text{reco}}/M_{\text{W}}^{\text{reco}}$ distributions at the same time. The idea

is to use e.g. the events from the sideband region of the $m_{\text{top}}^{\text{reco}}$ distribution to predict the shape of the background contribution to the R_{top} distribution. An initial investigation ignoring possible shape differences of the combinatorial- and physics background, and using a simple four-vector smearing approach, yields promising results, and will be extended to fully simulated Monte Carlo events and eventually data.

A direct fit to the $m_{\text{top}}^{\text{reco}}$ distribution and the template method lead to different systematic uncertainties. An analysis is underway to systematically compare the two approaches. This is done for the p_{T}-max and for a selection method that defines the top-quark as the jet triplet with the minimum sum of the three ΔR values.

Concerning the cross-section measurement an initial investigation of a cut and count analyses with and without using b-jet identification has been performed [102]. It exploits the lepton + jets channel at $\sqrt{s} = 10\,\text{TeV}$ and for $\mathcal{L}_{\text{int}} = 200\,\text{pb}^{-1}$. Within the systematic uncertainties investigated the total systematic uncertainty estimated is about 30%.

All-Jets Channel

In the all-jets channel only jet requirements and jet topologies can be used to separate the signal from the background reactions. Consequently, this channel suffers from a much higher background from the QCD multijet production. Here, events with isolated leptons are vetoed, and the missing transverse energy is required to be consistent with zero. In addition, at least six jets, not consistent with being purely electromagnetic, and two of which are identified b-jets, are required within $|\eta| < 2.5$. By exploring the transverse energies of the jets and the angular correlation of the two b-jets, the S/B is improved by several orders of magnitude to about 10^{-1}, while retaining a signal efficiency of about 10%. In this procedure the use of b-jet identification is absolutely essential. In addition, the availability of a multi-jet trigger with appropriate thresholds is imperative to not loose the signal events already at the trigger stage. This involves a delicate optimization to retain a sufficiently high efficiency for the signal events, while not saturating the ATLAS readout system with the QCD multijet events. The trigger conditions have been carefully studied, and the use of some trigger signals are suggested to ATLAS. Under the assumption that these will be available, and when exploiting the above event selection, a mass distribution has been isolated, where the signal starts to be visible on a still large background. For this analysis the next steps are the optimization of the background description and a fit to the distribution to access the sensitivity to m_{top}.

Summary

In summary the MPP analyses in the Top Physics area are well advanced. A variety of paths are explored in the search for the most appropriate variable and analysis strategy to determine the top-quark mass, a measurement that will soon be dominated by the systematic uncertainty. The methods in hand allow for a cross-calibration of the result for gaining confidence in their stability. Members of the group are actively participating in the ATLAS efforts, and have presented Top Physics results from the MPP group and beyond at international conferences [103, 104]

6.2.3 Searches for the Higgs Boson

The origin of particle masses is one of the most important open questions in particle physics. In the Standard Model (SM), the answer to this question is connected with the prediction of a new elementary particle with neutral charge, the Higgs boson H. The mass m_H of the Higgs boson is an unknown parameter of the theory. The experimental lower bound of 115 GeV has been set by the LEP experiments, while the recent searches at the Tevatron have excluded a SM Higgs boson in the mass range of $162 < m_H < 166$ GeV. The theoretical upper limit of about 800 GeV still leaves a wide mass range to be explored.

In the minimal supersymmetric extension of the Standard Model (MSSM), the Higgs mechanism predicts the existence of five Higgs bosons, three neutral ($h/H/A$) and two charged ones $H^{\pm}$. Their production cross-sections and decays are determined by two independent parameters, e.g. the ratio $\tan\beta$ of the vacuum expectation values of the two Higgs doublets in this model and the mass m_A of the pseudoscalar Higgs boson. Current experimental searches at LEP and Tevatron exclude at a 95% confidence level the A boson mass values below 93 GeV, as well as the $\tan\beta$ values below 2. For an A boson mass of up to 200 GeV, also the high $\tan\beta$ values above 40 are excluded.

The search for the Higgs boson is one of the main motivations for the LHC and the ATLAS experiment. The high cross sections of the background processes exceeding the signal by many orders of magnitude call for selective triggers, efficient background suppression and reliable prediction of the background con-

tributions. Until recently, our studies were devoted to the preparation for an early Higgs boson discovery during the first years of LHC running at the nominal center-of-mass collision energy of 14 TeV. The obtained results can be found in the newly published review of the ATLAS physics potential [105]. As of lately, the searches are being optimized for the initial LHC operation at a centerer-of-mass energy of 7 TeV. With a relatively low expected total integrated luminosity of 1 fb^{-1}, the Higgs boson discovery is rather unlikely under these operating conditions. However, the allowed Higgs mass range can be constrained beyond the present experimental limits, as summarized in [106].

The Standard Model Higgs Boson

The expected potential for the Standard Model Higgs boson discovery is shown in Fig. 6.46. In the mass

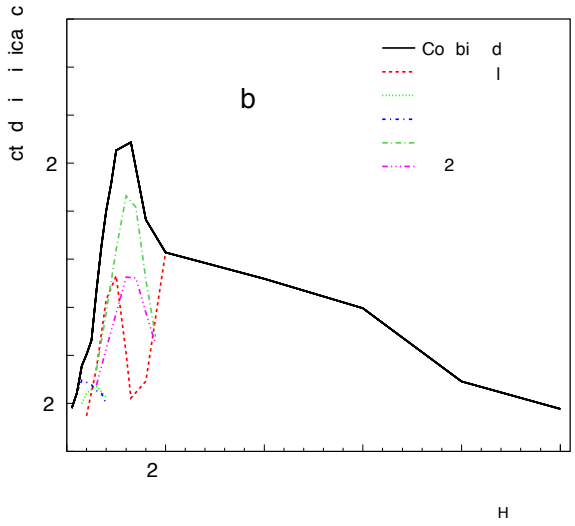

Figure 6.46: Discovery potential of the ATLAS experiment for the Standard Model Higgs boson. The statistical significance expected for an integrated luminosity of 10 fb^{-1} at a centerer of mass energy of 14 TeV is shown for the different Higgs decay modes and their combination as a function of the Higgs boson mass m_H.

range above 180 GeV, the key discovery channel is the Higgs decay into four charged leptons via two intermediate Z bosons. The lower mass range can only be covered by the combination of searches in several Higgs decay modes.

The clearest signature is found in the four-lepton decay channel $H \rightarrow ZZ^{(*)} \rightarrow 4\ell$ which also allows for a precise Higgs mass measurement. The reconstruction of this channel strongly relies on the high lepton identification efficiency and good momentum resolution of the ATLAS detector. The reducible $Zb\bar{b}$ and $t\bar{t}$ background processes can be suppressed by means of the Z boson mass reconstruction and the requirement of a low jet activity in the vicinity of each lepton. The remaining reducible background is small compared to the irreducible $ZZ^{(*)}$ background. In addition to the optimization of the analysis selection criteria, our studies include the detailed evaluation of the theoretical and experimental systematic uncertainties for both signal and background processes [107]. We also evaluate the potential to exclude a part of the allowed Higgs mass range in the initial phase of LHC operation [108], including the development of the methods for the precise determination of the background contributions from data. The expected exclusion limits are shown in Fig. 6.47 (top picture). The best upper limit on the Higgs boson production, obtained for the Higgs mass around 200 GeV, is still about a factor of two above the Standard Model prediction. The exclusion reach is especially low in the mass region around 160 GeV, where the $H \rightarrow ZZ^*$ decays are strongly suppressed by the Higgs boson decays into two on-shell W bosons.

Due to the high branching ratio for the decay $H \rightarrow W^+W^- \rightarrow (\ell\nu)(\ell\nu)$, the Higgs boson with a mass between 140 GeV and 180 GeV can be excluded in this channel during the initial phase of LHC operation. In combination with the four-lepton decay channel, the exclusion reach is slightly improved to cover the mass range from 135 GeV to 190 GeV, as shown in Fig. 6.47 (bottom picture). Due to the two neutrinos in the final state of the Higgs decays into W bosons, no precise measurement of the Higgs mass is possible. Precise determination of the background contributions is therefore required to exclude the presence of signal events. For this purpose, we are measuring the Standard Model background processes with present LHC data. The $H \rightarrow WW$ decay channel also allows for an early Higgs boson discovery during the LHC operation at 14 TeV. Parallel to the optimization of the event selection criteria in this context [109], we have developed a new algorithm for the jet reconstruction [110, 111], which is used for the suppression of the $t\bar{t}$ and $W + jets$ backgrounds to the Higgs production via the W or Z gauge boson fusion. The algorithm reconstructs the jets using particle tracks in the inner detector instead of energy deposition in the calorimeters. The inner detector tracks can be associated to

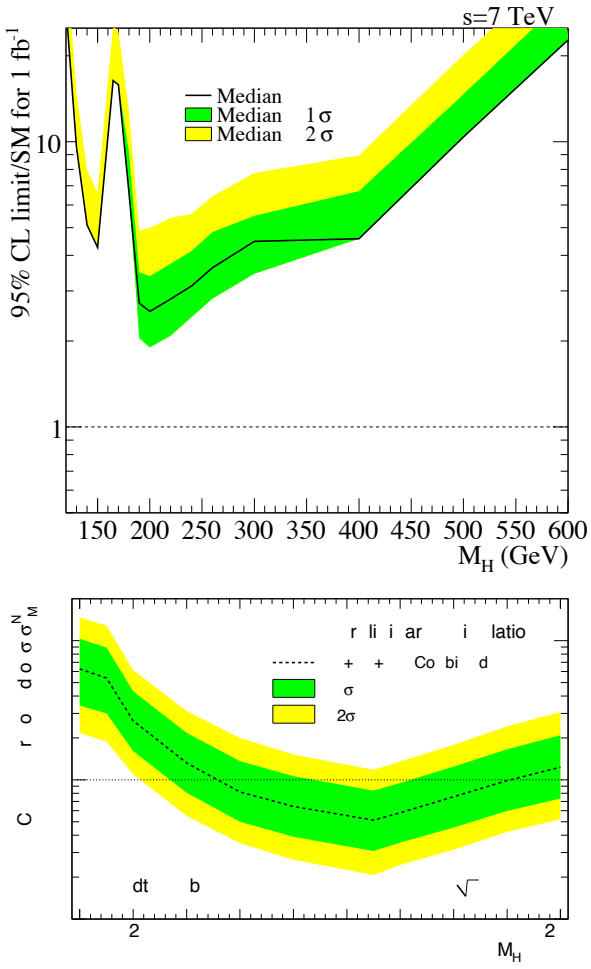

Figure 6.47: Expected upper limits (95% confidence level) on the Standard Model Higgs boson production rate in the $H \to ZZ^{(*)} \to 4\ell$ channel alone (top picture) and after the combination with the $H \to WW \to \ell\nu\ell\nu$ and $H \to \gamma\gamma$ channels (bottom picture), shown as a function of the Higgs mass at an integrated luminosity of 1 fb^{-1} and a centre-of-mass energy of 7 TeV and normalized to the Standard Model prediction. The bands indicate the 68% and 95% probability regions in which the limit is expected to fluctuate in the absence of signal.

common vertices leading to a jet reconstruction probability which is insensitive to the presence of multiple proton-proton interactions per beam collision (pile-up events).

In the mass range below 140 GeV, the Higgs boson predominantly decays into $b\bar{b}$ pairs. Due to the large contribution of QCD background in the gluon-fusion production mode, this decay can only be triggered and discriminated from the background in the production mode of the Higgs boson in association with a $t\bar{t}$ pair. Our studies have shown that the discovery potential in the $H \to b\bar{b}$ decay channel is very much limited by the large experimental systematic uncertainties [112, 113].

The second most frequent mode which can be observed in the mass range below 140 GeV is the decay into a $\tau^+\tau^-$ pair. This decay can only be discriminated against the background processes in the Higgs production mode via the W or Z gauge boson fusion where two additional forward jets in the final state provide a signature for background rejection. The decay modes with both τ leptons decaying leptonically ($\ell\ell$ mode) as well as with one hadronic and one leptonic τ-decay (ℓh mode) have been studied ([114], [115]). The event selection criteria have been optimized using multivariate analysis techniques. With a neural network based background rejection method, the signal significance is improved compared to the standard analysis with sequential cuts on the discriminating variables, as shown in Fig. 6.48.

Higgs Bosons Beyond the Standard Model (MSSM)

The searches for the three neutral Higgs bosons predicted by the MSSM differ to some extent from the searches for the SM Higgs particle. The neutral Higgs decay modes into two intermediate gauge bosons are suppressed in MSSM, while the A and H boson decays into charged lepton pairs, $\mu^+\mu^-$ and $\tau^+\tau^-$ are enhanced compared to the Standard Model. The later decay channel has an about three hundred times higher branching ratio compared to the first one but is more difficult to reconstruct and provides a less precise Higgs mass determination.

Our studies of MSSM Higgs decays into two τ leptons are summarized in [116]. The dominant background contribution originates from the $Z \to \tau^+\tau^-$ and $t\bar{t}$ processes and can be suppressed by the requirements on the b quark jet reconstruction and large angular separation between the two decaying leptons. This channel provides the highest sensitivity reach for the neutral MSSM Higgs bosons.

Motivated by the excellent muon reconstruction in the ATLAS detector, we also study the prospects for the search in the channel with MSSM Higgs boson decays into two oppositely charged muons. The event selection criteria are optimized for the best discovery potential taknig into account the theoretical and experimental systematic uncertainties [117]. The invariant dimuon mass distribution after all analysis selection criteria is shown for the signal and dominant background processes in Fig. 6.49. The dominant $Z \to \mu^+\mu^-$ and $t\bar{t}$ background contributions are rather large

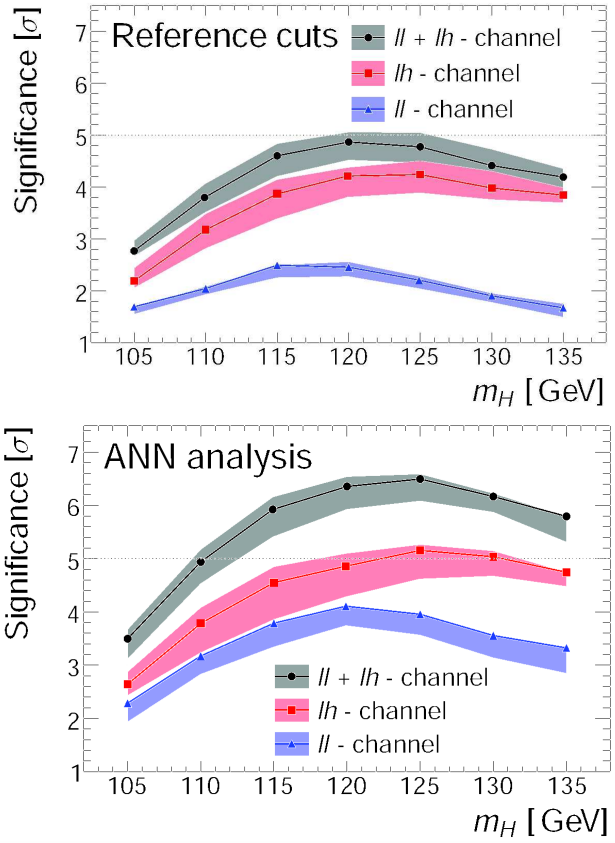

Figure 6.48: Discovery potential for the Higgs boson search in the $H \to \tau^+\tau^-$ decay channel, shown separately for the fully leptonic $\tau^+\tau^-$ decay mode ($\ell\ell$), semi-leptonic mode (ℓh) and their combination at an integrated luminosity of 30 fb^{-1} and a center-of-mass energy of 14 TeV. The results are obtained using the standard analysis with sequential cuts on the discriminating variables (top picture), as well as for neural network based analysis (bottom picture). The shaded bands indicate the effect of the experimental systematic uncertainties.

compared to the signal and are subject to sizeable experimental systematic uncertainties, particularly with regard to the jet energy scale. It is therefore important to measure this background contribution with data. This can be done by combining the information from the side-bands of the invariant dimuon mass distribution with the measurements on the e^+e^- control sample. The later is motivated by an almost vanishing Higgs boson decay probability into two electrons, while the background contributions are similar for the dimuon and the dielectron final states. The expected ratio of invariant dielectron and dimuon mass distributions is shown in Fig. 6.50 after all analysis selection criteria and after correcting for the different electron and muon reconstruction and identification efficiency.

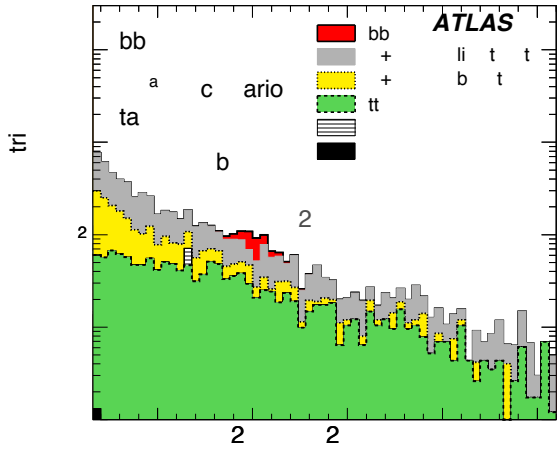

Figure 6.49: Invariant dimuon mass distributions of the main backgrounds and the A boson signal at masses M_A = 150, 200 and 300 GeV and tan β = 30, obtained for the integrated luminosity of 30 fb^{-1} at a center-of-mass energy of 14 TeV. Only events with at least one reconstructed b quark jet in the final state are selected.

We perform a detailed study of the background estima-

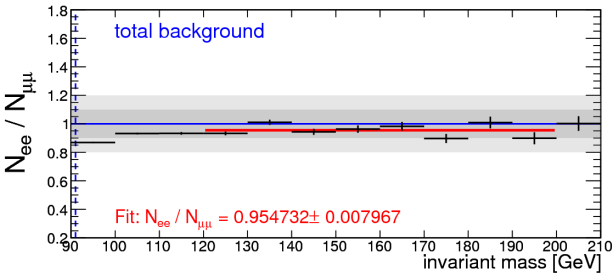

Figure 6.50: Ratio of the dilepton invariant mass distributions for the e^+e^- control sample and the total $\mu^+\mu^-$ background for the Higgs search in the $h/A/H \to \mu^+\mu^-$ channel, shown for an integrated luminosity of 4 fb^{-1} .

tion from data in [118, 119]. The presented method allows for a significant decrease of systematic uncertainties and thus in the imroved sensitivity reach for the MSSM Higgs boson search in the $\mu^+\mu^-$ decay channel. Especially during the initial phase of LHC running with the limited amount of data, the introduced control data samples are essential for obtaining reliable exclusion limits. The exclusion reach with early data at a center-of-mass collision energy of 7 TeV has been evaluated for the $h/H/A \to \mu^+\mu^-$ channel in [120], see Fig. 6.51. At an integrated luminosity of 1 fb^{-1} one cannot improve the current limits reached

by the Tevatron experiments using this channel alone. However, its combination with searches in a more sensitive $h/H/A \rightarrow \tau^+\tau^-$ decay channel allows for an improved coverage of the $(m_A, \tan\beta)$ parameter space.

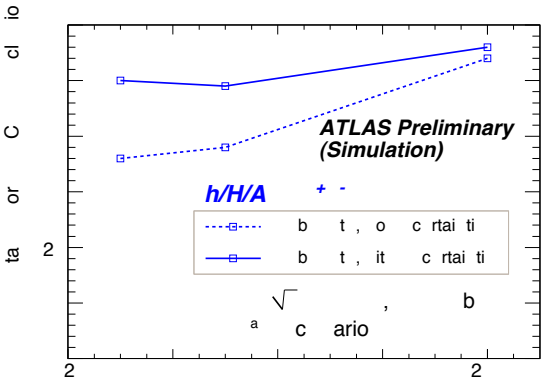

Figure 6.51: The $\tan\beta$ values needed for an exclusion of the neutral MSSM Higgs bosons shown as a function of the Higgs boson mass m_A for the analysis mode with at least one b-jet in the final state. An integrated luminosity of 1 fb^{-1} and a center-of-mass energy of 7 TeV are assumed. Dashed lines represent the results assuming zero uncertainty on the signal and background, while the full lines correspond to the results with both signal and background uncertainty taken into account.

The light neutral MSSM Higgs boson is difficult to distinguish from the Standard Model Higgs boson. Clear evidence for physics beyond the Standard Model would be provided by the discovery of charged scalar Higgs bosons. We have studied the prospects for the search for the charged MSSM Higgs bosons in the decay channel $H^\pm \rightarrow \tau^\pm\nu_\tau$ which dominates for relatively small Higgs masses below 200 GeV [121, 122]. The charged Higgs bosons are produced in top quark decays in $pp \rightarrow t\bar{t} \rightarrow (bH^\pm)(bW^\mp)$ events. The τ leptons from $H^\pm$ decays are reconstructed in their hadronic decay modes while the W bosons from top quark decays are required to decay leptonically. Since $H^\pm$ mass cannot be reconstructed because of the undetected neutrinos in the final state, these events can only be distinguished as an excess of events with reconstructed τ leptons and large missing transverse energy above the high background of standard model decays of top quark pairs.In Fig. 6.52, the discovery region in the $(m_H^\pm, \tan\beta)$ plane is shown for a charged Higgs boson in the above production and decay mode assuming different amounts of integrated luminosity. The theoretical and experimental systematic uncertainties have

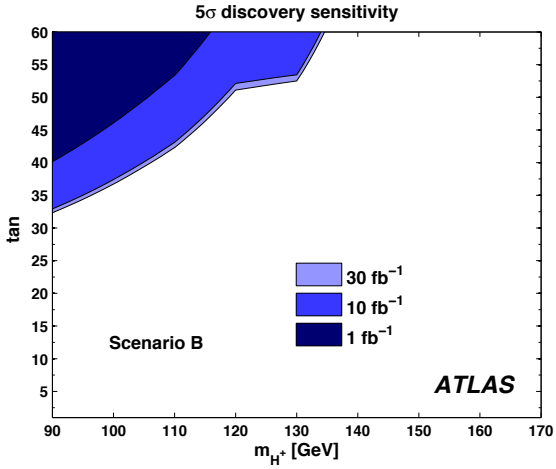

Figure 6.52: The $\tan\beta$ values needed for a discovery of the charged MSSM Higgs bosons shown as a function of the Higgs boson mass $m_{H^\pm}$ for different levels of integrated luminosity. A center-of-mass energy of 14 TeV is assumed. The decays $H^\pm \rightarrow \tau^\pm\nu_\tau$ can be discovered with at least 5σ significance in all shaded regions of the parameter space.

been taken into account. We have developed the methods to decrease the original instrumental backgound uncertainty of 50% down to 10% by means of the control measurements on data [122, 123].

6.2.4 Search for Physics Beyond the Standard Model

Supersymmetric Particles

Supersymmetry (SUSY) is the theoretically favoured model for physics beyond the Standard Model. The new symmetry uniting fermions and bosons predicts for each Standard Model particle a new supersymmetric partner with spin quantum number differing by $1/2$. Supersymmetry provides a natural explanation for Higgs boson masses near the electroweak scale. In addition, the lightest stable supersymmetric particle is a good candidate for dark matter. Another theoretical problems which can be solved by SUSY is the unification of the fundamental forces.

If the mass scale of the SUSY particles is accessible at LHC, the squarks and gluinos (the superpartners of quarks and gluons with spin 0 and $1/2$, respectively) will be copiously produced in pp collisions. In order to suppress the processes violating the barionic and leptonic quantum numbers, R-parity is introduced. The consequences of R-parity are that supersymmetric particles must be produced in pairs and each will decay to weakly interacting lightest supersymmetric particle via decay chains involving production of quarks and

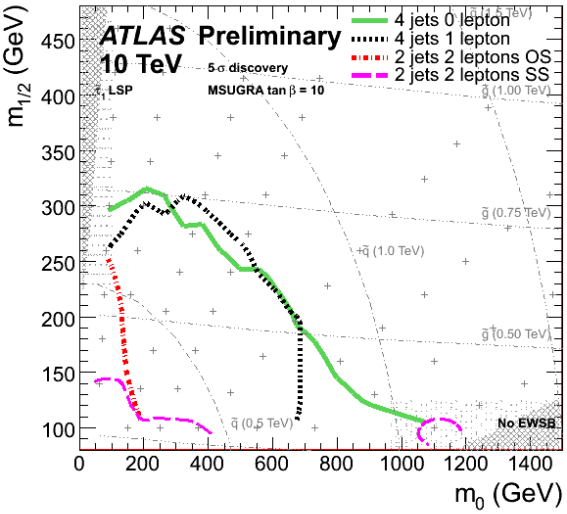

Figure 6.53: ATLAS 5-σ discovery reach for the the mSUGRA model for the channels with various jet and lepton multiplicity in the parameter space of mSUGRA model defined by common mass of fermion $m_{1/2}$ and common mass of bosons m_0 at the GUT scale. The discovery reach is estimated for the center-of-mass energy is 10 GeV and the integrated luminosity is 200 pb^{-1}.

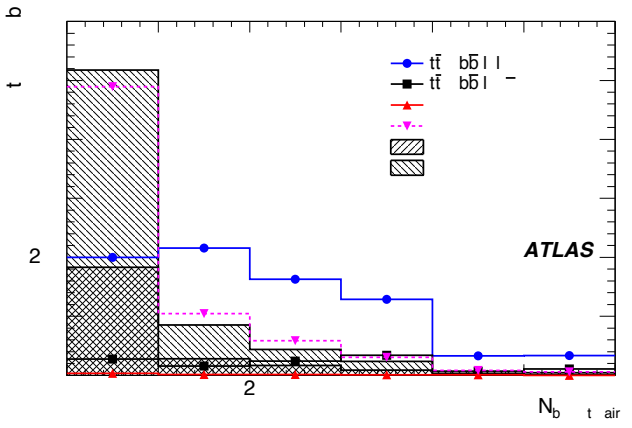

Figure 6.54: Number of b-jet pairs $N_{b-jetpairs}$ passing the kinematic requirements of $t\bar{t}$ process with both t-quarks decayed to b-quark, neutrino and lepton (electron or muon). The $N_{b-jetpairs} > 0$ region is mainly populated by $t\bar{t}$. This region is used as a "control sample" for the estimations of $t\bar{t}$ background with τ-lepton and non-identified electrons and muons in SUSY searches with one lepton. The bin $N_{b-jetpairs} = 0$ is filled by the gauge boson production processes and by the SUSY events simulated by two typical models labeled SU1 and SU3.

leptons. Therefore, the SUSY events at LHC are characterized by the large transverse missing energy, high energetic hadronic jets and leptons.

Supersymmetry requires equal mass for the particle and its superpartner. As the supersymmetric partners of Standard Model particles are not observed so far, SUSY must be a broken symmetry. A model with SUSY breaking mediated by gravitational interaction is called mSUGRA and is described by the common boson mass and common fermion mass at energy scale above 10^{15} GeV, where the electroweak and strong interactions are unified (GUT scale).

The searches for SUSY signatures with R-parity conservation in ATLAS are performed by searching an excess of events in various channels. These channels explore a large variety of possible signals, e.g. different jet and lepton multiplicities. Fig. 6.53 shows 5-σ discovery reach for the mSUGRA model for the 4 jet 0 lepton, the 4 jet 1 lepton and the 2 jet 2 lepton channels in the parameter space of mSUGRA model defined by common mass of fermion $m_{1/2}$ and common mass of bosons m_0 at the GUT scale.

The Standard Model processes with similar signature are top quarks ($t\bar{t}$) and gauge bosons (W and Z) production. In these processes the large transverse missing energy is originated from weakly interacting neutrino. These processes constitute the main background to SUSY searches at LHC. Jet production from QCD process with "fake" transverse missing energy originated from jet energy mis-measurement is another important source of the background. It is expected that at LHC the Monte Carlo prediction will not be sufficient to achieve the good understanding and the control of the background to SUSY searches. Our studies are concentrated on the data-driven estimation of the backgrounds to SUSY searches, which is a key point of early discovery of SUSY by ATLAS detector.

With Monte Carlo simulations we have studied methods for determining the $t\bar{t}$ background from data [124]. The background estimation is performed by selecting the SUSY-free "control sample" from which the prediction of background is derived. The $t\bar{t}$ production with top quark decays involving the τ leptons and non-reconstructed electrons or muons is estimated from similar events with identified muons and electron. The "control sample" composed mainly by events where both top quarks decayed to b-quark, neutrino and lepton (electron or muon) is selected by applying the set of kinematic constrains particular to this process. The resulting variable, denoting the number of b-jet pairs passing the kinematic constrains is used to separate the signal region into SUSY-dominated region and $t\bar{t}$-dominated region.

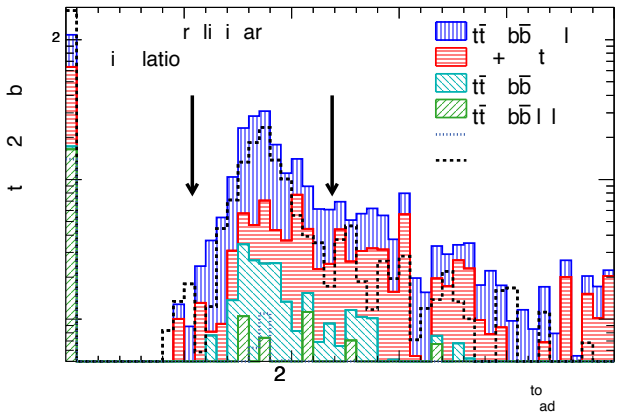

Figure 6.55: Distribution of invariant mass of tree nearby jets. This variable used for the selection of the "control sample" of $t\bar{t}$ events with one top quark decayed to jet, neutrino and lepton (electron or muon), and the other top quark decayed to b-quark and two light quarks. This "control sample" is used to derive the data-driven production of $t\bar{t}$ background in SUSY searches with no-lepton signatures. The arrows show the chosen window for this variable. The Standard Model contributions are shown by the stacked hatched histograms. The SUSY contribution for two typical SUSY mSUGRA models labeled as SU3 and SU4 are overlaid.

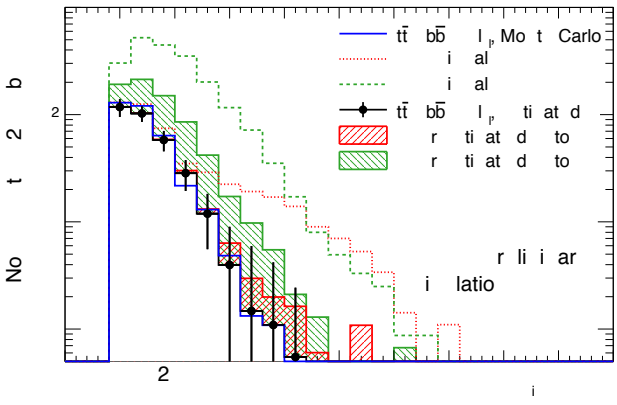

Figure 6.56: Distribution of transverse missing energy in $t\bar{t}$ events. The solid line shows the Monte Carlo estimate, circles show the result of data-driven estimation. The shaded histograms show the increase of data-driven estimates in the presence of SUSY signal (represented by SU3 and SU4 models) in the "control sample" and the dashed lines shows the SUSY signals stacked on the top of $t\bar{t}$ background.

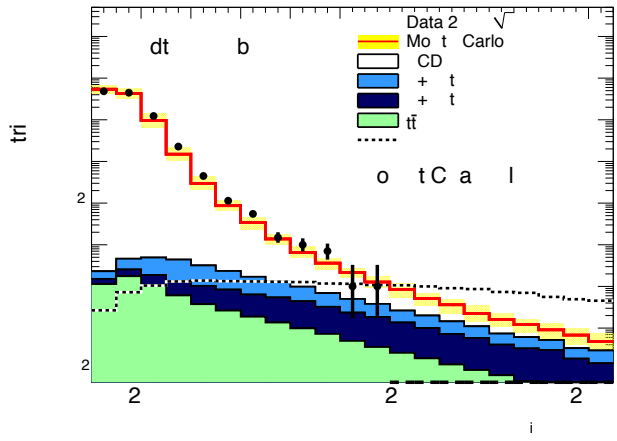

Figure 6.57: Distribution of missing transverse energy for events with two jets. Black points shows the first 70 nb^{-1} of data collected by ATLAS experiment during the period March-July 2010. Shaded histograms shows the contribution of gauge boson and top quark production processes. The open red histogram shows the QCD di-jet production process. The prediction of low-mass mSUGRA model SU4 (enhanced by factor 10) is shown by black dashed line.

Similar strategy is used for isolation of the control sample with $t\bar{t}$ events with one top quark decayed to jet, neutrino and lepton (electron or muon), and the other top quark decayed to b-quark and two light quarks [125]. In this case the discriminating variable is the invariant mass of three close hadron jets, which is close to mass of the top quark for $t\bar{t}$ events.

The $t\bar{t}$ events with tau leptons produced in top-quark decay are reproduced by the events of the "control sample" by replacing the electron or muon with a tau lepton and simulating the tau lepton decay. Similar, the contribution with non-identified electron or muon is reproduced by treating the lepton as if it had not been identified.

We analyzed a set of the most important kinematic variables for the first 70 nb^{-1} of data collected by ATLAS experiment during the period March-July 2010 [126]. We find good agreement between data and Monte Carlo simulation indicating that the Standard Model backgrounds to SUSY searches is under good control.

Other Extensions of the Standard Model

Since the discovery of the neutrino flavour oscillations it is known that the lepton flavour is not conserved in particle interactions. One of the lepton flavour violating process accessible at LHC is a neutrinoless decay of a tau lepton $\tau \to \mu\mu\mu$. Although the Standard Model predicts very small branching ratio for this decay,

$$B(\tau \to \mu\mu\mu) \leqslant 10^{-14},$$

some extensions of the Standard Model, such as SUSY and models with double charged Higgs Boson, pre-

dicts sizable value for it. Therefore, the measurement of branching ratio of $\tau \to \mu\mu\mu$ will put stringent limits on the parameters of these models.

During one year of data-taking at the low luminosity phase ATLAS will collect 10^{12} τ lepton decays. Due to severe background only fraction of these decays can be observed in ATLAS, namely decays of τ lepton produced via W and Z bosons. We studied the sensitivity of the ATLAS detector to the $\tau \to \mu\mu\mu$ decay, where the tau lepton is produced by decay of W boson [127]. This process is characterized by large transverse missing energy produced by non-detectable neutrino, and by three nearby muon tracks. The main background processes are production of charmed and beauty mesons, with following decay to muons.

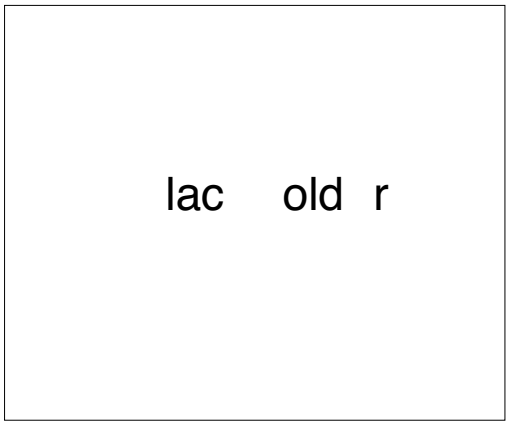

Figure 6.58: Invariant mass distribution of tree nearby muons produced by $\tau \to \mu\mu\mu$ decay with tau lepton produced via W boson (green) and by the background processed, including decay of charmed and beauty mesons. All selection cuts except of the cut on the shown variable are applied to the Monte Carlo data, normalised to the integrated luminosity of 10 fb^{-1}. Non-shaded area shows the cut on the invariant mass of tree muons.

The study with the simulated data shows that the upper limit of $B(\tau \to \mu\mu\mu) \leqslant 5.9^{-7}$ can be achieved with 10 fb^{-1} of collected data. With the expected sensitivity, an integrated luminosity of 100 fb^{-1} has to be collected by ATLAS experiment to reach the current best upper limit of $B(\tau \to \mu\mu\mu) \leqslant 3.2^{-8}$ (90% CL) of the BELLE experiment.

In addition, we pursue searches for non-Standard Model heavy neutral gauge boson Z' predicted by some extensions of Standard Model which address the problems of mass hierarchy and number of generations of lepton and quarks.

6.3 Detector Upgrade

The design luminosity of the LHC of $10^{34}\,\mathrm{cm}^{-2}\mathrm{s}^{-1}$ is expected to be reached after a few years of data taking at lower luminosity. In an experimental run at the LHC the design luminosity will only be available at the beginning of a machine fill, then it decays slowly due to proton losses and beam size increase. When the luminosity has decreased to about half the initial value after typically 5 hours, the beams will be dumped and a new proton fill will be accumulated. The *integrated* luminosity after 10 years of operation under these conditions is expected to be about 300 fb^{-1}.

For the study of even lower-cross section phenomena at the LHC, a substantial increase of the LHC luminosity is needed. With a series of upgrades of the CERN accelerator complex an order of magnitude could be achieved, which may yield an integrated luminosity of up to 3000 fb^{-1} after 10 years of additional running (Super-LHC or SLHC). To help the LHC detectors to cope with this luminosity increase, a new operation mode of the machine is foreseen ("luminosity levelling"), reducing the decay rate of luminosity during a proton fill in such a way that the peak luminosity at the beginning of the fill will be limited to about $4 \times 10^{34}\,\mathrm{cm}^{-2}\mathrm{s}^{-1}$, yet yielding a 10 times higher integrated luminosity for the fill.

While this reduction of the *peak* relative to the *integrated* luminosity by a factor of 2.5 represents a substantial alleviation for the operation of the ATLAS detector, the increase of luminosity by a factor of 4 relative to the original design value of $10^{34}\,\mathrm{cm}^{-2}\mathrm{s}^{-1}$ still calls for a major upgrade effort for most subsystems of the ATLAS detector. Tracking detectors, for example, may need higher granularity to cope with the high particle rates while e.g. the overall radiation dose corresponding to 3000 fb^{-1} will require new radiation hard readout electronics in all subsystems of the ATLAS detector.

6.3.1 R&D towards a novel Pixel Detector for the SLHC

Overview

The present ATLAS Inner Detector consists of a pixel detector, the SCT detector, and the TRT, which are located at increasing radii from the beam line as described above.

After about five years of operation it is planned to extend the present pixel detector by an additional innermost layer, which will be directly mounted onto a

new beam pipe. This upgrade is named the Insertable B-Layer (IBL). After ten years of operation at the LHC with the design luminosity profile the complete silicon part of the ATLAS Inner Detector has to be replaced due to radiation damage. In addition, an upgrade of the LHC accelerator, named Super-LHC (SLHC), is planned to reach a ten-fold increase in luminosity. Consequently, for a given radius the expected the radiation dose and hit occupancy at the SLHC are a factor 5–10 higher than at the LHC. The Inner Detector upgrade, mandatory for running at the SLHC, demands a completely new design for the Inner Detector, rather than upgrading the existing detector. For example, the high hit occupancy leads to an unacceptable occupancy for the TRT detector, which needs to be replaced by a new device with a different detector technology. The choice has been made for a patterned solid state detector with decreasing granularity for increasing radius. Although the general strategy is clear, the details of the layout and also the detector concepts to be used at various radii are still under study.

The geometrical design is developed by the Inner Detector Layout Group, where the MPP is participating. The initial design, the strawman, has been defined in [128]. From this the final design will be obtained by iteration, depending on the results from detector R&D as well as simulation of the expected performance. In any case, the expected increase in radiation dose means that a new generation of radiation tolerant silicon sensors has to be developed for the innermost part of the Inner Detector.

MPP Module Design

Utilizing the knowledge and capabilities of the semiconductor laboratory, HLL, who designed both the present pixel and the SCT sensors, the MPP has set out to investigate the feasibility of a novel detector concept for the pixel detector. The R&D [129] is embedded in the ATLAS upgrade activities, and has three main ingredients, 1) the production of (75–150)μm thin sensors to increase the radiation tolerance, 2) the use of a novel interconnection technology (SLID, see below) for attaching the readout electronics to the pixel sensors that may lead to a cost effective solution to replace the presently used bump bonding technology, and 3) the vertical integration of analog and digital electronics with inter chip via (ICV), which will allow for individual optimization of the electronic chips. A sketch of a pixel module using this concept, while obeying the restrictions placed by the presently available ATLAS FEI3 read-out electronics, is shown in Fig. 6.59.

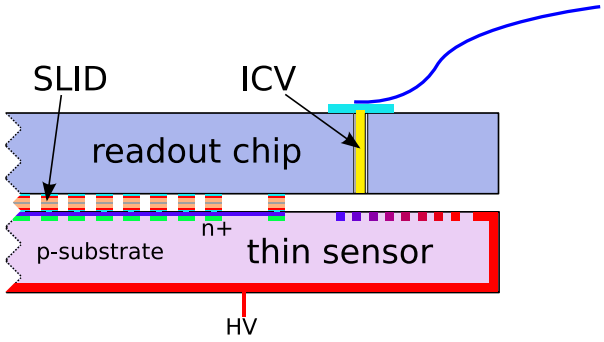

Figure 6.59: Sketch of the MPP module concept.

For the production of thin sensors the process [130] developed at the HLL is used. These sensors offer beneficial features [131] like a low depletion voltage, low leakage current and high charge collection efficiency (CCE).

The novel Solid-Liquid InterDiffusion (SLID) interconnection technology [132] has been developed by the Fraunhofer IZM Institut in Munich [133], but was not yet applied to sensors made for high energy experiments. The high density interconnection technology allows for smaller pixel sizes than in the current ATLAS hybrid pixel detector, which may be hard to achieve by the presently used bump bonding technique. Besides the interconnection of chips and sensors this technology allows for vertical integration of several layers of thinned chips with ICVs, by using the combined ICV-SLID process. When exploiting this, e.g. the chips performing the analog and digital parts of the read-out can be arranged on top of each other rather than side by side, which makes the design more compact and the signal paths shorter. In addition, the chips can be made using different technologies and optimized individually in terms of speed, power consumption and radiation hardness, allowing for a better overall performance. The first investigations, like the initial design studies and the compatibility investigations of thin sensors with the SLID metalization system and processing steps [134], were already reported in [9]. The results obtained in the years 2007-2010 are described below, starting with the sensor design supported by device simulation, followed by the wafer production and device evaluation, and finally the SLID and ICV investigations.

Thin Sensors

The design and production of four thin sensor wafers in n^+-in-n and eight in n^+-in-p technology, containing a variety of different structures, has been performed. For the n^+-in-n technology all four wafers have 75 μm thin active sensors, whereas for the n^+-in-p technology four wafers each have 150 μm and 75 μm thin active sensors. These wafers were partly processed at the HLL and partly at industrial companies.

The most important structures are firstly strip sensors for CCE measurements, and secondly pixel devices with the ATLAS pixel sensor geometry used to either be connected to the present ATLAS pixel chips, and read-out by the existing data acquisition system to study system issues, or to investigate the ICV-SLID technologies. To determine the implant parameters, and to better understand the behavior of the pixels before and after irradiation as functions of the parameters of the p-spray isolation, a simulation of a restricted part of the pixel array has been set up [135] using the DIOS/TeSCA silicon device simulation software.

The wafer production was very successful in terms of device yield and properties of the diodes, strips and pixel structures before and after irradiation with 26 MeV protons at the Karlsuhe Cyclotron up to fluences of 10^{16} n_{eq}/cm^2 (1 MeV neutron equivalent) expected at the SLHC. Some results of the wafers

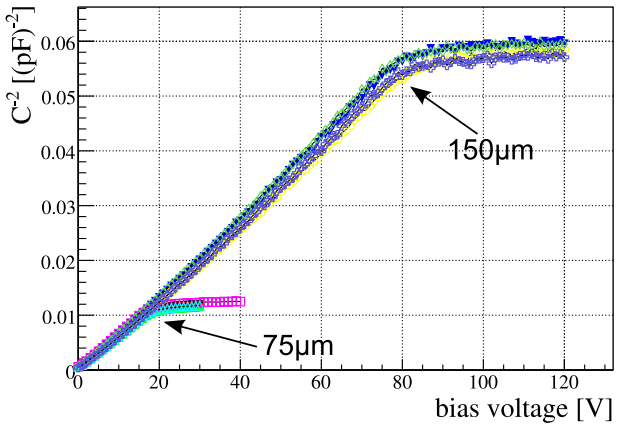

Figure 6.60: Capacitance-voltage characteristics of n^+-in-p diodes before irradiation.

made using the favored n^+-in-p option are reported below. The depletion voltage, which is indicated by the kink in the inverse capacitance squared versus voltage behavior shown in Fig. 6.60 for the non-irradiated diodes, is according to the expectation from the resistivity of the silicon material used. The measured values of about 20 V and 80 V also nicely exhibit the predicted quadratic scaling with the sensor thickness. The device yield for the FEI3 compatible pixel structures is 79 working structures out of 80 produced. This yield is defined by the current voltage characteristics and requiring that the sensor can be biased well above its depletion voltage. This is shown for a subset of 16 sensors in Fig. 6.61, and the one structure marked as failing is displayed with red circles drawing much more current than all the others with a steeply rising behavior at around 150 V. The overall level of leakage current in the plateau of about 5 nA/cm^2 is very low signaling a very high quality and low impurity processing of the wafers. After irradiation with protons

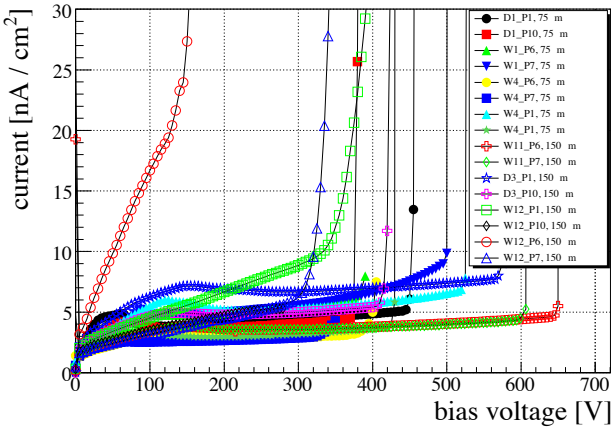

Figure 6.61: Current-voltage characteristics of n^+-in-p FEI3 pixel sensors before irradiation.

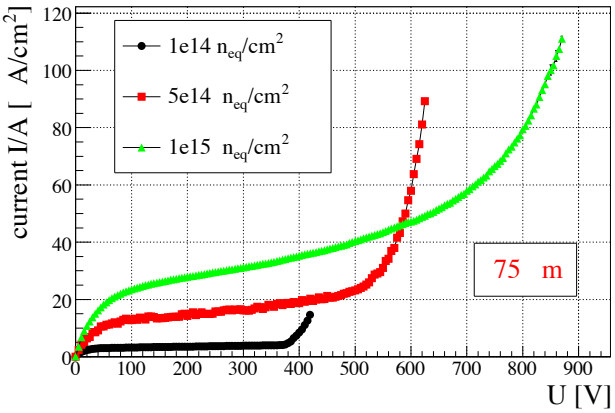

Figure 6.62: Current-voltage characteristics of n^+-in-p FEI3 pixel sensors after irradiation to three fluences.

up to various fluences the devices show the expected behavior, namely an increased current accompanied by a higher depletion voltage but also a much increased breakdown voltage. This is demonstrated in Fig. 6.62 for pixel sensors with 75 μm active thickness.

A very important, and at present also much debated, property of the sensors is the CCE, which is defined as the collected charge after irradiation normalized to the one obtained before irradiation. The conventional description of the radiation damage of silicon predicts very low CCE after large fluences. This leads to small signals at increasing noise rendering operation of the device more and more challenging due to a decreasing signal-to-noise (S/N) ratio. The decrease of the collected charge is caused mainly by radiation-induced bulk defects acting as traps for the electrons and holes, produced by the primary particle, on their drift path to the electrodes. As a result it is predicted that only charges from the close vicinity of the electrodes can arrive in time and lead to a detectable signal. Experimental observations from various groups are in clear contradiction to the prediction of a strongly reduced CCE, and rather show that for short collection distances, i.e. thin sensors or 3D sensors [1], the CCE after strong irradiation reaches unity or even surpasses it. One model to account for this is charge multiplication, which occurs in very high electric fields, and naturally is more likely for thin sensors, since here the bias voltage drops over a shorter distance.

The MPP group investigated this effect experimentally on n^+-in-p strip sensors, and also by a Monte Carlo simulation propagating the electrons through the detailed electric field of the devices while simulating charge trapping, but also the charge multiplication process, both according to existing models.

The measured CCE as a function of the bias voltage for various sensors and fluences is shown in Fig. 6.63. Clearly sensors of both thicknesses largely surpass the prediction from conventional trapping models (see below), and for the 75 μm thin devices the full charge can be recovered within uncertainties, albeit at increasing voltages for increasing fluences. This is a very important result since it means that the requirements on the minimum signal charge for the newly designed FE-I4 readout chip, to be used for the IBL and for outer layers of the pixel detector for the SLHC, is less demanding than initially thought. However, only the experimental investigation of the module assemblies to be performed later this year will tell whether the S/N value will be high enough after strong irradiation.

[1] In 3D sensors the electrodes are not implanted on the surface as for planar sensors, but as columns through the bulk of the sensor. This enables to achieve short collection distances independent of the bulk thickness, at the expense of the need to use a non-standard expensive production process, which at present has only low yield.

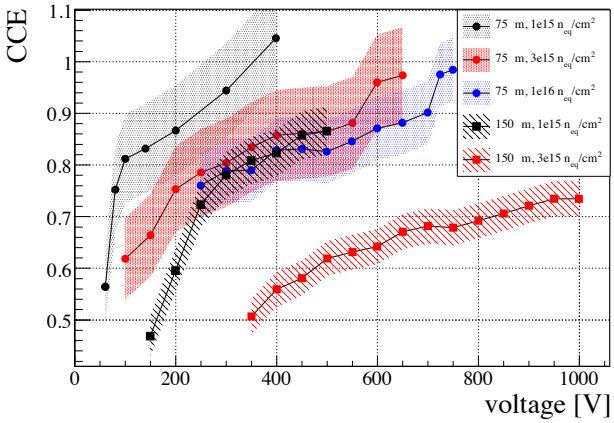

Figure 6.63: Charge collection efficiency of n^+-in-p strip sensors after irradiation.

The strip sensors used for the CCE measurements shown in Fig. 6.63 are DC coupled to the readout electronics. After irradiation this causes high currents to flow through the readout channels that prevent applying higher bias voltages than the ones shown to not damage the electronics. In future this limitation will be avoided by an AC coupling of the strips. At present for some of the sensors the use of decoupling pitch adapters between the sensor and the chip effectively leads to an AC coupling. With these measures higher bias voltages can be applied to investigate, whether also for the 150 μm thin sensors after irradiation, the full charge can be recovered at even higher voltages.

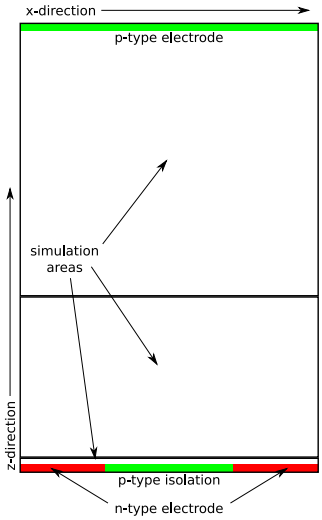

Figure 6.64: Sketch of the 2-dimensional area used for the device simulation.

The simulation of the predicted CCE is done two-dimensional, as shown in Fig. 6.64. In the MC simulation the electrons produced by an incident parti-

cle are individually followed through the sensor, and at each step charge trapping and charge multiplication are simulated based on the models available from the literature, and according to the electric field as calculated by the preceding DIOS/Tesca simulation described above [135]. Indeed, at high bias voltage and after large fluences, the electric field exceeds the value needed for charge multiplication, especially so at the boundaries of the p-type and n-type doping in the close vicinity of the collecting electrodes, i.e. the boundaries between the red and green regions close to $z = 0$ in Fig. 6.64. The predicted CCE for 75 μm thin diodes

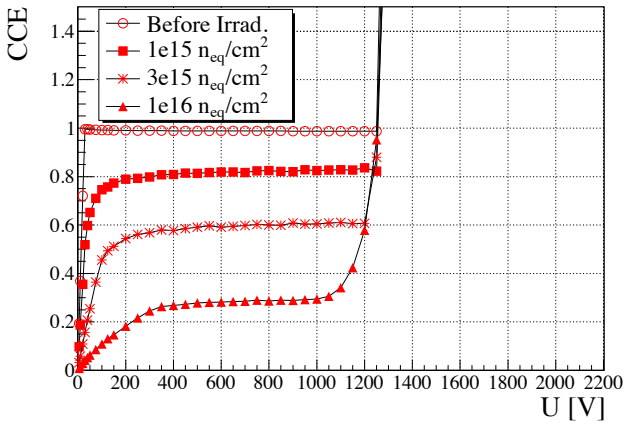

Figure 6.65: Predicted CCE for 75 μm thin n$^+$-in-p diodes after irradiation.

presented in Fig. 6.65 reveals a strong rise in CCE for fluences from $3 \cdot 10^{15}$ n_{eq}/cm^2, however at very high bias voltages well in excess of 1 kV. When comparing this prediction to the experimental result two facts are evident. The measured CCE in the plateau region is much higher than the prediction, e.g. for the 75 μm thin diodes at $1 \cdot 10^{16}$ n_{eq}/cm^2 and at 500 V the measurement is about 0.8 with a prediction of slightly below 0.3. The observed increase of the CCE with the bias voltage is roughly linear, and the predicted steep increase due to charge multiplication is not observed. Further investigations are clearly needed before proper predictions for the experimental observations can be made.

For the IBL upgrade a reduction of the inactive region around the active pixel region from the present width of about 1000 μm to about 450 μm is required. To achieve this, sensors with a so called slim-edge design with 11 instead of 21 guard rings around the active region have been produced. The high voltage behavior of the bare sensors with the slim edge design before and after irradiation is not significantly worse than that of the ones with the present guard ring design, proving that this requirement can be met.

In parallel to the MPP&HLL wafer production, n$^+$-in-p pixel sensors of the very same design have been produced at CiS and bump bonded to FEI3 electronics. Initial tests of these single chip modules are promising, showing adequate noise and sufficient high voltage stability. After irradiation to large fluences they will serve to verify that the passivation layer on top of the sensor is sufficiently insulating. This is needed to avoid sparking between the chip and the sensor which, in the n$^+$-in-p sensor technology, are only a few μm apart, but are kept at a potential difference of several hundred Volt.

Interconnection and vertical Integration

The SLID interconnection and ICV have been investigated in collaboration with the IZM Munich. A number of wafers containing inactive structures consisting of many long chains of aluminum traces, so called daisy-chains, to be individually connected via SLID have been designed and produced at MPP&HLL. The wafer layout is divided into two halves, one serving the sensor structures, the other half mimicking the chips to be connected to the sensors. These wafers were connected partly in a wafer-to-wafer approach, i.e. one wafer was rotated by 180 degrees and SLID connected to another wafer, and partly in a chip-to-wafer approach, i.e. the chips of one wafer were singularized, individually attached to a handle wafer, and this handle wafer was SLID connected to the sensor wafer. The results shown below are from the wafer-to-wafer connection. The chip-to-wafer approach yielded worse results due to technical problems that have led to an insufficient alignment of the chips on the handle wafer, and consequently a large number of non successful connections. The likely cause of this has been understood, and will be addressed for the next SLID connection run which is underway. The daisy-chains feature different sizes and pitches of SLID connections. Resistance measurements on these chains indicate if at least one connection of a chain is missing. By assuming a binomial probability distribution the SLID inefficiency is calculated from those resistance measurements. It is found to be of the order of one per mill for types where at least one connection was failing, and to be below three per mill for those where all chains were fully intact. Small deliberate vertical steps in the SLID connection, produced by omitting some layers in the structure design, and amounting to at most 1 μm, did not deteriorate these results. From

the fully working chains the resistance per connection was determined to be below 1.5 Ω and likely dominated by the contact resistance. These values are small enough for SLID to be used for connecting individual pixel cells.

In addition to the chains, these wafers contain geometrical structures that allow for the measurement of the positioning accuracy again by performing resistance measurements. The positioning accuracy of the SLID connections can also be deduced from infrared images of connected packages, see Fig. 6.66. The silicon bulk (grey area) is transparent to the infrared light, but the SLID metal layers (dark structures) are not. Consequently, these structures are visible both on the

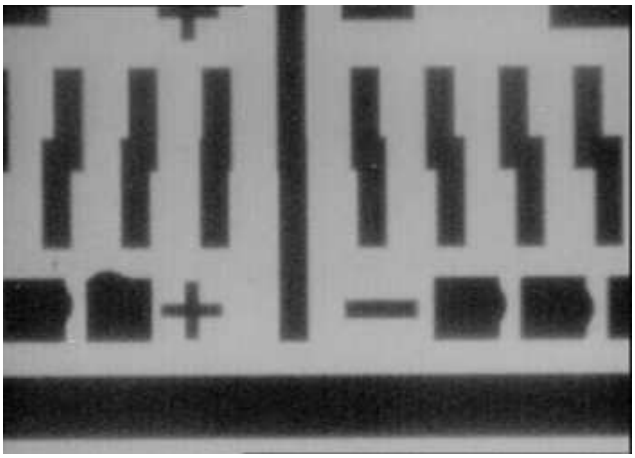

Figure 6.66: Infrared image of SLID connections.

sensor and on the chip surface. Comparing their position and overlap with the wafer design reveals the positioning accuracy. In this way the positioning accuracy for the wafer-to-wafer connection was estimated to be better than (5-10) μm, again precise enough for SLID to be used for connecting individual pixel cells.

The ICVs are needed if vertical integration is attempted. This can be done at two levels, either by connecting individual pixels by ICV, or by only routing the signals from the wire bond pads via ICV to reduce, or even avoid, the presently used balcony for the wire bond pads. However, this needs a special design of the read-out electronics that reserves inactive regions in the chip layout, to allow etching the vias. In the present design of the FEI3 chip such regions are not available for individual pixels. To still show the feasibility of ICV and to develop the processing steps, the present R&D concentrates on etching vias only at the read-out wire bond pads, that by design do not have active parts below them, see Fig. 6.59 for a schematic view. The location and layout of the vias have already been defined, and the first test etching on FEI3 wafers have been performed.

The progress of this R&D has been reported by members of the group at international conferences [134, 136, 137], including overview presentations of the entire ATLAS R&D on planar silicon sensors [138].

Outlook

The future steps of the pixel R&D consists of the production of thin n^+-in-p sensors for the IBL sensor qualification. Here the MPP design competes with the planar n^+-in-n design, as well as with 3D- and diamond sensors. The MPP&HLL thin n^+-in-p wafer production is partly done, and interconnection to the newly developed FEI4 chip with the conventional bump bonding process (the choice of interconnection made for the IBL) at IZM Berlin [139] is planned later this year. The SLID connection to FEI3 chips without ICVs is underway. The preparation of the chip- and sensor wafers has been done, the dicing and singularizing of the chips is presently ongoing, and SLID connections are planned later this summer. For the SLID connection to FEI3 chips with ICVs the design work is finished and first test etchings for the ICVs are underway.

6.3.2 Upgrade of the HEC: Motivation and Options

The LAr system consists of a barrel region and two endcap and forward regions. As seen from Fig. 6.67 the radiation levels increase with $|\eta|$. From the barrel to the endcap and from the endcap to the forward calorimeters the flux and average energy of the particles from minimum bias events increases with the consequent growth of multiplicity and density of shower particles. This results in a power density, and hence radiation flux, deposited in the calorimeters reaching levels not seen in previous collider detectors. The ATLAS calorimeters are designed to cope with a peak luminosity of 10^{34} cm^{-2}s^{-1} and an integrated luminosity of about 700 fb^{-1} as foreseen at the LHC.

Under SLHC conditions both the maximum instantaneous luminosity of 10^{35} cm^{-2}s^{-1} and the integrated luminosity of about 6000 fb^{-1} luminosity collected over an anticipated SLHC lifetime of 10 years will typically increase by an order of magnitude. It is

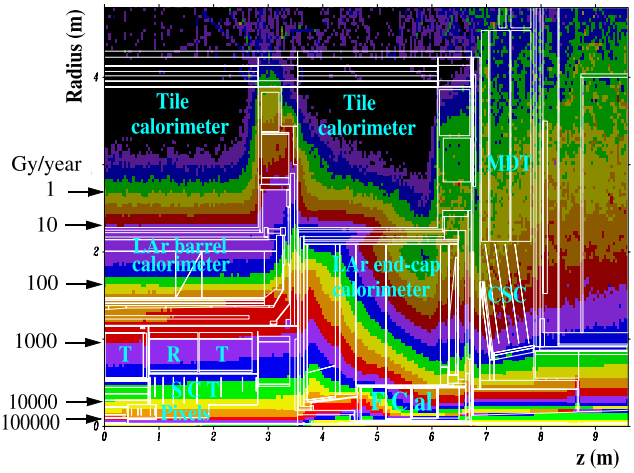

Figure 6.67: The total ionising dose per year calculated by the GCALOR software package in one quarter of the central part of the detector. The locations of the inner detector sub-systems, of the different calorimeters and of the inner endcap muon stations are indicated. The scale on the left gives the integrated dose per year corresponding to the various iso-lines.

safe to assume that the functioning of the LAr barrel EM calorimeter will suffer neither at highest peak luminosities nor from the integrated luminosity collected. Depending on the running conditions and the actual level of radiation, the performance of the forward calorimeter may be degraded due to the increased peak luminosity. On the other hand, it is unclear how much the endcap calorimeters (EMEC and HEC) will be affected. To understand the effects of luminosity on the endcap and forward regions, the so-called HiLum experiment has been launched.

One element which might be affected by the integrated luminosity is the front-end electronics of the HEC which is installed at the perimeter of the HEC in relatively high radiation fields.

In the vicinity of the HEC cold electronics a neutron fluence of 0.2×10^{14} n/cm^2, a γ dose of 330 Gy and a hadronic fluence of 3.1×10^{11} h/cm^2 are expected after 10 years of LHC operation at high luminosity. The radiation hardness against all three types of radiation has been studied with both preproduction and production versions of the HEC cold electronics chips both at room temperature and submerged in liquid nitrogen [140]. It was found that neutron irradiation is by far the most dangerous yielding the smallest safety margin. Measurements in these tests showed that the amplifiers start to degrade when the neutron fluence exceeds $\sim 3{\times}10^{14}$ n/cm^2. Compared to ATLAS requirements this amounts to a safety margin of about 15 for 10 years of LHC operation.

Assuming a ten times higher SLHC luminosity the safety margin is essentially eliminated, i.e. the present HEC cold electronics would be operated at its limit. It is therefore planned to develop a new ASIC that will be ten times more radiation hard. It would be available to replace the present GaAs chips at the SLHC.

The HiLum experiment

In order to establish the operating limits of the LAr endcap and forward calorimeters in conditions as close as possible to those that will occur at the SLHC, test modules of the EMEC, HEC, and FCal calorimeters were exposed to a proton high intensity beam at the IHEP 70 GeV synchrotron in Protvino, Russia [141, 142]. The beam intensities reached up to 10^{13} protons/spill. The performance of the ATLAS liquid-argon endcap calorimeters has been studied over a wide range of ionisation rates including those corresponding to SLHC luminosities and above. The EMEC, HEC, and FCal test modules are each installed in their own cryostats to help isolate potential poisoning of the liquid argon. They were installed one behind the other in the proton beam with interspersed shielding to spread the hadronic showers and to adjust the ionisation rates to be in approximately the same proportions as in ATLAS. The beam is extracted via the bent crystal technique, offering the unique opportunity to cover intensities ranging from 10^6 protons per spill (pps) up to 10^{12} pps. In addition, the machine has been operated with the 6 MHz RF bunch structure preserved and with 5 empty bunches between each filled bunch. This operation mode enables us to study the high flux response of the calorimeter modules unaffected by pile-up from previous bunches and thus reconstruct a clean signal of the response over the full drift time of electrons in the liquid argon gaps.

The beam intensity was not constant within a spill but varied from filled bunch to filled bunch. In order to correlate the calorimeter signal with the actual bunch intensity, a Cherenkov counter has been installed to measure the beam intensity in each single bunch, filled or not. The intensity ranges typically from 1 to 10^6 protons/bunch. The Cherenkov counter has been operated with air at atmospheric pressure, varying the PMT voltage to match the ADC dynamic range. The read-out was VME based and allowed to measure up to 6×10^6 bunch intensities per second.

A low pressure ionization chamber was used to monitor the proton flux per spill up to intensities of about 1×10^{11} pps. At higher intensities a secondary emission chamber with segmented electrodes monitored the flux and measured the beam profile in x and y.

Refs. [141, 142] describe the measurements on the degradation of the signal amplitude and shape as function of the beam intensity. The ionisation history over several positive Ar ion drift times preceding the trigger is also recorded to determine the space charge buildup with the required accuracy. These data allow an accurate determination of the positive ion mobility and the bulk ion/electron recombination rate. Additional tests

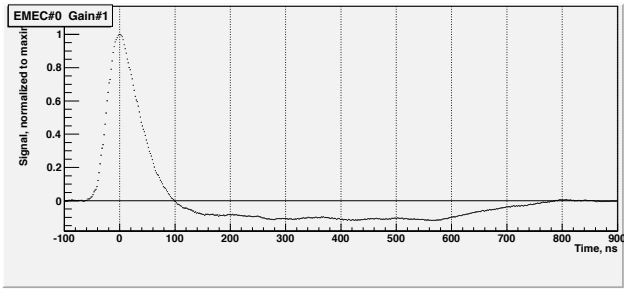

Figure 6.68: Pulse shape at an intensity of 6×10^7 protons per spill.

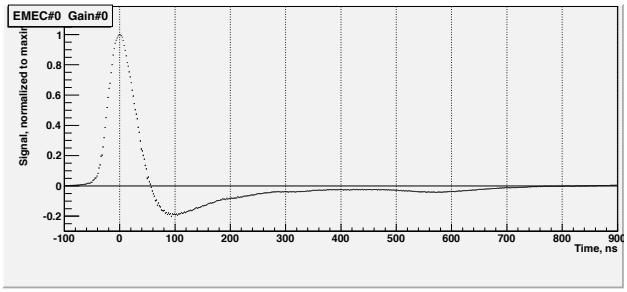

Figure 6.69: Pulse shape at an intensity of 2×10^{11} protons per spill.

include the measurements of the temperature rise due to beam heating, radiation damage studies, and performance studies of FCal electrodes with smaller LAr gaps.

Hadronic endcap electronics

Present HEC cold electronics. The signal processing of the HEC employs the notion of 'active pads' which keeps the detector capacities at the input of the amplifiers small and thereby achieves a fast rise time of the signal [140]. Short coaxial cables are used to send the signals from the read-out pads to preamplifier and summing boards (PSB) located at the perimeter of the wheels inside the liquid argon. The lateral segmentation is $\Delta\eta \times \Delta\phi = 0.1 \times 0.1$ up to $\eta = 2.5$ and $\Delta\eta \times \Delta\phi = 0.2 \times 0.2$ for higher η , and the longitudinal granularity is a fourfold read-out segmentation. The detector capacitance varies from 40 to 400 pF giving a rise time variation from 5 to 25 ns.

These PSB's carry highly integrated amplifier and summing chips in Gallium-Arsenide (GaAs) technology. The signals from a set of preamplifiers from longitudinally aligned pads (2, 4, 8, or 16 for different regions of the calorimeter) are then actively summed forming one output signal, which is transmitted to the cryostat feed-through.

The GaAs TriQuint QED-A 1 μm technology has been selected for the front-end ASIC because it offers excellent high frequency performance, stable operation at cryogenic temperatures and radiation hardness [140]. The front-end chip consists of 8 identical preamplifiers and two drivers. The summing scheme is implemented with external components and interconnections made on the PSB. The Fig. 6.70 shows a fully assembled HEC wheel in the horizontal position on the assembly table with the PSB boards (see Fig. 6.71) at the outer circumference.

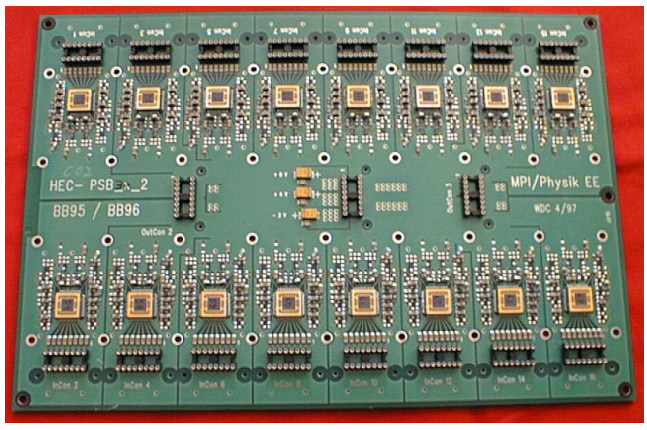

Figure 6.71: Picture of a Preamplifier and Summing Board PSB showing the 16 GaAs IC's with the related input connectors. The output connectors are in the center of the board. As the cabling will stay unchanged, the same connector types will be used for the new PSB's.

In the hadronic endcap calorimeter a neutron fluence of 0.2×10^{14} n/cm^2 is expected after 10 years

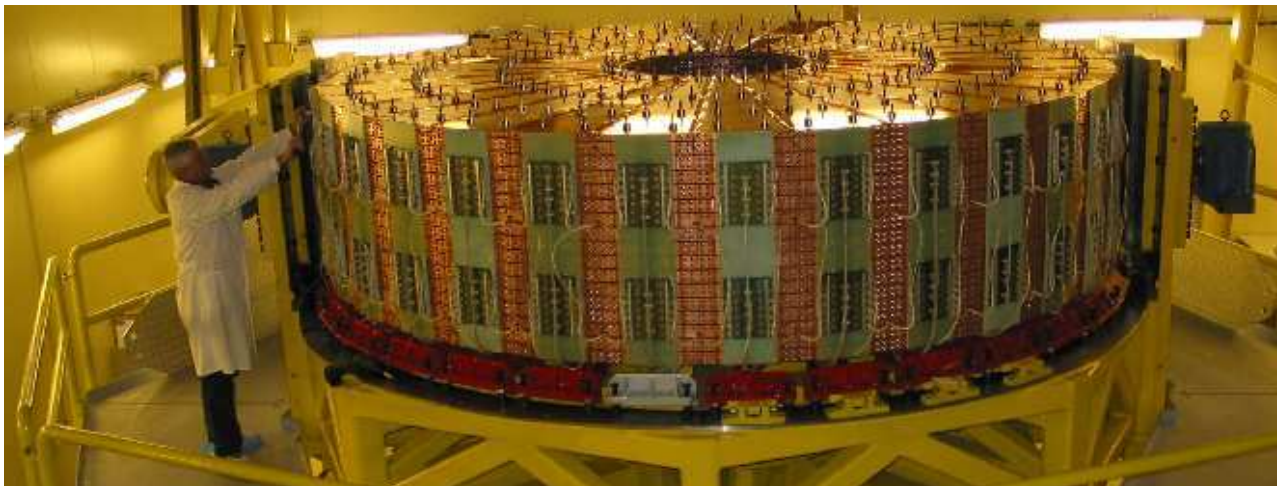

Figure 6.70: A HEC wheel fully assembled on the assembly table showing the 'active pad' electronics. The PSB boards with the GaAs IC's are mounted at the periphery of the wheel.

of LHC operation at high luminosity. It is known that GaAs is a radiation resistant semiconductor. The radiation hardness has been studied at the $IBR-2$ reactor in Dubna, Russia, with a set of pre-production chips. Various types of tests have been performed. Seven chips were exposed to a total fluence of fast neutrons of $(1.11 \pm 0.15) \times 10^{15}$ n/cm^2 and an integrated γ dose of (3.5 ± 0.3) kGy. A second set of 8 chips was irradiated with γ's up to a total dose of (55 ± 8) kGy accompanied by a fast neutron fluence of $(1.1 \pm 0.2) \times 10^{14}$ n/cm^2. In these tests the ASICs were kept in a cryostat filled with liquid nitrogen. The standard set of characteristics like transfer function, rise time, linearity and equivalent noise current of the preamplifiers was measured. The measurements show that the preamplifier characteristics start to degrade when the neutron fluence exceeds approximately 3×10^{14} n/cm^2. Fig. 6.72 shows the degradation of the amplitude with neutron irradiation for four different values of input (detector) capacitance. Such a degradation will result in a non-uniform response, which is critical since between 2 and 16 read-out pads are summed, and will ultimately impact the resolution required for physics measurements.

Similar measurements with γ-irradiation show that the characteristics stay unchanged up to a dose of at least 50 kGy. Both boundary values are well above the radiation levels expected in the final ATLAS environment at LHC.

Another important practical aspect of the cold electronics is the heating of the chips that can finally result in bubbling of the liquid argon. The bubbles propagating to a LAr detector gap can cause high voltage discharges. Therefore the power consumption has to be kept low.

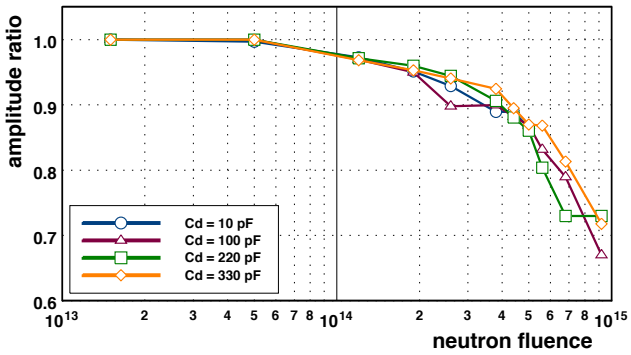

Figure 6.72: The signal amplitude measured after values of neutron fluence from 1.5×10^{13} to $9\times10^{14} n/cm^2$ for 4 different detector capacities. Shown is the ratio to the signal amplitude before the irradiation.

Requirements of the HEC cold electronics for the SLHC upgrade. The present ATLAS requirements for the HEC PSB boards, which have been developed with an LHC design luminosity of 10^{34}cm^{-2}s^{-1}, are 2×10^{12} n/cm^2 per year. Assuming an operation of 10 years, this yields a safety margin of about 10 for the LHC luminosity. Assuming a ten times higher integrated luminosity at SLHC the safety factor is essentially eliminated, i.e. the present HEC cold electronics would be operated at its limit. It is therefore planned to develop a new ASIC that will be ten times more radiation hard against neutrons. If needed, the new ASIC

will be used to replace the present GaAs chips at the SLHC. For an upgrade, the PSB boards at the circumference of the HEC wheel would then be replaced by new, pin-compatible PSB boards with more radiation hard IC's. This operation can be done without disassembling the HEC wheels but does require that the wheels be removed from the cryostat..

The requirements for the new IC's are:

- Radiation hardness for neutrons up to a factor of 10 better, i.e. up to a fluence of $\sim 2 \times 10^{15}\mathrm{n/cm^2}$.
- Low power consumption to stay safely away from the LAr boiling point at the operational pressure and temperature of the liquid argon. This means that the power consumption of the entire chip should not exceed the present level of < 0.2 W.
- As most of the quality control (QC) tests have to be done at room temperature, the gain of the preamplifiers and summing amplifiers should not vary by more than a factor of two from room to LAr temperature.
- The noise has to stay low, i.e. it should not exceed the present level of 50 nA with 0 pF input load or 100 nA with 200 pF load at each preamplifier input; the maximum signal for one preamplifier input is 250 μA, the dynamic range of the preamplifier has to be $\sim 5 \times 10^3$, that of the summing amplifier $\sim 10^4$.
- As only the summed signal from the full read-out channel can be electronically calibrated, the gain variation of the individual preamplifiers within the IC has to be below 1 %.
- The IC has to be safe against HV discharges in the gaps of the HEC modules.
- The input impedance has to be $(50 \pm 2)\ \Omega$ to cope with the existing cabling scheme.

Technologies studied. The radiation hardness against neutron irradiation has been studied for transistors of SiGe (Table 6.1), Si and GaAs (Table 6.2) technologies.

Typically four structures have been bonded in one ceramic package, which was mounted on a small test board. Up to 8 boards have been aligned in the neutron beam of the cyclotron at Rez/Prague. 37 MeV protons impinge on a D_2O target to generate a neutron flux up to $10^{11}\mathrm{ncm^{-2}s^{-1}}$. The energy spectrum peaks at low energies (1 MeV) with a steep decline towards higher energies. The flux falls off steeply with the distance from the target. The typical integrated flux obtained was of the order of $2 \times 10^{16}\mathrm{n/cm^2}$ for the closest position relative to the D_2O target. The performance of the transistors was continuously monitored with a network analyzer recording the full set of S-parameters. In addition, DC parameters (voltages and currents) were also recorded. Fig. 6.73 shows the

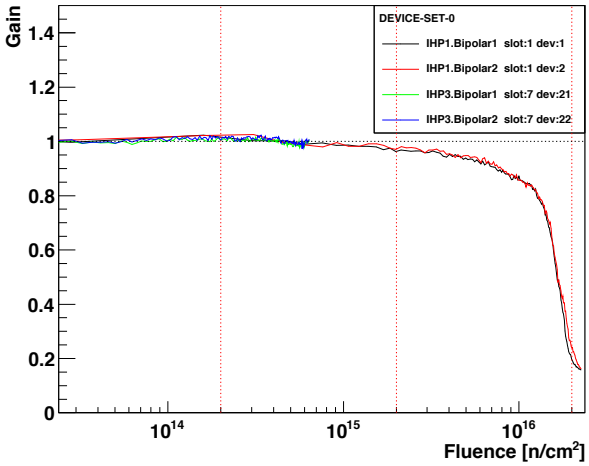

Figure 6.73: Dependence of the gain of four bipolar IHP transistors on the neutron fluence in units of $\mathrm{n/cm^2}$. The vertical dotted lines indicate the expected SLHC irradiation level, the requirements for the HEC cold electronics including the safety factor of 10 and the upper limit of the fluence reached in the irradiation runs. The transistors in slot 7 (green and blue lines) are irradiated up to a fluence of $\sim 6 \times 10^{14}\mathrm{n/cm^2}$ only. They don't show any degradation. The transistors in slot 1 (black and red lines) are irradiated up to a fluence of $\sim 2 \times 10^{16}\mathrm{n/cm^2}$. They show some degradation above a fluence of $\sim 2 \times 10^{15}\mathrm{n/cm^2}$. In the region of overlap all four transistors show a similar dependence of the gain on the fluence within the systematic error.

dependence of the gain on the neutron flux for four IHP bipolar transistors. The two transistors which are in slot one (black and red lines), i.e. closest to the D_2O target, were exposed to a neutron fluence of $2.2 \times 10^{16}\mathrm{n/cm^2}$. They show some degradation above a fluence of $\sim 2 \times 10^{15}\mathrm{n/cm^2}$. The corresponding neutron fluence for the equivalent transistors located in

slot seven (green and blue lines) is $\sim 6 \times 10^{14}$n/cm^2. They don't show any degradation. In the region of overlap all four transistors show a similar dependence of the gain on the fluence within the systematic error. The results show that the gain is rather stable in the range required for SLHC (including the safety factor of 10), i.e. up to 2×10^{15}n/cm^2.

Table 6.3 shows the loss of gain for the transistors for two different frequencies, studied at a neutron fluence of 2×10^{15}n/cm^2. The errors are dominated by systematic effects and are at the few percent level. All technologies investigated show only a small degradation of the gain up to the irradiation level expected for SLHC.

Another important aspect is the variation of the gain with temperature. This dependence has been studied for all technologies in the required range down to liquid N_2 temperatures. All bipolar technologies show a strong dependence of the operation point with temperature, therefore, to be used at the SLHC, they would require a voltage adjustment when going from room to liquid N_2 temperatures. This is different for the FET's where the gain variation is rather small within the temperature range studied.

Based on these studies both options, bipolar SiGe as well as CMOS FET technologies, are sufficiently stable under neutron irradiation and are being investigated further. Presently preamplifiers in both technologies are being developed. Studies of the dynamic range and noise performance are ongoing. We plan to irradiate these prototype preamplifiers in cold in the near future.

6.3.3 Upgrade of the Muon system for High Luminosities

The muon system will face two main challenges with luminosities beyond the design value:

(a) maintenance of excellent tracking efficiency of the MDT drift tube chambers in the presence of high background hit rates, due to converted neutrons and gammas and

(b) limitation of trigger rates for high-p_T muons at a level of about 20–30% of the overall ATLAS trigger rate, which is planned to remain at the present level of 100 kHz.

In the following chapters we present (a) a R&D project for the upgrade of drift tube chambers to cope with high background rates at the SLHC and (b) a method to upgrade the muon trigger by combining the high position accuracy of the MDT chambers with the high time resolution of the existing muon trigger chambers, decisively improving the selectivity of the muon trigger for high-p_T tracks.

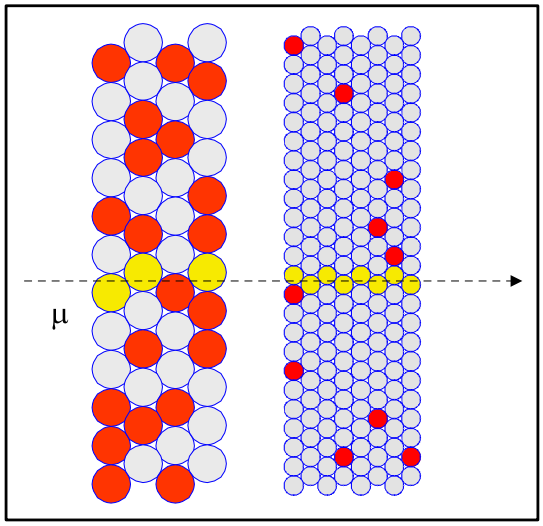

Figure 6.74: Illustration of the tracking quality in 30 mm and 15 mm drift tubes in a region of high n/γ background, as expected at the SLHC. The occupancies from background hits (red dots) are 50 % in the 30 mm tubes but only 7 % in the 15 mm tubes due to shorter drift time and smaller area.

Drift tube chambers for tracking in a high–background environment

The outer region of the ATLAS detector, where the muon chambers are located, receives high rates of low-energy neutrons, mainly due to shower leakage from calorimeters and shielding structures in the high-η region. At the nominal luminosity gammas from neutron capture and related conversion electrons are expected to generate hit rates in the range 50–300 kHz in each MDT tube. A conversion electron may mask a muon hit if the signal arrives *before* the muon signal, which leads to a muon detection efficiency of exp(-τ×f) ≈ 1 - τ×f, where τ is the average drift time in the MDT tubes and f the rate of hits due to gamma conversions.

At high rates of n/γ background, the efficiency may be further reduced by a decrease of the gas amplification due to space charge from slowly drifting positive ions in the tubes, while the *fluctuations* of the space charge tend to degrade the spatial resolution by up to about 20 % at the highest rates.

The effects of gamma conversions in the MDT tubes have been studied in detail using a muon beam in the presence of intense γ-irradiation of up to 500 Hz/cm^2

Table 6.1: Characteristics of the SiGe technologies (transistors) studied for radiation hardness using neutron irradiation.

Material	SiGe	SiGe	SiGe
Transistor	Bipolar HBT	Bipolar HBT	Bipolar HBT
Foundry	IHP	IBM	AMS
Process	SGB25V	8WLBiCMOS	BiCMOS
	250 nm	130 nm	350 nm
		MB and HB	
Type	npn	npn	npn

Table 6.2: Characteristics of the Si and GaAs technologies (transistors) studied for radiation hardness using neutron irradiation.

Material	Si	Si	Si	GaAs	GaAs
Transistor	CMOS FET	CMOS FET	CMOS FET	FET	FET
Foundry	IHP	IHP	AMS	Triquint	Sirenza
Process	SGB25V	SGB25V	BiCMOS	CFH800	
	250 nm	250 nm	350 nm	250 nm	250 nm
Type	nmos	pmos	nmos	pHEMT	pHEMT

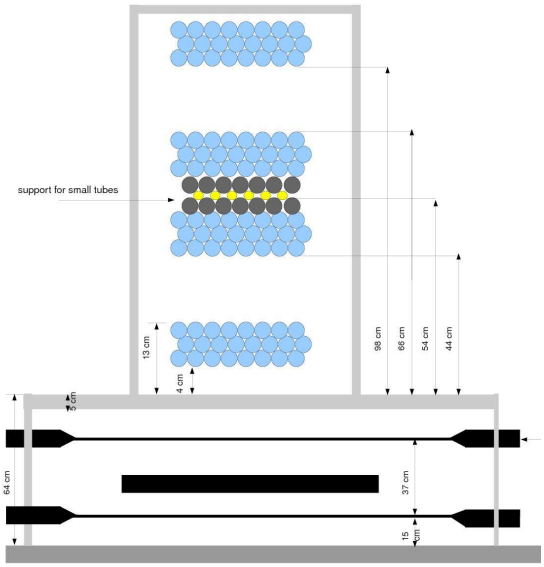

Figure 6.75: In this test setup the coordinates of a cosmic track are measured in 12 layers of 30 mm tubes (blue). The efficiency of the 15 mm tubes (yellow) is defined with respect to the fitted track, as explained in the text. Two scintillators below the setup are used for triggering.

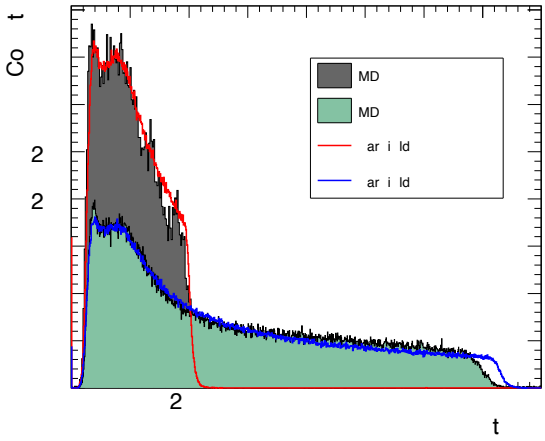

Figure 6.76: Comparison of the drift-time spectra of 30 mm and 15 mm diameter drift tubes at standard gas mixture, gas pressure and gas amplification. The maximum drift times are 700 and 200 ns, respectively, well reproduced by GARFIELD simulation.

(i.e. ∼300 kHz/tube), as delivered by the Gamma Irradiation Facility at CERN (GIF) [63]. While the γ-rates at the GIF correspond to only about 30% of the background levels expected for the hottest regions at the SLHC, the results of these measurements already allow to define the baseline of a chamber design with much improved tracking capability: MDT drift tube with only half the tube diameter offer a reduction of the drift time by a factor 3,5, due to the non-linear relation between track distance from the central wire and drift time (r-t relation) and in addition by a factor 2 from the exposed area, thus yielding a factor of 7 in the reduction of the hit rate due to n/γ background. Moreover, up to two times more tube layers can be accommodated in the available space, leading to improved track finding efficiency and position resolution (see Fig. 6.74).

Table 6.3: Loss of gain of the transistors studied for a neutron fluence of $2 \times 10^{15} \mathrm{n/cm^2}$ at two different frequencies.

Material	SiGe	SiGe	SiGe	Si	Si	Si	GaAs	GaAs
Transistor	Bipolar	Bipolar	Bipolar	CMOS FET	CMOS FET	CMOS FET	FET	FET
Foundry	IHP	IBM	AMS	IHP	IHP	AMS	Triquint	Sirenza
Type	npn	npn	npn	nmos	pmos	nmos	pHEMT	pHEMT
10 MHz	5%	5%	5%	4%	4%	3%	0%	4%
40 MHz	3%	2%	5%	2%	3%	3%	2%	2%

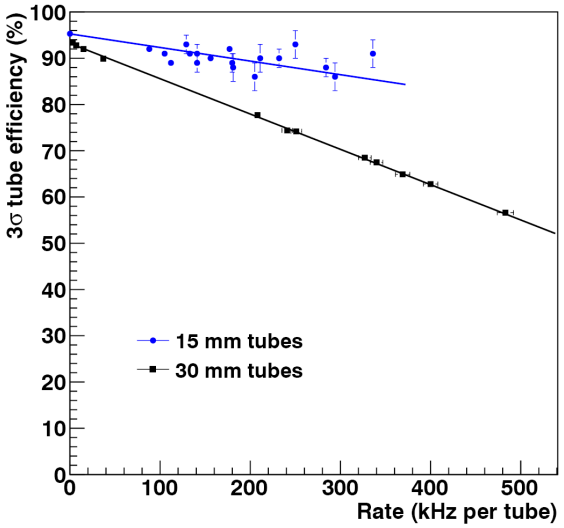

Figure 6.77: Efficiency vs. hit rate per tube for 30 mm and 15 mm drift tubes. For this measurement cosmic muon tracks were detected in the presence of gamma irradiation with adjustable intensity at the GIF facility at CERN.

The reduction of the tube diameter of the MDT tubes allows to maintain the main advantages of the drift tube concept:

- independence of the position resolution from the angle of incidence onto the chamber plane (contrary to drift chambers with rectangular drift geometry)
- operational independance of each tube, where any malfunction of a tube can only generate a negligible inefficiency
- modularity of chamber construction

Another advantage of maintaining the drift tube concept is that it allows to use the extensive experience with design and operation of the present MDT chambers with 30 mm tube diameter.

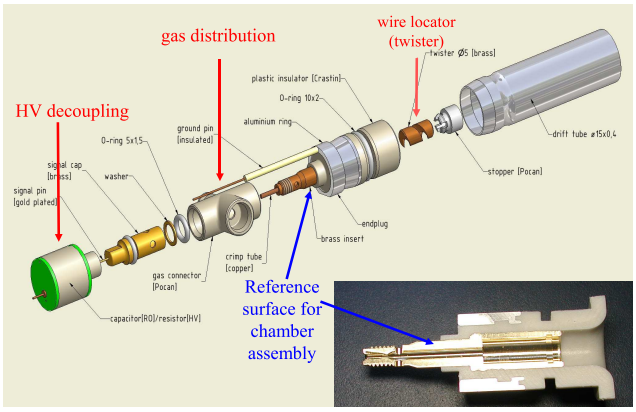

Figure 6.78: Structure of a small drift tube with gas connection and decoupling capacitor in the longitudinal direction (green zylinder). The plastic parts are injection moulded.

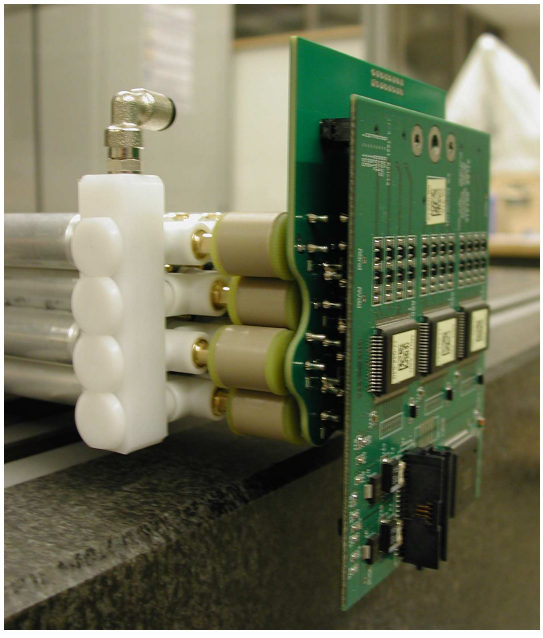

Figure 6.79: Integration of gas distribution system and readout electronics with the small tubes.

To verify the performance of 15 mm ("small") tubes

a number of tests was executed, using cosmic muon tracks. A pair of 30 mm ("large") drift tube chambers was used as reference, defining the position of the muon track, while a layer of small tubes was the device under test (see Fig. 6.75). Tubes along the track are called 'efficient' when the hit is detected inside a 3σ road, as defined by the reference tubes.

This measurement was done in the presence of various levels of gamma background due to a close-by, adjustable source (GIF test area at CERN). First tests [147] confirmed the expectation that by reducing the drift tube diameter by a factor of two whilst leaving all operational parameters unchanged, the maximum drift time is reduced by a factor of 3.5 (Fig. 6.76). Fig. 6.77 shows the efficiency of small and large tubes vs. hit rate from conversions, small tubes providing a much better performance, as expected. The efficiency at rate zero deviates from 100 % due to tracks passing across or close to the tube walls and due to δ-electrons shifting the position of the hit outside the 3σ acceptance road.

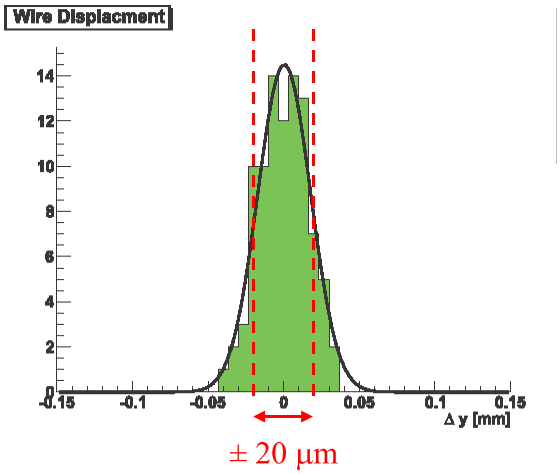

Figure 6.80: Distribution of the wire displacement from the nominal position, the decisive parameter for the measuring accuracy of the MDT chambers.

Going from large to small tubes as construction elements for MDT chambers poses a number of technical challenges, as the higher tube density requires more refined electrical and gas connections on the same available service area. This is a particular problem for the supply of the tubes with the operating voltage of 2750 V, requiring isolation distances which cannot be realized on the area available for the readout boards. The integration of the HV decoupling condensors into the end-plugs of the tubes was therefore a central requirement for the tube design. In a similar way, gas supply of each MDT tube by individual tublets, as implemented for the 30 mm tube MDTs, did not seem feasible for the production of chambers with four times higher tube density.

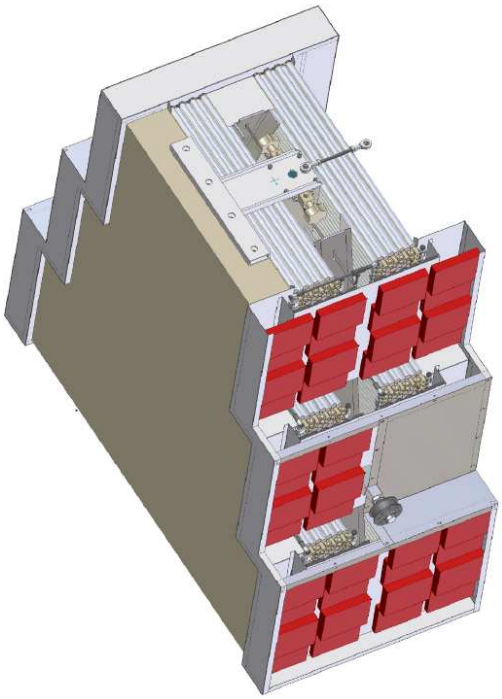

Figure 6.81: Design of a full prototype for a chamber to be implemented into the forward region of the ATLAS detector ("Small wheel").

Development work for small tube chambers started early in 2008 with an innovative tube design, where HV decoupling and gas distribution are integrated into the design of the end-plug (Fig. 6.78). Fig. 6.79 shows the integrated gas distribution scheme plus readout electronics for a 4-layer module of small tubes.

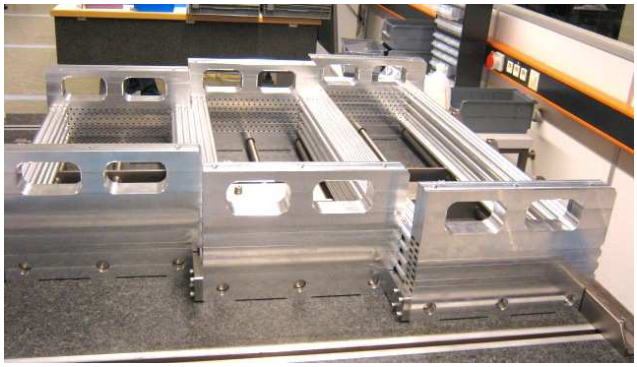

Figure 6.82: Precision placement of the small MDT tubes in high accuracy 'combs' before glueing with epoxy.

The integration of tubes into chambers is achieved

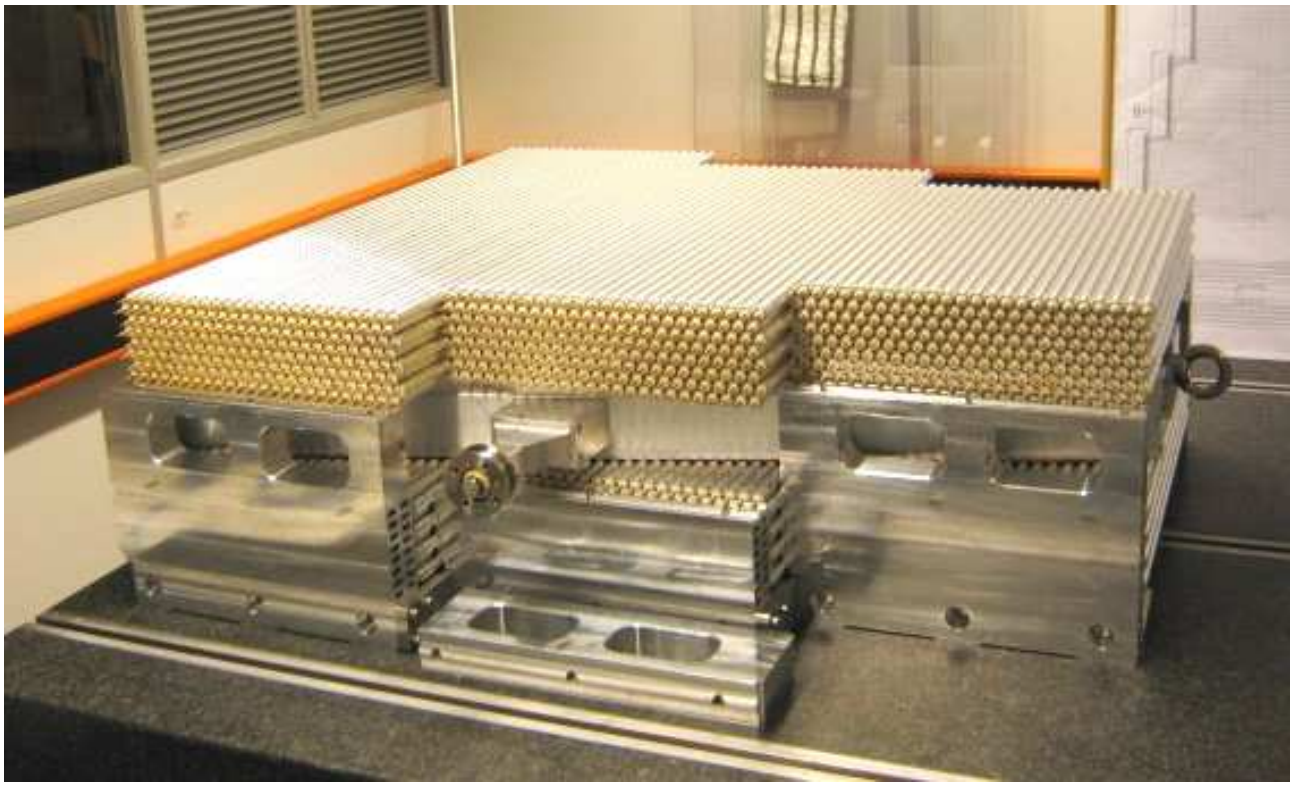

Figure 6.83: The small tube prototype chamber after assembly, consisting of two packages of 8 tube layers, with 72 tubes per layer and 1152 tubes in total.

by bonding tubes layer by layer with epoxy glue. This requires a high level of positioning accuracy and fixation during the curing. In production tests the target accuracy of 20 μm (Fig. 6.80) was obtained by placing the tubes into special supports ("combs"), see Fig. 6.82. All 8 tube layers were glued in a time span of a few hours, curing was overnight, such that the assembly of a tube package took only one day.

Presently, a full prototype of a MDT chamber in small tube technology is under construction (Fig. 6.81). It consists of 2×8 tube layers and is designed to fit into the inner part of the muon detector in the very forward direction, where rates are highest. This prototype will be available for tests at the GIF facility by fall 2010. The readout will be achieved with available electronics for the large tube chambers, specially adapted for use with the new chamber geometry.

Development of new electronics for small drift tube readout

The readout architecture of the present MDT system is described in [143]. While this proven concept is also applicable to the small tube system, the four times higher channel density is dictating a higher level of integration, more on-board data storage capacity and higher band width for data transfer to the counting room.

In addition, due to the ten times higher target for the integrated luminosity of the SLHC, electronics components have to survive correspondingly higher irradiation doses. Together with the Electronics Division of the MPI we are currently developing a new 16-channel Amplifier-Shaper-Discriminator (ASD) chip in IBM 130 nm technology, known to be radiation hard beyond what is expected for the Muon detector at SLHC.

To study the analog performance of the 130 nm technology in our application a prototype chip for the ASD with four channels was produced in 2009, showing excellent matching with the design parameters as well as of the gains among the four channels. Fig. 6.84 shows the response of two channels to the injection of a delta-charge.

For the TDC, measuring the drift times in the MDT tubes, a faster, radiation hard technology is introduced, based on developments of the CERN Micro Electronics Group.

For the on-chamber FPGAs, responsible for data formatting and transmission to the counting room, a new firmware is developed by MPI's Electronics Divi-

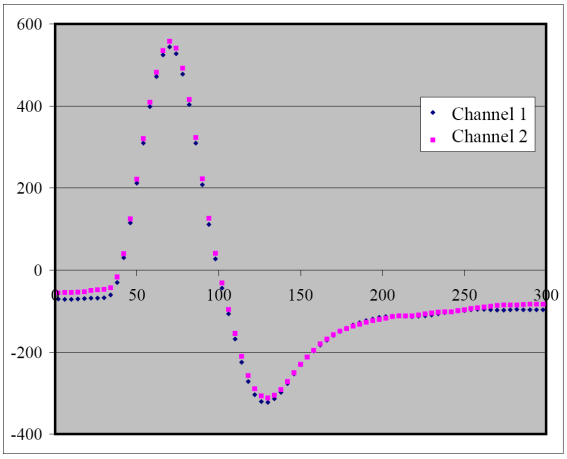

Figure 6.84: Performance of two channels in an ASD chip to be used in the frontend electronics of the MDT drift tubes. Gain and pulse shape of both channels correspond closely to the design parameters and to predictions from simulation.

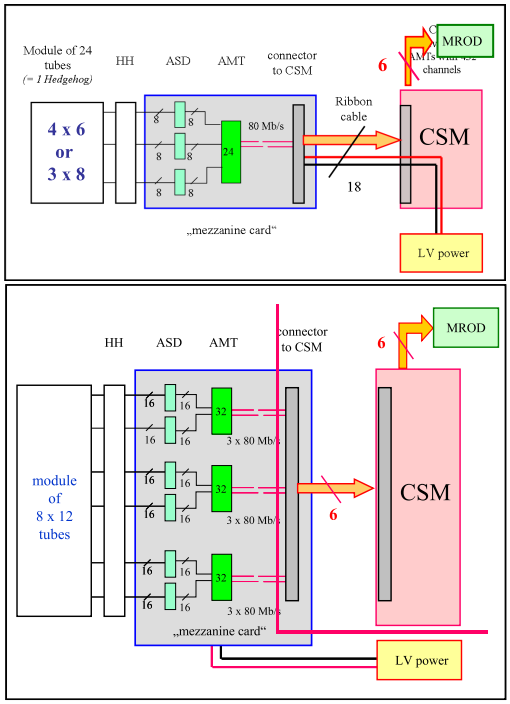

Figure 6.85: Present readout scheme for large MDT tubes, 24 tubes being served by one TDC ('AMT') on a readout card (top). In the future architecture 96 small tubes will be served by a card of comparable size, requiring a higher level of integration (bottom).

sion. The aim is to reduce the sensitivity of the configuration code to single event upsets from ionizing particles by the implementation of a high level of code redundancy (Triple Modular Redundancy). Finally, optical data transmission to the counting room will be based on the Gigabit Optical Link (GOL) chipset, developed by CERN. In this transmission scheme 5 Gbit/s will be available, about three times more than in the present SLINK scheme. A schematic diagram of the readout architecture of large and small tube chambers is given in Fig. 6.85.

Sharpening of the trigger threshold for high-p_T tracks

The capability to trigger on muon tracks with a transverse momentum (p_T) above a certain threshold was one of the principal requirements for the design of the muon spectrometer. MDT chambers with their long drift time of up to 750 ns, spanning 30 beam crossings, are not suited for this task and had to be complemented by specialized trigger chambers, capable of identifying tracks belonging to a given beam crossing.

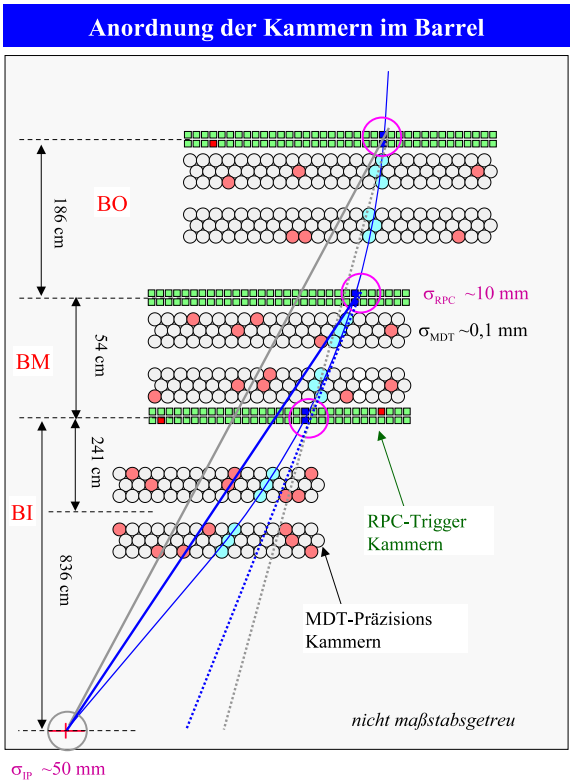

Figure 6.86: Implementation of the Level-1 trigger in the muon barrel region.

In the barrel region of the muon detector, the Resistive Plate Chamber (RPC) technology was selected for this purpose. This detector type uses pick-up strips perpendicular to the z-direction to sense the avalanches generated by traversing particles in the chamber gas, delivering the coordinates of the tracks along the bending direction of the magnetic field [48].

The time resolution of about 20 ns of the RPC chambers is sufficient to tag the beam crossing with about 95% confidence. Fig. 6.86 shows the schematics of the muon Level-1 triggering system in the barrel region. RPC trigger chambers (marked in green) are positioned at three radial positions of the barrel, one in the outer detector layer (BO) and two in the middle layer (BM), below and above the middle MDT. This way, three coordinate measurements are obtained along the track, defining the sagitta and thus p_T.

The implementation of the Level-1 trigger in the muon barrel uses a system of fast coincidences between the pick-up strips of the three RPC layers, estimating p_T from the bending of the track in the toroidal magnetic field. Due to the width of the RPC strips of 30 mm the p_T resolution for tracks above 15–20 GeV is not very sharp, the sagitta of a 20 GeV track being only 24 mm. Fig. 6.87 depicts the situation in a quantitative way. With a threshold setting of 20 GeV (red curve) the trigger is still accepting about 60% of the 15 GeV and 15% of the 10 GeV tracks. The corresponding, unwanted extra trigger rates from muons below threshold are by far not negligible, as the cross sections for most muon channels are strongly decreasing with p_T, while those of the more interesting physics channels (e.g. from W/Z decays) are roughly constant or even increasing, see Fig. 6.88.

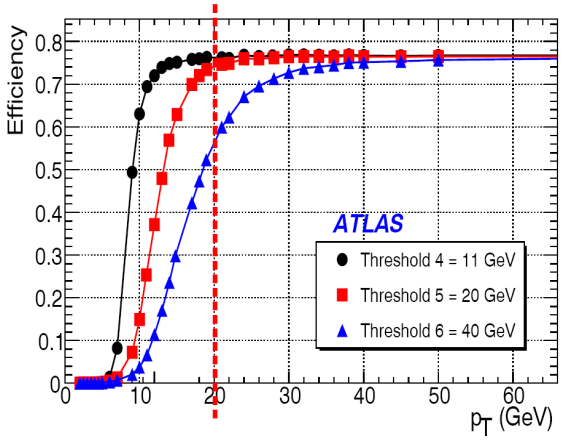

Figure 6.87: Acceptance of the Level-1 trigger vs. p_T for three typical trigger thresholds. For the 20 and 40 GeV thresholds the transitions from 90–10% efficiency cover a wide p_T-range, leading to high rates of unwanted triggers.

For practical and cost reasons the maximum Level-1 trigger rate for ATLAS at the SLHC is planned to remain at the present value of 100 kHz, and therefore the efficient rejection of triggers from low-p_T muon tracks is a prime requirement for the upgrade towards SLHC.

Improving the p_T-selectivity of the muon trigger means improving the precision of the track coordinates available for the Level-1 trigger decision. In the present ATLAS trigger hierarchy tracking information of the MDT is only used at the Level-2 trigger stage, where muon tracks are reconstructed using the precise MDT coordinates, leading to the rejection of more than 90% of the Level-1 muon triggers. Due to considerable computing and data transfer overheads, however, this result is only available after a latency of about 10 ms, three orders of magnitude beyond what is acceptable for the latency of the Level-1 trigger. If a Level-1 trigger arrives later than the maximum allowed latency, information in the front-end buffers of the ATLAS subdetectors may be lost.

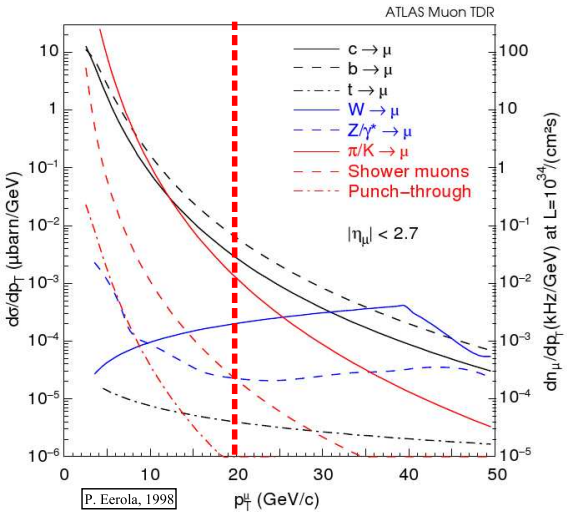

Figure 6.88: Transverse momentum distribution of muons in the ATLAS muon spectrometer for various production channels.

The challenge for an improvement of the Level-1 trigger is to design a MDT readout scheme, able to deliver a refined p_T-value inside a latency of a few microseconds. The present latency budget of 2,5 μs was adapted to the situation at the original LHC and is insufficient for any refinement of the trigger decision.

For SLHC, however, an increase of the latency to 6,4 μs or even 10 μs will be implemented for the front-tend data storage of all subdetectors, providing considerable design freedom for Level-1 trigger improvements.

The implementation of an improved muon barrel trigger requires an additional readout path of the MDT, in parallel and independent of the existing non-synchroneous, 'standard' readout path (Fig. 6.89).

For this fast MDT readout path the following design concept is pursued:

(a) Readout is only activated when a high-p_T candidate is flagged by the RPC trigger logic, saving occupancy and readout bandwidth.

(b) All MDT tubes but those close to the trajectory of the high-p_T muon candidate, as supplied by the RPC, will be ignored in the fast readout, saving data transfer and processing time.

(c) The resolution of the MDT drift time will be reduced from 12 to 7 bit. The corresponding position resolution of the MDT of about 1 mm (RMS) being still about a factor 10 better than the one of the RPC, sufficient for a decisive sharpening of the Level-1 trigger threshold. This way data volumina and transmission delays are reduced. For the same reason, data redundancy and format overheads will be reduced to the strict minimum.

(d) Separate fast communication lines will be installed to reduce transmission delays, while fast local processors will be used for the sagitta and p_T estimates.

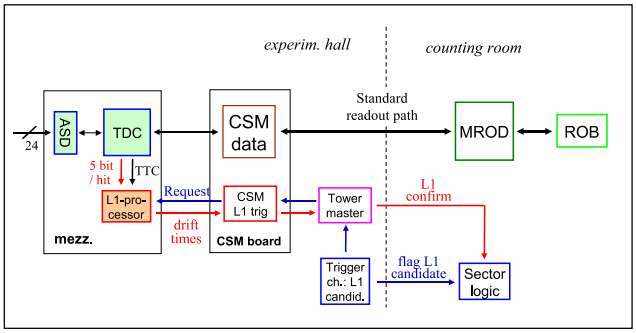

Figure 6.89: Readout architecture to combine the precision track coordinates determined in the MDT chambers with the 'fast' trigger flag supplied by the RPC's.

An analysis of the time behaviour of such a readout model shows that a latency of 4,5–5,5 μs could be achieved and thus would be a realistic option for the upgrade of the muon Level-1 trigger at the LHC. A significant advantage of this scheme would be that the existing RPC trigger chambers would not need an modifications (except electronics).

A similar upgrade scheme could also be applied to the Level-1 trigger in the end-cap region where trigger chambers of the TGC type are used [48]. Because of the different geometry of the toroidal magnetic field and the different location of trigger and MDT chambers, however, a modified architecture and specialized algorithms will have to be used.

In the context of this research program we have submitted four proposals to the ATLAS upgrade coordinator: (a) development of improved muon drift tube detectors [144] (b) development of radiation tolerant readout electronics [145] and (c) development of methods to reduce the data volume [146] or, alternatively, increase the bandwidth of the data acquisition system of the MDT chambers [145] for operation at very high luminosities.

References

[1] The MPP ATLAS group, *The ATLAS Experiment at the Large Hadron Collider LHC*, in Report to the Fachbeirat 2004-2006, Vol II (2007).

[2] ATLAS Collaboration, *The ATLAS Experiment at the CERN Large Hadron Collider*, Accepted for publication to JINST.

[3] The ATLAS Collaboration, *Inner Detector Technical Design Report*, CERN/LHCC/97-16 and 97-17 (1997).

[4] G. Aad *et al.*, The ATLAS Collaboration, *The ATLAS Experiment at the CERN Large Hadron Collider*, JINST 3 (2008) S08003.

[5] G. Aad *et al.*, The ATLAS Collaboration, *Expected Performance of the ATLAS Experiment - Detector, Trigger and Physics*, CERN-OPEN-2008-020 (2008) arxiv:0901.0512.

[6] G. Aad *et al.*, The ATLAS Collaboration, *The ATLAS Inner Detector commissioning and calibration*, accepted by Eur. Phys. J. C (2010), arxiv:1004.5293.

[7] G. Aad *et al.*, The ATLAS Collaboration, *Charged-particle multiplicities in pp interactions at* $\sqrt{(s)} = 900$ *GeV measured with the ATLAS detector at the LHC*, Phys. Lett. B688 (2010) 21-42.

[8] The MPP SCT group, *The ATLAS Semiconductor Tracker*, in Report to the Fachbeirat 1997-2003 (2004) 63-67.

[9] The MPP SCT group, *The ATLAS SemiConductor Tracker(SCT)*, in Report to the Fachbeirat 2004-2006, Vol II (2007) 77-85.

[10] A. Ahmad *et al.*, The ATLAS SCT Collaboration, *The Silicon microstrip sensors of the ATLAS semiconductor tracker*, Nucl. Instr. and Meth. A578 (2007) 98-118.

[11] A. Abdesselam *et al.*, The ATLAS SCT Collaboration, *The ATLAS semiconductor tracker end-cap module*, Nucl. Instr. and Meth. A575 (2007) 353-389.

[12] S. Haywood *et al.*, *Offline alignment & calibration of the Inner Detector*, ATLAS-INDET-2000-005, (2000).

[13] R. Härtel, *Iterative local χ^2 alignment approach for the ATLAS SCT detector*, diploma thesis, MPP and Technical University München (2005) MPP-2005-174.

[14] T. Göttfert, *Iterative local χ^2 alignment algorithm for the ATLAS pixel detector*, diploma thesis, MPP and Würzburg University (2006) MPP-2006-118.

[15] M. Kayl, *Kalman style alignment approach for the ATLAS SCT and pixel detectors*, diploma thesis, MPP and Technical University München (2007) MPP-2007-18.

[16] S. Pataraia, *Studies on top quark-pair production in pp collisions at the Large Hadron Collider with the ATLAS experiment*, PhD thesis, MPP and Technical University München (2009) MPP-2009-181.

[17] R. Härtel, *Studies on an initial top quark mass measurement at ATLAS in the lepton+jets* $t\bar{t}$ *channel and alignment of the Pixel and SCT subdetectors*, Ph.D. thesis, Technische Universität München, MPP-2009-134, Mar 2009.

[18] A. Ahmad *et al*., *Alignment of the Pixel and SCT Modules for the 2004 ATLAS Combined Test Beam* JINST 3 (2008) P09004.

[19] E. Abat *et al*., The ATLAS Collaboration, *Combined performance tests before installation of the ATLAS Semiconductor and Transition Radiation Tracking Detectors*, JINST 3 (2008) P08003.

[20] T. Göttfert, *Background suppression for a top quark mass measurement in the lepton+jets $t\bar{t}$ decay channel and Alignment of the ATLAS silicon detectors with cosmic rays*, Ph.D. thesis, Technische Universität München, MPP-2010-4, Dec 2009.

[21] J. Alison, B. Cooper and T. Göttfert, *Production of Systematically Misaligned Geometries for the ATLAS Inner Detector* ATL-INDET-INT-2009-003.

[22] R. Härtel, *Alignment of the ATLAS Inner Detector*, ACAT 2007 Conference, Amsterdam April 2007, PoS (ACAT) 049 (2007) MPP-2007-255.

[23] T. Göttfert, *ATLAS Inner Detector alignment*, HEP 2007 Conference, Manchester July 2007, J. of Physics: Conf. Series 110 (2008) 092012, MPP-2008-216.

[24] G. Cortiana, *Alignment of the ATLAS Inner Detector Tracking System*, IEEE 2009, Nuclear Science Symposium, Orlando Florida USA 2009, ATL-INDET-PROC-2009-020, MPP-2009-292.

[25] The ATLAS Collaboration, ATLAS Calorimeter Performance, CERN/LHCC/96-40, ATLAS TDR 1 (1996).

[26] The ATLAS Collaboration, ATLAS Liquid Argon Calorimeter Technical Design Report, CERN/LHCC/96-41, ATLAS TDR 2 (1996).

[27] D. M. Gingrich *et al*., Construction, assembly and testing of the ATLAS hadronic end-cap calorimeter, JINST **2** P05005 (2007).

[28] The ATLAS Liquid Argon HEC Collaboration, Performance of the ATLAS Hadronic End-Cap Calorimeter in Beam Tests, Nucl.Instr.& Meth. **A482**,94-124 (2002).

[29] A.E. Kiryunin *et al*., GEANT 4 Physics Evaluation with Testbeam Data of the ATLAS Hadronic End-cap Calorimeter, Nucl. Instr.& Meth. **A560**,278-290 (2006).

[30] H. Bartko, Performance of the Combined ATLAS Liquid Argon End-Cap Calorimeter in Beam Tests at the CERN SPS, MPP-2003-186, Diploma Thesis, Technical University Munich (2003).

[31] The ATLAS Liquid Argon EMEC/HEC Collaboration, Hadronic Calibration of the ATLAS Liquid Argon End-Cap Calorimeter in the Region $1.6 <|\eta|< 1.8$ in Beamtests, Nucl.Instr.& Meth. **A531**,481-514 (2004).

[32] The ATLAS Liquid Argon EMEC/HEC Collaboration, Muon Results from the EMEC/HEC Combined Run corresponding to the ATLAS Pseudorapidity Region $1.6 <|\eta|< 1.8$, ATL-LARG-2004-006 (2004).

[33] J. Pinfold *et al*., Performance of the ATLAS Liquid Argon End-Cap Calorimeter in the Pseudorapidity region $2.5 <|\eta|< 4.0$ in Beam Tests, Nucl.Instr.& Meth. **A593**,324-342 (2008).

[34] B. Andrieu *et al*., Results for pion calibration runs for the H1 liquid argon calorimeter and comparisons with simulations, Nucl. Instrum. Meth. **A336**,499 (1993).

[35] I. Abt *et al*., The tracking, calorimeter and muon detectors of the H1 experiment at HERA, Nucl. Instr.& Meth. **A386**,348 (1997).

[36] W. Lampl, S. Laplace, D. Lelas, P. Loch, H. Ma, S. Menke, S. Rajagopolan, D. Rousseau, S. Snyder, G. Unal, Calorimeter Clustering Algorithms: Description and Performance, ATL-LARG-PUB-2008-002 (2008).

[37] The ATLAS Collaboration, Local hadronic calibration, ATL-LARG-PUB-2009-001 (2009).

[38] The ATLAS Collaboration, Jet Reconstruction Performance, ATL-PHYS-PUB-2009-012 (2009).

[39] The ATLAS Collaboration, Detector Level Jet Corrections, ATL-PHYS-PUB-2009-013 (2009).

[40] The ATLAS Collaboration, Measurement of missing tranverse energy, ATL-PHYS-PUB-2009-016 (2009).

[41] The ATLAS Collaboration, Light jets in $t\bar{t}$ events, ATL-PHYS-PUB-2008-CSC-T2 (2008).

[42] G. Aad *et al*. [The ATLAS Collaboration], Expected Performance of the ATLAS Experiment - Detector, Trigger and Physics, arXiv:0901.0512 [hep-ex] (2009).

[43] John Paul Archambault *et al*., The simulation of the ATLAS liquid argon calorimetry, ATL-LARG-PUB-2009-001 (2009).

[44] The ATLAS Collaboration, G. Aad *et al.*, The ATLAS Experiment at the CERN Large Hadron Collider, JINST **3** S08003 (2008).

[45] The ATLAS Collaboration, G. Aad *et al.*, Readiness of the ATLAS Liquid Argon Calorimeter for LHC Collisions, arXiv:0912.2642 [physics.ins-det] (2009).

[46] J. Erdmann, Analysis of the Hadronic Calibration of the ATLAS End-Cap Calorimeters using Test Beam Data, MPP-2008-162, Diploma Thesis, LMU Munich (2008).

[47] E. Rauter, Top Quark Mass Measurement: Prospects of Commissioning Studies for Early LHC Data in the ATLAS Detector, MPP-2009-132, PhD Thesis, TU Munich (2009).

[48] The ATLAS Collaboration. Technical Design Report for the ATLAS Muon Spectrometer. Cern/lhcc/97-22, CERN, 1997.

[49] The ATLAS Collaboration. The ATLAS Experiment at the CERN Large Hadron Collider. *JINST*, (3), 2008.

[50] J. Dubbert, S. Horvat, O. Kortner, H. Kroha S. Kotov, S. Mohrdieck-Möck, and R.Richter. Final Evaluation of the Mechanical Precision of the ATLAS Muon Drift Tube Chambers. In *Proceedings of the 2006 IEEE Nuclear Science Symposium, San Diego, USA, 29 October–4 November 2006*. MPI report MPP-2006-167, November 2006.

[51] F. Bauer et al. Construction and Test of MDT Chambers for the ATLAS Muon Spectrometer. *Nucl. Instr. and Methods*, A(461), 2001.
F. Bauer et al. Construction and Test of the Precision Drift Chambers for the ATLAS Muon Spectrometer. *IEEE Trans. Nucl. Sci.*, 48:302, 2001.
F. Bauer et al. The First Precision Drift Tube Chambers for the ATLAS Muon Spectrometer. *Nucl. Instr. and Methods*, A(478):153, 2002.
F. Bauer et al. The First Precision Drift Tube Chambers for the ATLAS Muon Spectrometer. *Nucl. Instr. and Methods*, A(518):69, 2004.

[52] J. Dubbert et al. Integration, Commissioning, and Installation of Monitored Drift Tube Chambers for the ATLAS Barrel Muon Spectrometer. A(572):53, 2007. Proceedings of the 10^{th} Pisa Meeting on Advanced Detectors, Isola d'Elba, Italy, 21.–27.5.2006, MPI report MPP-2006-164.
J. Dubbert et al. Integration, Commissioning and Installation of Large Drift-Tube Chambers for the ATLAS Barrel Muon Spectrometer. In *Proceedings of the 2006 IEEE Nuclear Science Symposium, San Diego, USA, 29 October–4 November 2006*, volume 3, pages 1368–1372. MPI report MPP-2006-163.

[53] J. v.Loeben. Test und Kalibrierung der Präzisionsdriftrohrkammern des ATLAS-Myonspektrometers. Technical report, Technische Universität München, December 2006. Diploma thesis, MPI Report MPP-2006-241.

[54] J. Schmaler. Test and Alignment of the ATLAS Precision Muon Chambers. Technical report, Technische Universität München, March 2007. Diploma thesis, MPI Report MPP-2007-30.

[55] M. Groh. *Study of the Higgs Boson Discovery Potential in the Process $pp \to Hqq$, $H \to \tau\tau$ with the ATLAS Detector*. PhD thesis, Technische Universität München, May 2009. MPI Report MPP-2009-56, CERN-THESIS-2009-039.

[56] B. Bittner. Alignment of the ATLAS Muon Spectrometer Using Muon Tracks. Technical report, Technische Universität München, November 2008. Diploma thesis, MPI Report, MPP-2008-270.

[57] J. Dubbert (on behalf of the ATLAS collaboration). First Experience with the ATLAS Muon Spectrometer. *Nucl. Instr. and Methods*, A(581):507, 2007. Proceedings of the 11^{th} Vienna Conference on Instrumentation, Vienna, Austria, 19.–24.2.2007.

[58] J. von Loeben (on behalf of the ATLAS collaboration). First Cosmic Ray Results of the ATLAS Muon Spectrometer with Magnetic Field. In *Proceedings of the 2007 IEEE Nuclear Science Symposium, Honolulu, Hawaii, USA, 28 October–2 November 2007*. MPI report MPP-2007-175.

[59] J. von Loeben, M. Deile, N. Hessey, H. Kroha O. Kortner, and A. Staude. An Efficient Method to Determine the Space-to-Drift Time Relationship of the ATLAS Monitored Drift Tube Chambers. In *Proceedings of the 2007 IEEE Nuclear Science Symposium, Honolulu, Hawaii, USA, 28 October–2 November 2007*. MPI report MPP-2007-176.

[60] S. Horvat, O. Kortner, and H. Kroha. Determination of the Spatial Drift-Tube Resolution Using Muon Tracks. ATLAS Note ATL-MUON-PUB-2006-008, CERN, 2006.

[61] C. Adorisio et al. System Test of the ATLAS Muon Spectrometer at the H8 Beam at the CERN SPS. *Nucl. Instr. and Meth.*, A(593):232, 2008.

[62] C. Adorisio et al. Study of the ATLAS MDT Spectrometer Using High Energy CERN Combined Test Beam Data. *Nucl. Instr. and Meth.*, A(598):400, 2009.

[63] M. Deile et al. Performance of the ATLAS Precision Muon Chambers under LHC Operating Conditions. *Nucl. Instr. and Methods*, A(5518):65, 2004. Proceedings of the 10^{th} Pisa Meeting on Advanced Detectors, Isola d'Elba, Italy, 21.–27.5.2006.
M. Deile et al. Resolution and Efficiency of the ATLAS Muon Drift-Tube Chambers at High Background Rates. *Nucl. Instr. and Methods*, A(535):212, 2004. Proceedings of the 10^{th} Vienna Conference on Instrumentation, Vienna, Austria, 19.–24.2.2007.
S. Horvat et al. Operation of the ATLAS Muon Drift-Tube Chambers at High Background Rates and in Magnetic Fields. *IEEE Trans. Nucl. Sci.*, 53(2):562, 2006. MPI report MPP-2006-131.

[64] J. Dubbert et al. Modelling of the Space-to-Drift-Time Relationship of the ATLAS Monitored Drift-Tube Chambers in the Presence of Magnetic Fields. *Nucl. Instr. and Methods*, A(572):50, 2007. MPI report MPP-2006-166.

[65] P. Bagnaia, O. Biebel, C. Guyot, D. Orestano H. Kroha, and B. Zhou. A Proposal for the Calibration and Alignment of the ATLAS Muon Spectrometer. ATLAS Note ATL-MUON-INT-2006-006, CERN, 2008.

P. Bagnaia et al. Calibration model for the MDT chambers of the ATLAS Muon Spectrometer. ATLAS Note ATL-MUON-PUB-2008-004, CERN, 2008.

[66] Ch. Amelung et al. The ATLAS Muon Alignment System. In *Proceedings of the First LHC Alignment Workshop, CERN, Geneva, Switzerland, 4–6 September 2006*. CERN report CERN-2007-004.
J.C. Barriere et al. The Alignment System of the Barrel Part of the ATLAS Muon Spectrometer. ATLAS Note ATL-MUON-PUB-2008-007, CERN, 2008.

[67] O. Kortner, S. Kotov, H. Kroha, and I. Potrap. Alignment of the ATLAS Muon Spectrometer with Straight Tracks Using MILLEPEDE Method. ATLAS Note ATL-COM-MUON-2007-017, CERN, 2007.

[68] O. Kortner, S. Kotov, H. Kroha, J. Schmaler, and Ch. Valderanis. Alignment of the ATLAS Muon Spectrometer with Tracks and Muon Identification at High Background Rates, journal = Nucl. Instr. and Methods. A(581):545, 2007.

[69] O. Kortner, S. Kotov, H. Kroha, I. Potrap, and J. Schmaler. New Methods for the Alignment of the ATLAS Muon Spectrometer with Tracks. In *Proceedings of the 2007 IEEE Nuclear Science Symposium, Honolulu, Hawaii, USA, 28 October–2 November 2007*. MPI report MPP-2007-177.

[70] St. Kaiser. *Search for the Higgs Boson in the Process $pp \to Hqq, H \to WW$ with the ATLAS Detector*. PhD thesis, Technische Universität München, January 2010. MPI Report MPP-2010-38, CERN-THESIS-2010-043.

[71] N. Benekos, L. Chevalier, J.-F. Laporte, and M. Schott. Impacts of Misalignment on the Reconstructed Z-Boson Resonance at the ATLAS Muon Spectrometer. A(572):16, 2007. Proceedings of the 10^{th} Pisa Meeting on Advanced Detectors, Isola d'Elba, Italy, 21.–27.5.2006.
N. Benekos, L. Chevalier, J.-F. Laporte, and M. Schott. Final Evaluation of the Mechanical Precision of the ATLAS Muon Drift Tube Chambers. In *Proceedings of the 2006 IEEE Nuclear Science Symposium, San Diego, USA, 29 October–4 November 2006*. MPI report MPP-2006-173, November 2006.

[72] N. Benekos and M. Schott. Study of Z-Boson Measurements at the ATLAS Experiment. In *Proceedings of the Physics at LHC conference, Cracow, Poland, 3–8 July 2006*. MPI report MPP-2006-174, July 2006.

[73] O. Kortner, G. Mikenberg, H. Messer, and O. Primor. A Novel Approach to Track Finding in a Drift Tube Detector. *JINST*, (2), 2007.

[74] S. Baranov et al. Muon Detector Description as built and its Simulation for the ATLAS Experiment. A(572):14, 2007. Proceedings of the 10^{th} Pisa Meeting on Advanced Detectors, Isola d'Elba, Italy, 21.–27.5.2006.
D. Rebuzzi et al. Muon Detector Description as built and its Simulation for the ATLAS Experiment. In *Proceedings of the 2006 IEEE Nuclear Science Symposium, San Diego, USA, 29 October–4 November 2006*, volume 3. MPI report MPP-2006-170.

[75] D. Rebuzzi et al. GEANT4 Muon Digitization in the ATHENA Framework. In *Proceedings of the 2006 Computing in High Energy Physics Conference, Mumbai, India, 13–17 February 2006*, volume 3. MPI report MPP-2006-178.

[76] J. v.Loeben. *Calibration of the ATLAS Muon Precision Chambers and Study of the Decay $\tau \to \mu\mu\mu$ at the LHC*. PhD thesis, Technische Universität München, May 2010. MPI Report MPP-2010-88.

[77] M. Cirilli et al. Conditions Database and Calibration Software Framework for ATLAS Monitored Drift Tube Chambers. *Nucl. Instr. and Methods*, A(572):38, 2007.

[78] O. Kortner (on behalf of the ATLAS collaboration). Commissioning of the Charged Lepton Identification with Cosmic Rays in ATLAS. *PoS (HCP2009) 009*, 2009.

[79] The ATLAS collaboration. Expected Performance of the ATLAS Experiment: Detector, Trigger and Physics. *arXiv:1006.4384*. submitted to EPJC (18 June 2010).

[80] The ATLAS collaboration. Expected Performance of the ATLAS Experiment: Detector, Trigger and Physics. *arXiv:0901.0512*, 2008. CERN-OPEN-2008-020.

[81] M. Antonelli et al. In-situ determination of the performance of the ATLAS muon spectrometer. *Nucl. Phys. Proc. Suppl.*, (177-178):326, 2008. Proceedings of the 11^{th} Vienna Conference on Instrumentation, Vienna, Austria, 19.–24.2.2007.

[82] The ATLAS collaboration. Muon Performance in Minimum Bias pp Collision Data at $\sqrt{s}$=7 TeV with ATLAS. ATLAS Conference Note ATL-CONF-2010-036, CERN, 2010.

[83] The ATLAS collaboration. Muon Reconstruction Performance. ATLAS Note ATL-COM-PHYS-2010-430, CERN, 2010.

[84] D. Adams et al., CERN-LHCC-2004-037 (2005).

[85] G. Duckeck et al., CERN-LHCC-2005-022 (2005).

[86] H. Hoffmann et al., CERN-LHCC-2001-004 (2001).

[87] The WLCG Parties, CERN-C-RRB-2005-01 (2005).

[88] J. Mejia, S. Kluth, S. Stonjek, (2009), Poster contributed to International Conference on Computing in High Energy and Nuclear Physics (CHEP2009).

[89] The MPP ATLAS group, *ATLAS Analysis*, Report to the Fachbeirat 1997–2003 Part II, (2004), 82-84.

[90] The MPP ATLAS group, *ATLAS Physics Analysis*, Report to the Fachbeirat 2004–2006 Part II, (2006), 106-112.

[91] The MPP ATLAS group, *ATLAS Physics Analysis*, Annual Report 2006-2007 Part II, (2008), 107-116.

[92] The ATLAS Collaboration,
Preliminary studies for the measurement of the inclusive muon spectrum in pp collisions at $\sqrt{s} = 7$ TeV with the ATLAS detector, contribution to PLHC 2010, ATL-COM-CONF-2010-035.

[93] The ATLAS Collaboration, *Extraction of the prompt muon component in inclusive muons produced at* $\sqrt{s} = 7$ *TeV* , contribution to ICHEP 2010, ATL-COM-PHYS-2010-431.

[94] The ATLAS Collaboration, *Observation of prompt inclusive electrons in the ATLAS experiment at* $\sqrt{s} = 7$ *TeV*, contribution to ICHEP 2010, ATL-COM-PHYS-2010-422.

[95] The ATLAS Collaboration, *W/Z Cross-Sections*, contribution to ICHEP 2010, ATL-COM-PHYS-2010-475.

[96] G. Cortiana, T. Göttfert, P. Haefner, R. Nisius, P. Weigell, *Template Method for an early Top-Quark Mass Measurement in the* $t\bar{t} \rightarrow$ *lepton+jets Channel with ATLAS Data*, ATLAS internal note, ATL-PHYS-INT-2010-007, December 2009.

[97] The ATLAS Collaboration, G. Aad et al., *Expected Performance of the ATLAS Experiment Detector, Trigger and Physics*, CERN-OPEN-2008-020, pp898 (2008).

[98] P. Weigell, *Constrained Kinematic Fitting for a Top Quark Mass Determination in the Electron + Jets Channel at ATLAS*, Diploma thesis, Technische Universität München, MPP-2009-177, Oct 2009.

[99] E. Rauter, *Top Quark Mass Measurement: Prospects of Commissioning Studies for Early LHC Data in the ATLAS Detector*, Ph.D. thesis, Technische Universität München, MPP-2009-132, Jun 2009.

[100] The ATLAS Collaboration, *Prospects for the Measurement of the Top-Quark Mass using the Template Method with early ATLAS Data*, ATLAS public note, ATL-PHYS-PUB-2010-004, May 2010.

[101] G. Cortiana, R. Nisius, *Measurement of the Top-Quark Mass using the stabilized Mass Variable via the Template Method in the* $t\bar{t} \rightarrow$ *lepton+jets at ATLAS*, ATLAS internal note, ATL-PHYS-INT-2010-027, March 2010.

[102] S. Pataraia, *Studies on top quark-pair production in pp collisions at the Large Hadron Collider with the ATLAS experiment*, Ph.D. thesis, Technische Universität München, MPP-2009-181, Oct 2009.

[103] J. Schieck, *Early Top Physics with ATLAS*, ICPP Conference, Istanbul, Turkey, 27 - 31 Oct 2008, Balkan Phys. Lett. 17 (2009).

[104] G. Cortiana, *Prospects for the measurement of the top-quark mass with early ATLAS data*, TOP 2010 Conference, Brügge, Belgium, May 31 - Jun 4 2010, to be published in Nuovo Cim. C., MPP-2010-74

[105] The ATLAS Collaboration, *Higgs Boson, in Expected performance of the ATLAS experiment*, pages 1198-1511, CERN-OPEN-2008-020, CERN, Geneva, 2009, arXiv:hep-ex/0901.0512, MPP-2009-1.

[106] The ATLAS Collaboration, *ATLAS Sensitivity Prospects for Higgs Boson Production at the LHC Running at 7 TeV*, ATLAS public note (under approval), ATL-COM-PHYS-2010-373, CERN, Geneva, 2010.

[107] The ATLAS Collaboration, *Search for the Standard Model* $H \rightarrow ZZ^{(*)} \rightarrow 4\ell$, *in Expected performance of the ATLAS experiment*, pages 1243-1270, CERN-OPEN-2008-020, CERN, Geneva, 2009, arXiv:hep-ex/0901.0512, MPP-2009-1.

[108] Ch. Anastopoulos et al., *ATLAS sensitivity prospects for the Standard Model Higgs boson in the decay channel* $H \rightarrow ZZ^{(*)} \rightarrow 4\ell$ *at* $\sqrt{s}$*=10 and 7TeV*, ATLAS internal note, ATL-PHYS-INT-2010-062, CERN, Geneva, 2010.

[109] The ATLAS Collaboration, *Higgs Boson Searches in Gluon Fusion and Vector Boson Fusion using the* $H \rightarrow WW$ *Decay Mode, in Expected performance of the ATLAS experiment*, pages 1306-1332, CERN-OPEN-2008-020, CERN, Geneva, 2009, arXiv:hep-ex/0901.0512, MPP-2009-1.

[110] Steffen Kaiser, *Search for the Higgs Boson in the Process* $pp \rightarrow Hqq, H \rightarrow WW$ *with the ATLAS Detector*, Dissertation, Technische Universität München, 2010, MPP-2010-38.

[111] S. Kaiser, S. Horvat, O. Kortner, H. Kroha, *Impact of Pile-up on the Search for* $H \rightarrow WW$ *in VBF Production and Study of Track Jets for the Central Jet Veto*, ATLAS internal note (under approval), ATL-COM-PHYS-2010-197, CERN, Geneva, 2010.

[112] S. Kotov, S. Horvat, O. Kortner, H. Kroha, S. Mohrdieck-Möck; J. Yuan, *Search for the SM Higgs boson in the* $H \rightarrow b\bar{b}$ *decay channel in associated production with* $t\bar{t}$ *using neural network techniques*, ATLAS internal note, ATL-PHYS-INT-2008-027, CERN, Geneva, 2010.

[113] S. Horvat, O. Kortner, H. Kroha, S. Kotov, J. Yuan, *Feasibility study of the observability of the* $H \rightarrow b\bar{b}$ *in Vector Boson Fusion production with the ATLAS detector*, ATLAS internal note, ATL-PHYS-INT-2008-048, CERN, Geneva, 2010.

[114] The ATLAS Collaboration, *Search for the Standard Model Higgs Boson via Vector Boson Fusion Production Process in the Di-Tau Channels, in Expected performance of the ATLAS experiment*, pages 1271-1305, CERN-OPEN-2008-020, CERN, Geneva, 2009, arXiv:hep-ex/0901.0512, MPP-2009-1.

[115] Manfred Groh, *Study of the Higgs Boson Discovery Potential in the Process* $pp \rightarrow Hqq, H \rightarrow \tau^+\tau^-$ *with the ATLAS Detector*, Dissertation, Technische Universität München, 2009, MPP-2009-56.

[116] Georgios Dedes, *Study of the Higgs Boson Discovery Potential in the Process* $pp \rightarrow H/A \rightarrow \mu^+\mu^-/\tau^+\tau^-$ *with the ATLAS detector*, Dissertation, Technische Universität München, 2008, MPP-2008-32.

[117] The ATLAS Collaboration, *Search for the Neutral MSSM Higgs Bosons in the Decay Channel* $A/H/h \rightarrow \mu^+\mu^-$, *in Expected performance of the ATLAS experiment*, pages 1391-1418, CERN-OPEN-2008-020, CERN, Geneva, 2009, arXiv:hep-ex/0901.0512, MPP-2009-1.

[118] S. Stern, *Measurement of the $\mu^+\mu^-$ Background for Neutral MSSM Higgs Searches with the ATLAS Detector*, Diplomarbeit, Technische Universität München, 2009, MPP-2009-211.

[119] S. Horvat, O. Kortner, H. Kroha, S. Stern, *Prospects for data-driven estimation of the $\mu^+\mu^-$ background for neutral MSSM Higgs searches in the decay channel $h/H/A \rightarrow \mu^+\mu^-$*, ATLAS internal note, ATL-PHYS-INT-2010-058, CERN, Geneva, 2010.

[120] S. Horvat, O. Kortner, H. Kroha, S. Stern, *ATLAS sensitivity prospects for the neutral MSSM Higgs bosons in the $H/A \rightarrow \mu^+\mu^-$ decay channel at $\sqrt{s} = 7$ TeV*, ATLAS internal note, ATL-PHYS-INT-2010-057, CERN, Geneva, 2010.

[121] The ATLAS Collaboration, *Charged Higgs Boson Searches, in Expected performance of the ATLAS experiment*, pages 1451-1479, CERN-OPEN-2008-020, CERN, Geneva, 2009, arXiv:hep-ex/0901.0512, MPP-2009-1.

[122] Thies Ehrich, *Search for Light Charged Higgs Bosons in Hadronic Final States with the ATLAS Detector*, Dissertation, Technische Universität München, 2010.

[123] T. Ehrich, S. Mohrdieck-Moeck, S. Horvat, O. Kortner, H. Kroha, *Data-driven measurement of the fake tau contribution from light jets and application for the ttbar background estimation in charged Higgs Searches*, ATLAS internal note, ATL-COM-PHYS-2009-662 (under approval), CERN, Geneva, 2010.

[124] ATLAS collaboration, *Data-driven determinations of W, Z and top background to supersymmetry searches at the LHC, in Expected Performance of the ATLAS Experiment - Detector, Trigger and Physics*, p. 1525, 2009

[125] ATLAS collaboration, *Data-Driven Determination of $t\bar{t}$ Background to Supersymmetry Searches in ATLAS*, ATL-PHYS-PUB-2009-083, 2009

[126] ATLAS collaboration, *Early supersymmetry searches without leptons with the ATLAS Detector*, ATL-COM-PHYS-2010-411, 2010 **replace by pubnote!!!**

[127] Jörg v. Loeben. *Calibration of the ATLAS Precision Muon Chambers and Study of the Decay $\tau \rightarrow \mu\mu\mu$ at the Large Hadron Collider*, MPP-2010-88, PhD Thesis, Technical University Munich, 2010

[128] N. Hessey *et al.*, *Layout Requirements and Options for a new Inner Tracker for the ATLAS Upgrade*, ATLAS internal document, ATL-P-EP-0001, (2007).

[129] R. Nisius *et al.*, *R&D on a novel interconnection technology for 3D integration of sensors and electronics and on thin pixel sensors*, ATL-P-MN-0019, ATLAS internal document, (2007).

[130] L. Andricek *et al.*, *Processing of ultra-thin silicon sensors for future linear collider experiments*, IEEE Transactions on Nuclear Science 51 (2004) 1117-1120.

[131] E. Fretwurst *et al.*, *High energy proton damage effects in thin high resistivity FZ silicon detectors*, Nucl. Instr. and Meth. A552 (2005) 124-130.

[132] A. Klumpp *et al.*, *Vertical System Integration by Using Inter-Chip Vias and Solid-Liquid InterDiffusion Bonding*, Japanese Journal of Applied Physics 43, No 7A.

[133] Fraunhofer-Institut für Zuverlässigkeit und Mikrointegration IZM, Institutsteil München, Hansastraße 27d, 80686 München, Germany.

[134] A. Macchiolo *et al.*, *Development of thin pixel sensors and a novel interconnection technology for the SLHC*, 9th International Workshop on Radiation Imaging Detectors, Erlangen, Germany 22-26 July 2007, Nucl. Instr. and Meth. A591 (2008) 229-232.

[135] M. Beimforde, *Investigations towards a pixel detector for the Super LHC*, PhD thesis, MPP and Technical University München (2010) MPP-2010-??.

[136] A. Macchiolo *et al.*, *Application of a new interconnection technology for the ATLAS pixel upgrade at SLHC*, TWEPP-09, Topical Workshop on Electronics for Particle Physics, Paris, France, 21–25 Sep 2009, CERN-2009-006 (2009) 216-219.

[137] L. Andricek *et al.*, *Development of thin sensors and a novel interconnection technology for the upgrade of the ATLAS pixel system*, 7th International Hiroshima Symposium on Development and Applications of Semiconductor Tracking Devices, Hiroshima, Japan, Aug. 29-Sep.1, 2009, Nucl. Instr. and Meth. A (2010) to be published.

[138] M. Beimforde, *The ATLAS Planar Pixel Sensor R&D project*, 7th International Hiroshima Symposium on Development and Applications of Semiconductor Tracking Devices, Hiroshima, Japan, Aug. 29-Sep.1, 2009, Nucl. Instr. and Meth. A (2010) to be published.

[139] Fraunhofer-Institut für Zuverlässigkeit und Mikrointegration IZM, Institutsteil Berlin, Gustav-Meyer-Allee 25, 13355 Berlin, Germany.

[140] J. Ban et al., Cold Electronics for the Liquid Argon Hadronic End-cap Calorimeter of ATLAS, Nucl. Instr.& Meth. **A556**, 158-168 (2006).

[141] P. Schacht for the Hilum and HECPAS collaboration, ATLAS Liquid Argon Endcap Calorimeter R & D for sLHC, Proceedings of the 11th ICATPP Conference on Astroparticle, Particle, Space Physics, Detectors and Medical Physics Applications, Como, 5-9 October 2009.

[142] Hilum Collaboration, A proposal for R & D to establish the limitations on the operation of the ATLAS endcap calorimeters at high LHC luminosities, INTAS Project INTAS-CERN 05-103-7555, INTAS Progress Report 2008 (2008) and INTAS Final Report (2009).

[143] Y. Arai et al., *ATLAS Muon Drift Tube Electronics*, JINST **3** P09001 (2008)

[144] O. Biebel, J. Dubbert, S. Horvat, O. Kortner, H. Kroha, R. Richter, D. Schaile, *Expression of Interest: R&D on Precision Drift Tube Detectors for Very High Background Rates at SLHC*, ATLAS document, ATL-M-MN-0006, March 2007.

[145] O. Biebel, J. Dubbert, S. Horvat, O. Kortner, H. Kroha, R. Richter, D. Schaile, *Upgrade of the MDT Readout Chain for the SLHC*, ATLAS document, ATL-M-MN-0003, March 2007.

[146] O. Biebel, J. Dubbert, S. Horvat, O. Kortner, H. Kroha, R. Richter, D. Schaile, *Upgrade of the MDT Electronics for the SLHC Using Selective Readout*, ATLAS document, ATL-M-MN-0005, March 2007.

[147] J. Dubbert, S. Horvat, O. Kortner, H. Kroha, F. Legger, R. Richter, F. Rauscher, *Development of Precision Drift Tube Detectors for the Very High Background Rates at the Super-LHC*, proceedings of the 2007 IEEE Nuclear Science Symposium, Honolulu, Hawaii, USA, 28 October–2 November 2007, MPI report, MPP-2007-172, November 2007, to be published in the IEEE Transactions on Nuclear Science.